Since 1955

Strojniški vestnik
Journal of Mechanical Engineering

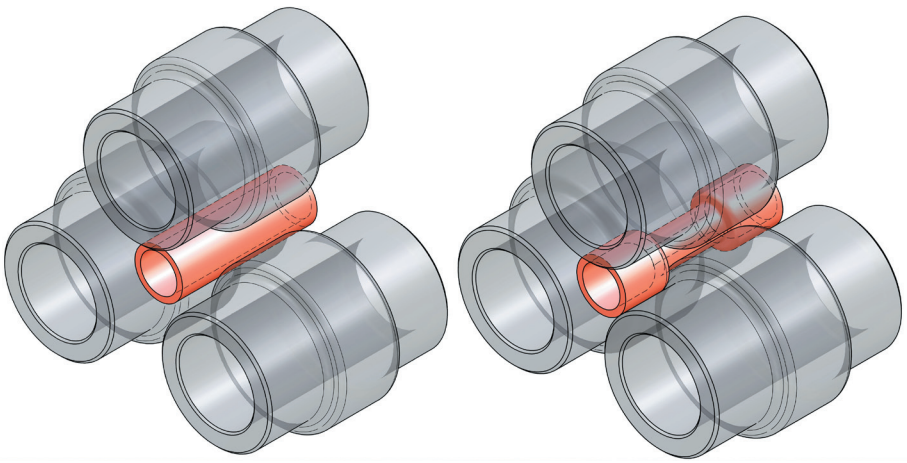

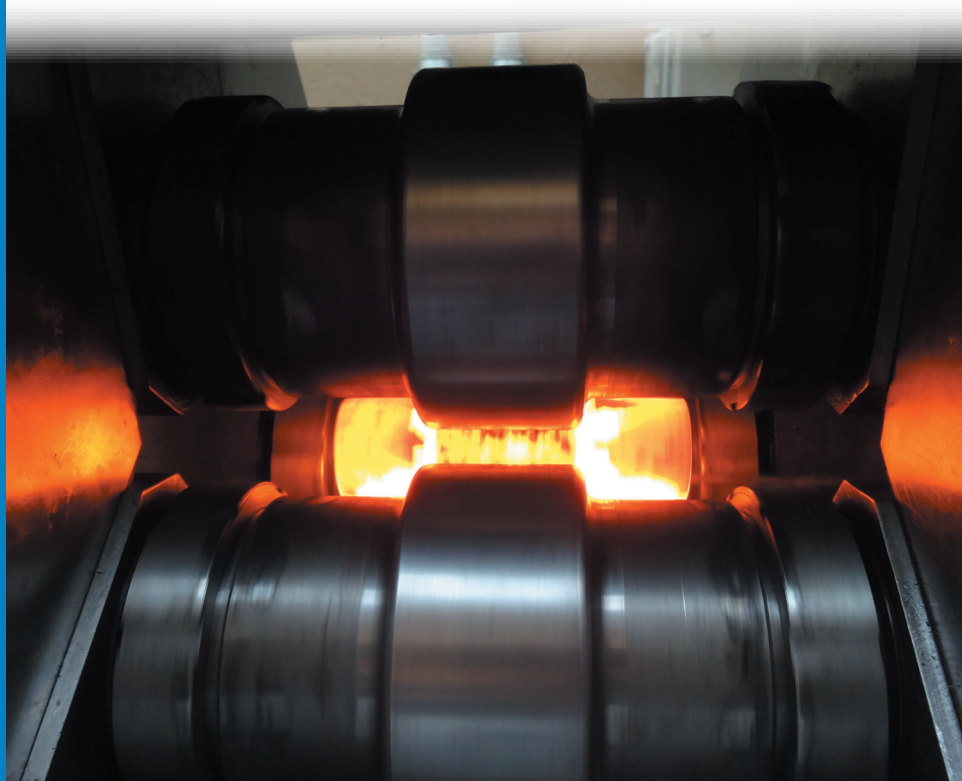

no. 3
year 2015
volume 61

Strojniški vestnik – Journal of Mechanical Engineering (SV-JME)

Aim and Scope

The international journal publishes original and (mini)review articles covering the concepts of materials science, mechanics, kinematics, thermodynamics, energy and environment, mechatronics and robotics, fluid mechanics, tribology, cybernetics, industrial engineering and structural analysis.

The journal follows new trends and progress proven practice in the mechanical engineering and also in the closely related sciences as are electrical, civil and process engineering, medicine, microbiology, ecology, agriculture, transport systems, aviation, and others, thus creating a unique forum for interdisciplinary or multidisciplinary dialogue.

The international conferences selected papers are welcome for publishing as a special issue of SV-JME with invited co-editor(s).

Editorial Office
University of Ljubljana, Faculty of Mechanical Engineering
SV-JME, Aškerčeva 6, SI-1000 Ljubljana, Slovenia
Phone: 386 (0)1 4771 137
Fax: 386 (0)1 2518 567
info@sv-jme.eu, http://www.sv-jme.eu

Print: Grafex, d.o.o., printed in 380 copies

Founders and Publishers
University of Ljubljana, Faculty of Mechanical Engineering, Slovenia
University of Maribor, Faculty of Mechanical Engineering, Slovenia
Association of Mechanical Engineers of Slovenia
Chamber of Commerce and Industry of Slovenia, Metal Processing Industry Association

Cover:
Hollow parts are applied in a variety of structures, from automotive and aircraft designs to household appliances. When solid parts such as drive axes and shafts are replaced with their hollow counterparts, the weight of mechanical structures is greatly reduced. Lower vehicle or aircraft weight, in turn, means a higher power of the engine and reduced fuel consumption. The interest of the automotive and aircraft sectors in hollow parts is due to rigorous emission standards for engines. New manufacturing techniques are being researched and developed.
Courtesy: *Lublin University of Technology, Faculty of Mechanical Engineering, Poland*

ISSN 0039-2480

General information

Strojniški vestnik – Journal of Mechanical Engineering is published in 11 issues per year (July and August is a double issue).

Institutional prices include print & online access: institutional subscription price and foreign subscription €100,00 (the price of a single issue is €10,00); general public subscription and student subscription €50,00 (the price of a single issue is €5,00). Prices are exclusive of tax. Delivery is included in the price. The recipient is responsible for paying any import duties or taxes. Legal title passes to the customer on dispatch by our distributor.

Single issues from current and recent volumes are available at the current single-issue price. To order the journal, please complete the form on our website. For submissions, subscriptions and all other information please visit: *http://en.sv-jme.eu/.*

You can advertise on the inner and outer side of the back cover of the journal. The authors of the published papers are invited to send photos or pictures with short explanation for cover content.

We would like to thank the reviewers who have taken part in the peer-review process.

The journal is subsidized by Slovenian Research Agency.

Strojniški vestnik - Journal of Mechanical Engineering is available on http://www.sv-jme.eu, where you access also to papers' supplements, such as simulations, etc.

Contents

Strojniški vestnik - Journal of Mechanical Engineering
volume 61, (2015), number 3
Ljubljana, March 2015
ISSN 0039-2480

Published monthly

Papers

Strojniški vestnik - Journal of Mechanical Engineering 61(2015)3,149-156
DOI:10.5545/sv-jme.2014.1977
Original Scientific Paper
Received for review: 2014-05-26
Received revised form: 2014-09-15
Accepted for publication: 2015-01-06

The Effect of Billet Wall Thickness on the Rotary Compression Process for Hollow Parts

Janusz Tomczak* – Tomasz Bulzak – Zbigniew Pater
Lublin University of Technology, Poland

This paper presents the numerical and experimental results of investigating the effect of geometrical parameters of tubular specimens on the rotary compression process for hollow axisymmetric shafts with central necking, and their accuracy. The numerical investigation was performed using the finite element method (FEM) with the Simufact Forming simulation software suite. The simulations investigated the effect of tubular specimen wall thickness on the kinematics of metal flow and the geometry of produced shafts. The results were validated in experimental tests using a forging machine designed specifically for this purpose.
Keywords: rotary compression, hollow parts, finite element method, experiment

Highlights
- *A new method for producing hollow parts is presented.*
- *The relationship between the wall thickness of a tubular specimen and rotary compression is investigated.*
- *The effect of wall thickness on the rotary compression process is studied both numerically and experimentally.*
- *The distributions of effective strain and temperature are determined by the finite element method.*
- *The variations in length and thickness of the work piece wall are determined, too.*

0 INTRODUCTION

Hollow parts, such as stepped axes, shafts, tubes, rings and many other axisymmetric parts, have a variety of applications, from automotive and aircraft structures to household appliances [1]. Due to their being highly in demand, hollow parts with finishing allowances are increasingly produced by metal-forming processes [2]. Compared to machining, metal-forming methods for producing hollow parts ensure reduced material consumption as well as enhanced strength properties of parts (fibre continuity is maintained). It should, however, be noted that the majority of current metal-forming processes for hollow parts are significantly complicated [3]. As a result, it is expensive to run them and, hence, to implement new technologies [4]. For this reason, new highly-efficient methods for forming hollow parts are being developed to ensure the production of parts with the required geometry and strength at the lowest costs possible.

The innovative methods for forming hollow parts from tubular billets include hydroforming and the RoProFlex method developed by the Institute of Forming Technology and Lightweight Construction (IUL) in Dortmund, Germany. The hydroforming technique is used to produce hollow complex-shaped parts that cannot be produced as monolithic components by other techniques. Parts produced by hydroforming are applied in automotive and aircraft industries. The main disadvantages of hydroforming include the high costs of tools, the slow speed of the process, and a lack of information about the process and tool design [5]. The RoProFlex method can be used to form any cross sections of tubes and sections along their longitudinal axis. Thanks to the numerical control of tool motion, this method can be used to produce parts with limitless variations of their cross sectional geometry. The RoProFlex method is mainly applied to produce light car parts, precise elements such as gears and helical rotors, as well as medical implants [6].

Rotary compression can be used to produce axisymmetric hollow shafts, including toothed shafts with straight, helical and herringbone teeth, as well as worms. In contrast to hydroforming and RoProFlex, this technique can be employed to form parts with thicker walls. The machine for rotary compression has a very simple design. The disadvantage of rotary compression is that this technique cannot be used to produce non-axisymmetric parts that can, however, be produced by hydroforming and RoProFlex.

One of the innovative methods for forming axisymmetric hollow parts is rotary compression shown in Fig. 1.

Rotary compression is a metal-forming operation based on the technique of cross rolling with three rolls, in which the tools not only rotate, but they also simultaneously travel towards the axis of the work piece. In this process, sections of commercial tubes or sleeves are rotated and deformed to reduce the diameter of steps. Compared to current techniques for manufacturing hollow shafts, rotary compression

*Corr. Author's Address: Lublin University of Technology, 36 Nadbystrzycka Str., 20-618 Lublin, Poland, j.tomczak@pollub.pl

offers numerous benefits, including lower forming forces, reduced material consumption, increased strength properties of produced parts, enhanced process efficiency, lower implementation and production costs, as well as simple design of the process and the possibility of its automation. Given the above benefits, it can be claimed that rotary compression can be applied in the industry. Therefore, the present investigation undertakes both theoretical and experimental analyses to develop relationships between the individual parameters of the rotary compression process for hollow parts and product quality.

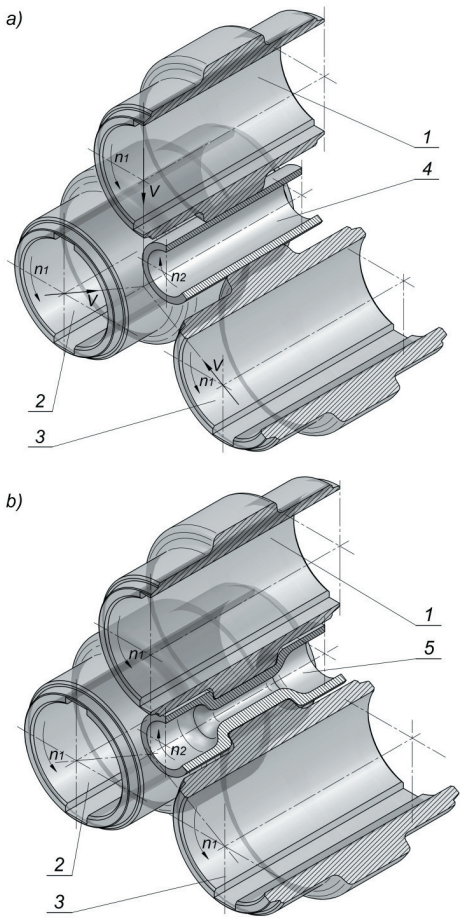

Fig. 1. *Schematic diagram of the rotary compression process for hollow shafts; a) start of the process, and b) end of the process; 1, 2 and 3 working rolls, 4 specimen, 5 finished part*

1 FEM MODELLING OF THE ROTARY COMPRESSION PROCESS

The present investigation mainly deals with presenting the effect of wall thickness of tubular specimens on rotary compression and product quality in the course of forming hollow necking in the centre of a shaft. The geometry of the work piece is determined by the reduction ratio ($\delta = D/d$) of the step (where: D is the outer diameter of the tubular specimen, d is the outer diameter of the step), which was set to 1.5 and of the initial wall thickness to of the tubular specimen set to 3, 5, 7, 9 and 11 mm, respectively. The shape and dimensions of the tubular specimen and of the desired final product are shown in Fig. 2.

First, the rotary compression process for a hollow shaft was modelled numerically. The computations were performed by the finite element method (FEM) using the Simufact Forming simulation software suite version 12.0, which the authors had previously used to investigate rotary processes for forming metals.

The geometrical model of the process developed for the purposes of the numerical analysis was identical to the schematic design of rotary compression shown in Fig. 1. The model consisted of three identical forming rolls and a tubular specimen (a C45 steel tube that had an outer diameter, D, of 42.4 mm, a wall thickness, t_o of 3, 5, 7, 9, 11 mm and a length, L, of 120 mm), modelled by means of first-order eight-node hexahedral elements. The model of C45 steel used in the computations was taken from the library database of the software used and is defined by:

$$\sigma_p = 2859.85 \times e^{(-0.00312548 \times T)}) \times \varepsilon^{(0.000044662 \times T - 0.101268)} \times \times e^{\frac{(-0.000027256 \times T + 0.000818308)}{\varepsilon}} \times \dot{\varepsilon}^{(0.000151151 \times T - 0.00274856)}, \quad (1)$$

where T is the temperature (ranging from 700 to 1250 °C), ε is the effective strain, $\dot{\varepsilon}$ is the strain rate.

At the initial stage of the process, the tubular specimen was heated throughout its volume to a temperature of 1150 °C, while the temperature of the tools was maintained constant at 100 °C. In the experiments, the tools were heated to a temperature of 100 °C with a gas burner. The temperature of the tools was monitored using a Flir T425 thermal imaging camera. The rolls were rotated in the same direction at a constant velocity n = 36 rpm, and simultaneously travelled relative to the axis of the work piece at a constant velocity v = 2.0 mm/s. The friction factor m on the material-tool contact was set to 1 **[7]**, the material-tools heat transfer coefficient was 30 kW/m²K **[8]**, while the heat transfer coefficient between the material and the environment was set to 0.35 kW/m²K **[9]**.

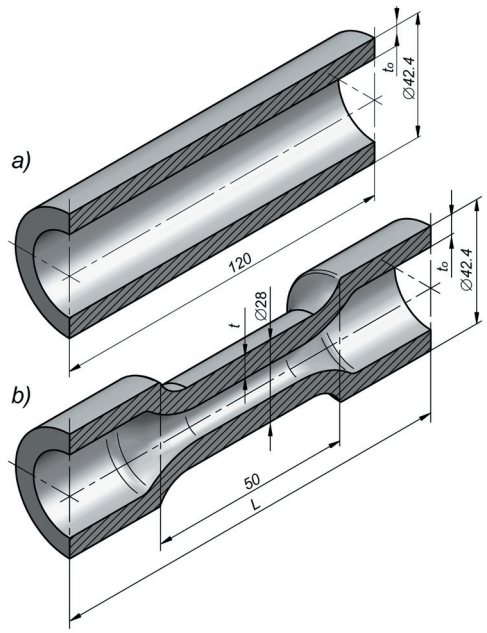

Fig. 2. *Shape and dimensions of a) tubular specimen, b) hollow shaft*

During the process, the rotating tools form necking in the centre of the shaft, which is accompanied by rapid metal flow radial to the axis of the work piece, thus leading to an increase in the thickness of the walls in this region. Furthermore, it can be noted that the material travels along the axis of the tubular specimen, which results in an increase in the work piece length. At the final stage of the process (i.e. sizing), the tools only perform a rotational motion, removing inaccuracies produced in the previous stages of the process. The FEM-determined geometry of hollow shafts and the effective strains for tubular specimens with different initial thickness of the wall are illustrated in Fig. 3. It is characteristic of the strains that they are distributed in a non-uniform manner. In all examined cases, the highest strains are concentrated on the outer surface of the work piece wall. The closer it is to the internal wall, the smaller the strains are. Such a distribution of strains is typical of rotary metal-forming processes and can be attributed to the kinematics of tool and work piece motion. Considerable slipping between the material being formed and the tools, as a result of which additional deformations are generated in the circumferential direction (by friction forces) on the work piece surface, can be observed. That increasing the initial thickness of the tubular specimen wall not only leads to an increase in the maximum strains, but to a greater non-uniformity of these strains can also be observed. This results from higher resistances to flow of the material during the forming of tubular specimens with thicker walls.

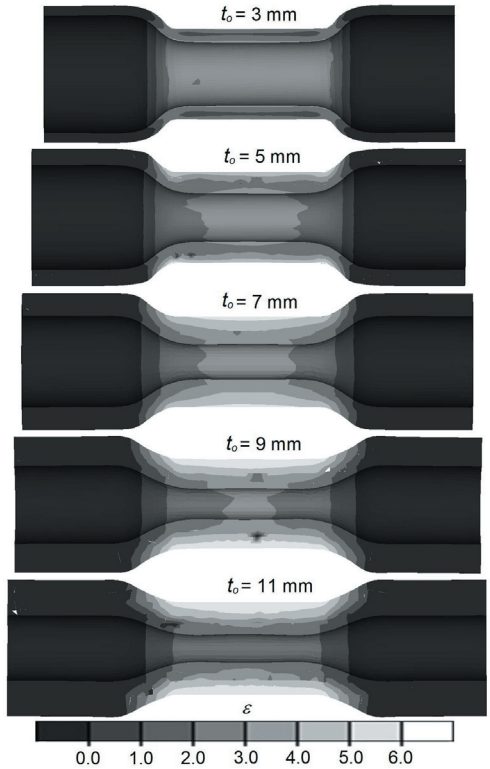

Fig. 3. *FEM-calculated distributions of effective strains in the final stage of the process for tubular specimens with various wall thicknesses*

The heat capacity of the hollow tubular specimens is much lower than that of the solid tubular specimens, which means that the material cools faster, thus hindering the rotary compression process. For this reason, the present investigation involved determining the effect of tubular specimen wall thickness on temperature and its distribution. Fig. 4 shows the temperature distribution maps that were calculated by the FEM in the final stage of rotary compression for tubular specimens with various wall thicknesses.

As predicted, the distributions of the temperatures are not uniform; the highest drops in the temperature can be observed in the region of the necking being formed. The non-uniform distribution pattern of the temperature in the region of the necking being formed results from the nature of the rotary compression process. During this process, the outside layers of the work piece are in contact with the colder tools, thus carrying heat away to the tools. In contrast, the inside layers of the work piece lose heat mainly due to heat exchange with the environment. The non-

uniform temperature distribution in the region of the necking being formed results from that fact that heat is transferred at a more rapid rate to the tools than to the environment. The amount of heat transferred from the work piece to the tools and the environment is determined by the heat transfer coefficients, the magnitudes of which are given in the section describing the numerical model.

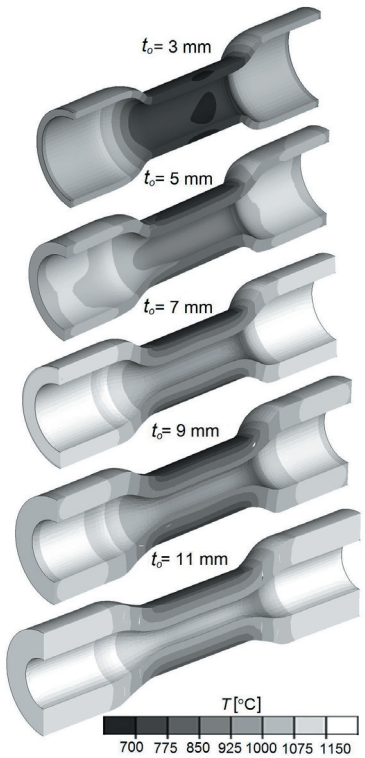

Fig. 4. *FEM-calculated distributions of the temperature in the final stage of the process for tubular specimens with various wall thicknesses*

The design of this forming process assumed that the external steps would not be in contact with the tools. As a result, they did not undergo deformation and their temperature was relatively uniform and high (above 1000 °C). Examining the distribution of the temperature in the zone where the tools have a direct impact on the tubular specimen, it can be observed that the highest drop in the temperature occurs when the tubular specimens with small wall thickness are used (low heat capacity of the tubular specimen). In addition, the forming of tubular specimens with relatively thin walls leads to the cooling of the material, practically over the entire section of the reduced step, and the temperature distributions in the reduction area are quasi-uniform. In contrast, the distributions of the temperature for tubular specimens with thicker walls differ: the temperature drops locally (on the surface). The farther it is from the surface layers that directly contact the tools, the higher the temperature. In effect, such a temperature distribution pattern enables the heat to flow from the inner to outer surfaces of the work piece, so that the temperature of the step is high enough for a relatively long time for the hot forming of this step. The rotary compression of tubular specimens with small thickness of their walls is, however, harder to perform, as the rapid and excessive cooling of the material across the entire section of the step being formed leads to a decrease in workability of the material and an increase in resistances to forming.

2 EXPERIMENTAL TESTS OF THE ROTARY COMPRESSION PROCESS FOR PRODUCING HOLLOW SHAFTS

The numerical results were verified experimentally under laboratory conditions. To perform the experiments, we used a forging machine as shown in Fig. 5. With this machine, the process can be run in accordance with the pattern of the numerical simulations. Force and kinematics parameters of the rotary compression process were measured with a measuring system comprised of the following elements: a torque transducer to digitally record torque during forming; a displacement transducer to record velocity and position of the tools; pressure transducers to measure pressure in order to determine the force of the tools acting on the work piece.

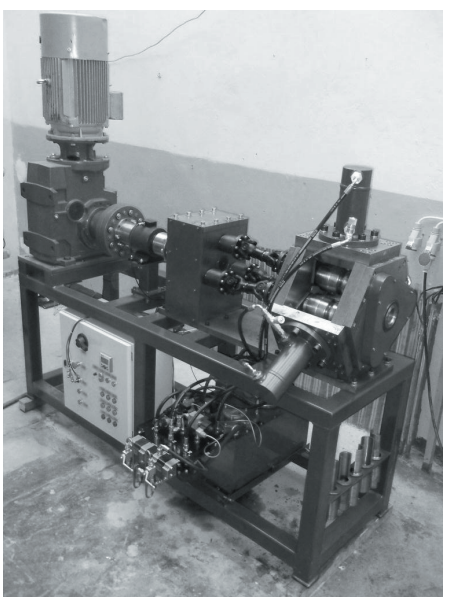

Fig. 5. *Machine used in the experiments of the rotary compression process for hollow shafts*

The tubular specimens used in the experiments were C45 steel tubes of the same dimensions as those applied in the FEM simulation. The tubular specimens were first heated in an electrical chamber furnace to a forming temperature of approx. 1150 °C, then they were fed by tongs into a special feed mechanism to position the tubular specimen in the working space of the machine (formed by three rotating rolls – Fig. 6a). In the subsequent stage of the process, the tools travelled radially at a constant velocity v = 2 mm/s and were rotated in the same direction at a velocity n = 36 rotations per minute, consequently setting the tubular specimen into a rotational motion and, thus, reducing the diameter of the step in the centre of the work piece. Once the slides travelled the path of the required diameter reduction ($\delta = D/d = 1.5$), the translational motion was automatically stopped. After the actual forming operation, the work piece was sized into the desired shape between rotating rolls. At the final stage of the process, the tools were opened radially (Fig. 6b) and the finished part was removed from the working space of the machine in a special feed mechanism.

The primary aim of the experiments was to verify whether the geometrical models applied in the numerical analysis were correct and to validate whether the rotary compression process is suitable for forming hollow stepped shafts. In the experiments of forming hollow tubular specimens with various wall thicknesses into shafts, we also analysed the geometrical parameters of finished products, process stability and forces. The experimental results obtained explicitly demonstrate that the proposed technique can be employed to form hollow tubular specimens into hollow stepped axes and shafts. The experimental results regarding the shapes and dimensions of produced parts agree well with both the theoretical assumptions (work piece shape assumed at design) and the numerical results. Fig. 7 shows the hollow shafts with various wall thicknesses produced in the experiments. As can be seen from Fig. 8, the thickness of the work piece walls increases, which is caused by the material's radial flow. Furthermore, it was observed that the length of all parts increased compared to the initial length of the tubular specimens, which results from the axial displacement of the material. It should however be stressed that the material flows axially mainly in the region where the tools have various radii, thus leading to a decrease in wall thickness in the region between the step being formed and the non-deformed steps of the work piece. The thinning of the wall can be significantly reduced or even eliminated by preventing free work piece elongation during the process.

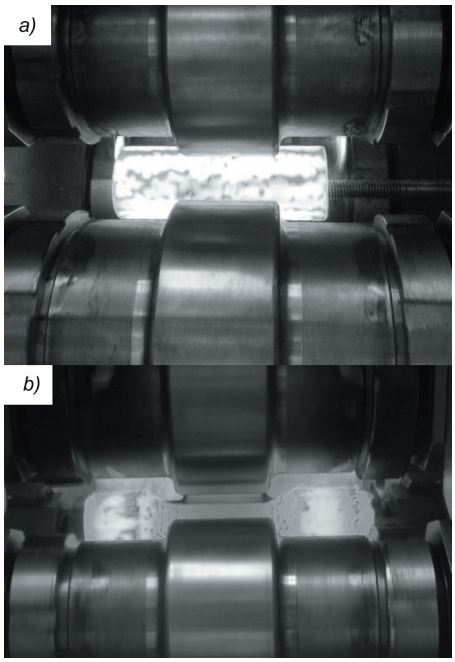

Fig. 6. *Rotary compression process for producing hollow shafts; a) start of the process, and b) end of the process*

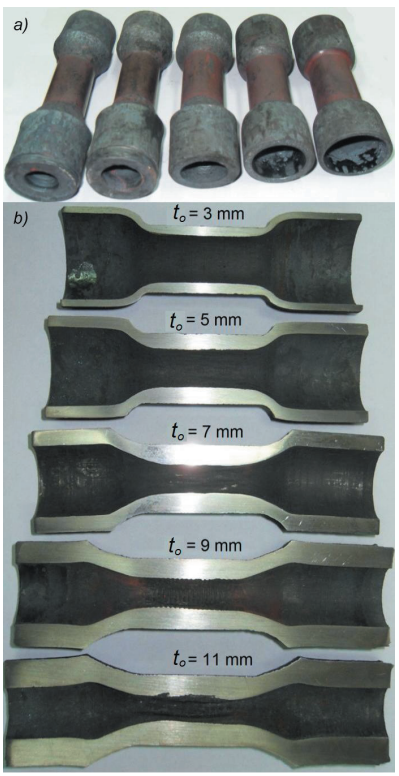

Fig. 7. *Hollow shafts produced in the experiments from hollow tubular specimens with various wall thicknesses; a) general view, and b) axial sections*

In spite of the above, we can observe that the region between the end and central steps of the work piece is characterized by local thinning of the work piece wall. Apart from the local thinning of the work piece wall, a small arching of the axis of the shaft is noted, especially in regard to shafts formed from tubular specimens with thicker walls. This defect is caused by the lack of support for the work piece in the zone of the end steps that were not in contact with the tools during the process.

Examining the geometry of the produced parts (Fig. 7), it can be observed that the initial thickness of a tubular specimen wall has a significant effect on the kinematics of material flow during the rotary compression process. The reduction in the outer diameter leads to a change in the wall thickness and work piece length.

It is to be noted, however, that the relative increase in the wall thickness of the necking formed (compared to the initial thickness) decreases as the initial tubular specimen wall thickness increases (Fig. 8); what is more, in the case of the tubular specimen with the thickest wall (t_o = 11 mm), a small loss of thickness of the wall in the formed step of the shaft can be observed. A reverse trend can be observed with regard to length of formed shafts. Here, the increase in the initial wall thickness leads to an increase in

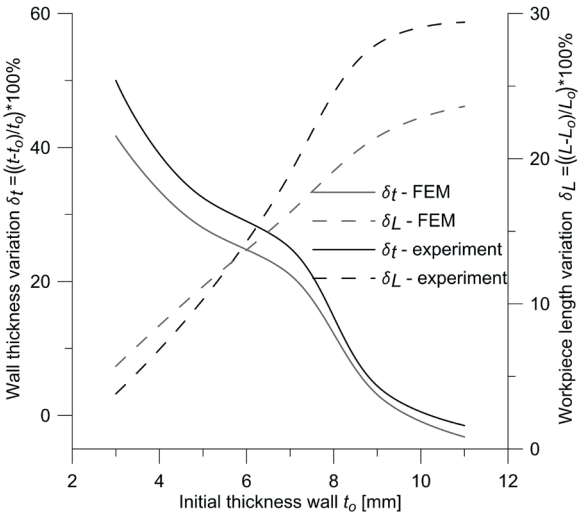

Fig. 8. *Variations in the wall thickness and work piece length as determined by FEM and in the experiments*

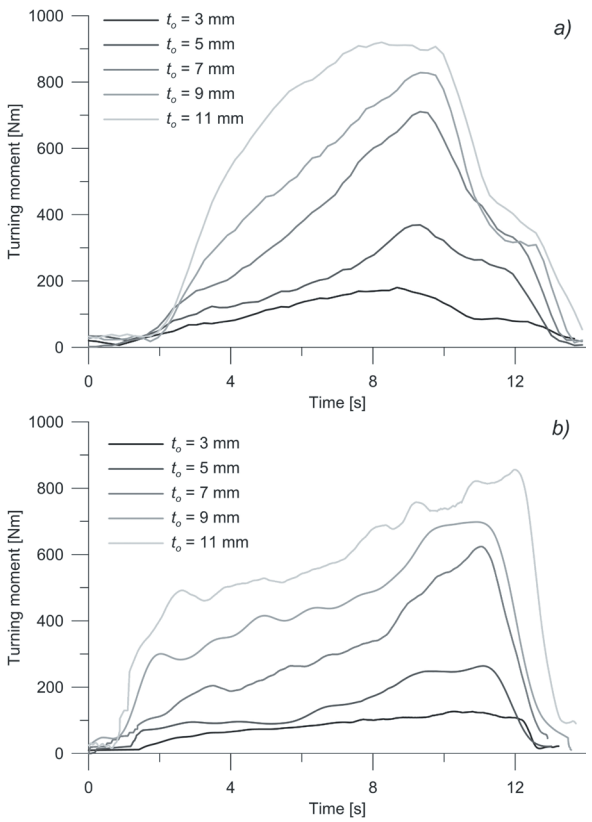

Fig. 9. *Torque in the rotary compression for hollow shafts with various initial wall thicknesses; a) experiment, and b) FEM*

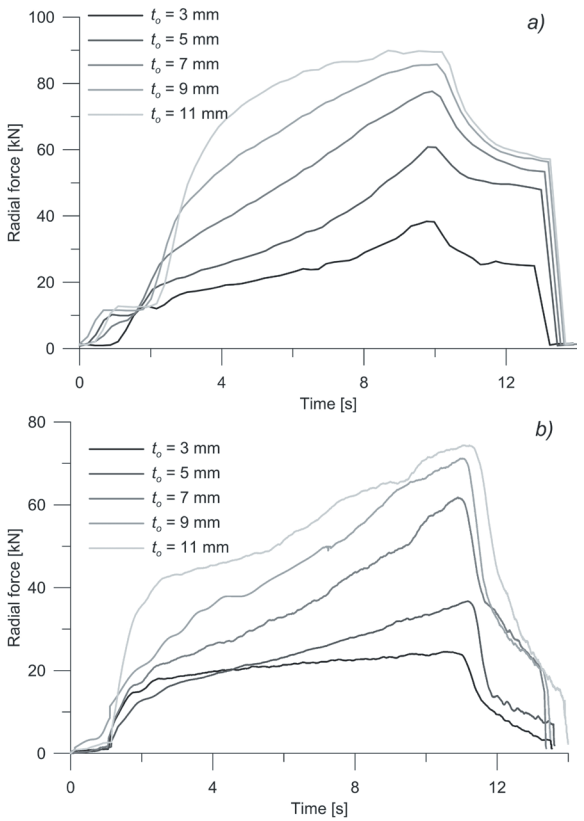

Fig. 10. *Force in the rotary compression process for hollow parts with various initial wall thicknesses; a) experiment, and b) FEM*

length of the shaft. The observed relationship directly results from the differences in resistance to material flow that depend on tubular specimen wall thickness. In the forming of thin-walled tubular specimens, the resistances to the radial flow of the material are much lower than those observed when the material flow is axial, which leads to a rapid increase in the thickness of the walls of the shafts. With thicker walls, the material's axial flow is free from such resistances, which results in a rapid increase in the length of the shaft.

The theoretical and experimental analyses were also performed to investigate forces and torques of the process, the variations of which are shown in Figs. 9 and 10. It can be noted that an increase in the thickness of a tubular specimen wall leads to an increase in the forces and torques. The nature of the variations in the force parameters is similar in all investigated cases. Initially, the forces and torques increase rapidly with the sinking of the tools into the material; in the steady-state stage of the process, the increase in the forces is stable and gentle. Then, at the final stage of the process, a rapid decrease in the forces and torques can be observed. There are, however, differences between the FEM-calculated variations in the forces and torques and those obtained in the experiments. The experimental results demonstrate that the forces increase much faster over time compared to the variations of the forces obtained in the FEM modelling. Moreover, the forces and torques are higher in the experiments (the differences can even amount to several percentage points in the case of tubular specimens with thin walls). The observed differences can result from the fact that the material cools faster in the experiments than in the numerical modelling. This is proved by the considerably lower differences in values of the forces obtained in the forming of tubular specimens with thicker walls. Owing to the higher heat capacity of the tubular specimens, the temperature of the tubular specimen is relatively high, thus ensuring sufficient material workability.

3 DISCUSSION AND CONCLUSIONS

The majority of currently employed metal-forming techniques for hollow parts are highly complicated and relatively expensive; they only become cost-effective in mass production. The proposed new rotary compression method for hollow parts can be successfully employed in both small series and mass production, as it is based on the use of simple tools and devices. Furthermore, the use of hollow tubular specimens in rotary compression leads to lower consumption of both material and energy, which, in turn, results in lower production costs.

The theoretical and experimental analyses of the rotary compression process have confirmed that stepped hollow shafts can be produced from hollow tubular specimens. The analyses led to a determination of the effect of work piece geometry on rotary compression and the geometry of finished parts. Furthermore, the force parameters of the process were investigated. Most importantly, however, the investigation helped validate the developed numerical model of the rotary compression process. Based on the results, the following conclusions have been drawn:

1. The numerical and experimental results show satisfactory agreement, which means that rotary compression processes can be modelled numerically.
2. Rotary compression can be employed to shape hollow tubular specimens of various wall thicknesses into stepped axes and shafts.
3. Parts produced by rotary compression processes exhibit higher wall thickness of steps and higher overall length of the work piece.
4. The rotary compression process for hollow parts involves non-uniform deformations; the greater the non-uniformity is, the higher the initial thickness of the tubular specimen wall is.
5. When tubular specimens with small initial wall thicknesses are formed into hollow parts, the material undergoes rapid cooling, which may hinder the rotary compression process.
6. An increase in the initial wall thickness of the tubular specimen leads to an increase in the tool force and torque.
7. Further research should be undertaken to determine failure modes and relationships between the technological parameters of the compression process and the geometry of tubular specimens and work piece.

4 ACKNOWLEDGEMENTS

The study was conducted as part of the project "Qualifications for the labour market - employer friendly university", co-financed by European Union from European Social Fund.

5 REFERENCES

[1] Opalić, M., Kranjčević, N., Habuš, S. (2011). Proof of strength of shafts and axles using finite element method. *Transactions of FAMENA*, vol. 35, no. 2, p. 63-71.

[2] Neugebauer, R., Kolbe, M., Glass, R. (2001). New warm forming processes to produce hollow shafts. *Journal of Materials Processing Technology*, vol. 119, no. 1-3, p. 277-282, **DOI:10.1016/S09240136(01)00936**.

[3] Neugebauer, R., Glass, R., Hoffmann, M. (2005). Spin Extrusion - A New Partial Forming Technology based on 7 NC-Axes Machining. *Annals of the CIRP*, vol. 54, no 1, p. 241-244, DOI:**10.1016/S0007-8506(07)60093-6**.

[4] Stanić, I., Galeta, T., Karakašić, M. (2008). Optimization of protecting wall tool for manufacture and assembly. *Technical Gazette*, vol. 15, no. 1, p. 45-49.

[5] Pepelnjak, T. (2004). Numerical Analyses of Tube Hydroforming by High Internal Pressure. *Strojniški vestnik - Journal of Mechanical Engineering*, vol. 501, no. 1, p. 31-43.

[6] Staupendahl, D., Becker, C., Weinrich, A., Hermes, M., Tekkaya, A.E. (2012). Innovative forming processes for tubes, profiles and sheets made of modern steel grades. *Stahl und Eisen*, vol. 132, no. 8 p. 47-54.

[7] Jia, Z., Zhou, J., Ji, J.J., Yu, Y.-Y., Xiao, C. (2012). Influence of tool parameters on internal voids in cross wedge rolling of aluminum alloy parts. *Transactions of Nonferrous Metals Society of China*, vol. 22, suppl. 1, p. 21-26, **DOI:10.1016/S1003-6326(12)61678-1**.

[8] Dadras, P., Wells, W.R. (1984). Heat transfer aspects of nonisothermal axisymmetric upset forging. *Journal of Engineering for Industry*, vol. 106, no. 3, p. 187-195, **DOI:10.1115/1.3185932**.

[9] Malinowski, Z., Lenard, J.G., Davies, M.E. (1994). A study of the heat-transfer coefficient as a function of temperature and pressure. *Journal of Materials Processing Technology*, vol. 41, no. 2, p. 125-142, **DOI:10.1016/0924-0136(94)90057-4**.

Strojniški vestnik - Journal of Mechanical Engineering 61(2015)3, 157-166
DOI:10.5545/sv-jme.2014.2051
Original Scientific Paper
Received for review: 2014-07-08
Received revised form: 2014-11-26
Accepted for publication: 2014-12-10

Investigations on the Effects of Different Tool Edge Geometries in the Finite Element Simulation of Machining

Lei Wan – Dazhong Wang* –Yayun Gao
Shanghai University of Engineering Science, College of Mechanical Engineering, China

This work focuses on the effects of cutting edge geometries on dead metal zone formation, as well as stress and temperature distributions in orthogonal cutting of P20 material using finite element method (FEM) simulation with sharp, chamfered, double chamfered and blunt tools. The cutting process is simulated with Arbitrary Lagrangian-Eulerian (ALE) approach in ABAQUS/Explicit. The simulation results suggest that the tool edge geometry influences the shape of dead metal zone considerably, while having little influence on the chip formation. An analysis of thermo-mechanical coupling was also conducted, and the results show that the stress distribution is affected by the temperature distribution and cutting speed because of the thermal softening effect and the strain rate hardening. A common analytical model is introduced to predict the residual stress, and equivalent Mises residual stresses are all calculated with four different tools to suggest that the tool edge geometry has a significant effect on the residual stress. The experiments are conducted using a CNC with former four kinds of tools at a speed of 480 m/min, and the residual stresses beneath the machined surface were measured with X-ray diffraction and electro-polishing techniques, and a chamfer tool at three different cutting speeds (250, 600 and 1000 m/min) to obtain the forces. The machining forces in both the cutting and thrust directions increases as the chamfer angle increases and decreases as the cutting speed increases.
Keywords: tool edge geometry, coupled thermo-mechanical analysis, finite element method, dead metal zone, residual stress

Highlights
- *Proposing a newly model of the tool edge geometry to analyze the effect of tool edge on the cutting process.*
- *Four different kinds of tool edge geometries are consider in this analysis.*
- *Finite element method (FEM) are utilized in cutting process.*
- *Dead metal zone is formed under different tool edge geometries and varies with the shape of the tool edge geometry.*
- *Stress and residual stress are influenced by the tool edge geometry.*
- *The simulated results are validated with the analytical and experimental results and the forces obtained from simulation, analysis and experiments are compared.*

0 INTRODUCTION

Metal cutting is always considered to be one of the most complicated manufacturing processes for different materials. In order to attain sufficiently high production rates at minimal cost, optimization of cutting tool geometry is necessary. Moreover, the cutting process is greatly influenced by the cutting conditions, such as cutting velocity, chip thickness, and feed rate, as well as the tool geometry. The design of tool edge geometry influences process parameters, such as the shape of deformation zones, stresses on the chip and machined surface and the cutting forces mentioned in Fig. 1 **[1]**. These effects in turn affect the changes in chip flow and machined surface integrity. The modification of the tool edge geometry is referred to edge preparation. Fig. 2 illustrates four major types of edge preparation design used in most commercial cutting inserts: sharp edge; hone edge; T-land/chamfer edge and double chamfer edge. Moreover, Regions 1, 2, 3 are the missing regions of blunt, double chamfer and chamfer tools compared with the sharp tool, respectively.

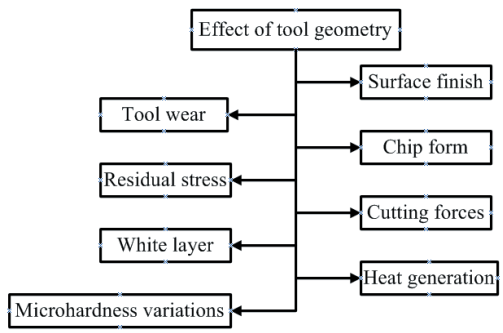

Fig. 1. *Effect of tool geometry on performance parameters in turning*

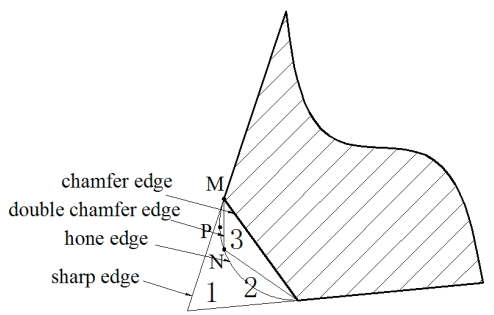

Fig. 2. *Typical cutting edge preparation*

*Corr. Author's Address: Shanghai University of Engineering Science, 333 Longteng Road, Shanghai, China, wdzh168@hotmail.com

Much research has been conducted about how the edge geometry of tools influenced the cutting process, analytically and experimentally [2]. Experimental results of a study done by El-Wardany et al. [3] show that for a sharp tool (compared with other geometries) the magnitude of the residual stress on the machined surface and the penetration depth of the stressed layer were reduced as cutting speed increased, while there is an opposite trend for the hone tools. Based on the large numbers of experiments, which were conducted with CBN tools for carburized hardened steel (600 to 720 HV) under both continuous and interrupted cutting conditions, Shintani et al. [4] and [5] analysed the effect of tool geometry on the cutting performance. They proposed that the optimum tool geometry for continuous cutting be specified as having a negative chamfer angle of 35° and a nose radius of 0.8 mm. Matsumoto et al. [6] investigated four different tool edge geometries (sharp, honed, single chamfered and double chamfered) on residual stress in precision hard turning, and concluded that tool edge geometry is the dominant factor determining the residual stress profile, and the residual stress with the honed and chamfer tool on the machined surface became more compressive. In recent decades, with the improvement of the computer technology, the finite element method (FEM) and numerical simulation have been increasingly used to study the machining process. Kountanya et al. [7] studied the effect of tool geometry and cutting conditions on experimental and simulated chip formation. Some observations can be obtained to illustrate that the machining forces increase as the tool edge radius increases, and the change of edge radius has little influence on chip morphology. Shatla et al. [8] applied the Lagrangian FEM to simulate the cutting process of H13 tool steel to investigate the influence of edge preparation (hone/chamfer) on tool temperature and stress. The simulation results showed that an increasing tool edge radius alters the distribution of temperature in the different kinds of tools, while the experiment results also indicated that the cutting force increases as the tool edge radius increases.

When studying the influence of the tool geometry on the metal cutting process, one of the main points of interest is the existence of the dead metal zone under the chamfer or around the edge radius of the tool. The dead metal zone is trapped under the chamfer and almost entirely fills the chamfer, which acts as the effective cutting edge of the tool, thus protecting the tool surface from wear under various kinds of heavy cutting conditions. The drawbacks of cutting with a dead metal zone on the chamfered edge are that the forces on the tool increased, and the simulation results may be inaccurate due to the varying dead zone during cutting. Experimental and analytical studies discussed in [9] to [11] concluded that a dead metal zone is mostly dependent on the geometry of the chamfered part rather than the cutting conditions. Meanwhile, the dead zone is also formed with the blunt tool in the same way as for the chamfered tool, which is in good agreement with the results of assumption of the formation of BUE discussed by Waldorf et al. [12] for large-radius tools. The region of the missing zone determines the region of the dead zone. The surface finishing may depend greatly on the size and the shape of the dead zone. Al-Athel and Gadala [13] proposed a new volume of solid (VOS) method to simulate the metal cutting process with four different geometries tools. The simulation results suggest that the tool geometries have great influence on the formation of the dead metal zone, but little effect on the distribution of stress. Jacobson et al. [14] conclude that various kinds of dead zones near the tip of the tool may occassionaly become unstable in form and size, and sometimes crack partially or even entirely, resulting in deposits on the tool surface.

From this background information, it can be determined that the above mentioned authors have the common view that the tool edge geometries significantly influence dead metal zone formation and residual stress distribution, but not the chip formation and the stress distribution. Aiming at these hypotheses, this paper presents a numerical analysis of a continuous chip formation process based on the finite element method for a better understanding of dead metal formation and chip formation. The effects of four common kinds of tool edge geometries on the formation of the dead metal zone and how they affect the distributions of stress and temperature have been studied.

1 NUMERICAL SIMULATION

1.1 Numerical Approach

Numerical simulation of the cutting process can provide detailed results for process variables, such as stress, strain, strain rate, temperature, that are extremely difficult to measure with current technology. Owing to advanced technology and computer power, an alternative approach called the arbitrary Lagrangian-Eulerian (ALE) approach [13], which could combine the advantages of Lagrangian and Eulerian approaches, eliminating mesh distortion in Eulerian formulation and modeling the

unconstrained flow of the chip in Lagrangian approach was applied in this research. The ALE approach is proved to be viable once a proper mesh motion scheme been implemented, Fig. 3 [15]. The simulation results are compared with the numerical work done by Movahhedy et al. [16], who simulated the cutting process via the ALE approach with four different tools whose rake angles were 0°. The ALE model (shown in Fig. 4) developed by Muñoz-Sánchez et al. [17] allows the material to flow across an internal Eulerian zone surrounding the tool tip by using sliding Lagrangian and Eulerian contours. This method can avoid extreme mesh distortion and allows the simulation of a long machining time. The model is divided into four zones, allowing mesh motion or material flow across the fixed mesh. Zones 1 to 3 combine Lagrangian/ Eulerian boundaries with sliding boundaries where the material can flow tangential to the contour but not go across this boundary. Eulerian boundaries located at the entrance of Zone 1 and in Zone 2 can avoid the mesh distortion that is commonly revealed as the calculation advances. Zone 4 allows the material to flow across this region (which is a Eulerian region) with the mesh fixed. The main advantage of this technique is that it can avoid the extreme distortion in the region surrounding the tool tip. Therefore, it can be used to simulate a large machined surface in this paper.

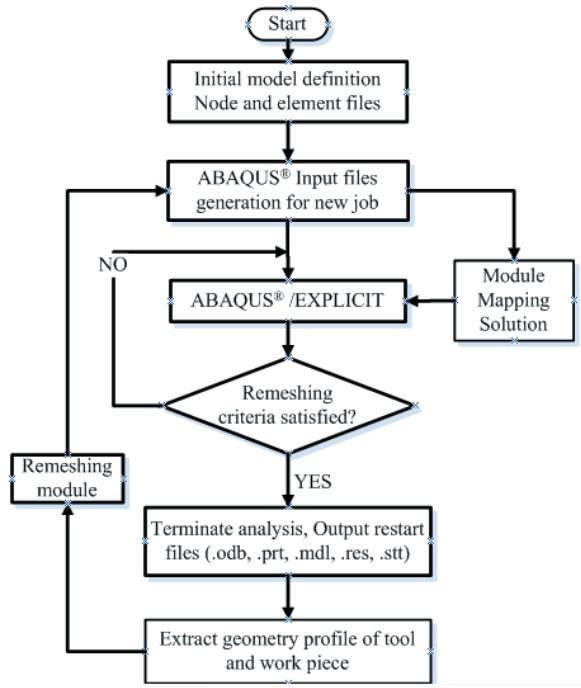

Fig. 3. *Overall simulation approach*

1.2 Boundary Conditions and Material Properties

Fig. 5 shows the schematic of the metal cutting process for a general case with a chamfer tool. The cutting force and thrust force are respectively defined by F_c and F_t. F_s and F_n represent the forces acting along and normal to the shear plane, respectively. The main rake angle and chamfer angles are defined as α_0 and α_1. The length of the chamfered part is defined as b_{cf}, material flow (V_c) splits into two parts at the front of the cutting edge, one part shapes the chip at speed of V_a, the other forms the machined surface at speed of V_b. Three deformation zones are shown in the graph.

The metal cutting process is so complicated that the finite element model should be simplified, and some assumptions established as well. The assumptions of finite element model are:

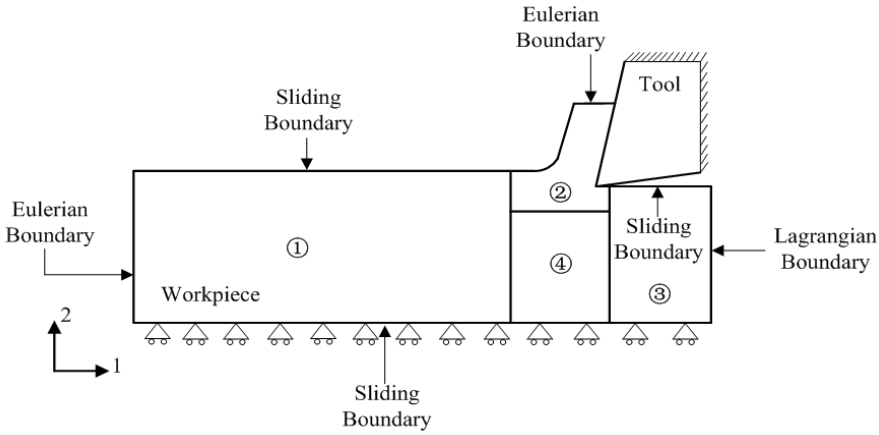

Fig. 4. *Implementation of boundary condition and type of contour in the model; regions 1 to 3 combine sliding and Lagrangian/Eulerian boundaries; region 4 combines Eulerian boundaries*

1. The workpiece material is isotropic.
2. The workpiece material accords with Von Mises yield criteria.
3. Machine tool bed and fixture are both rigid in the cutting process.

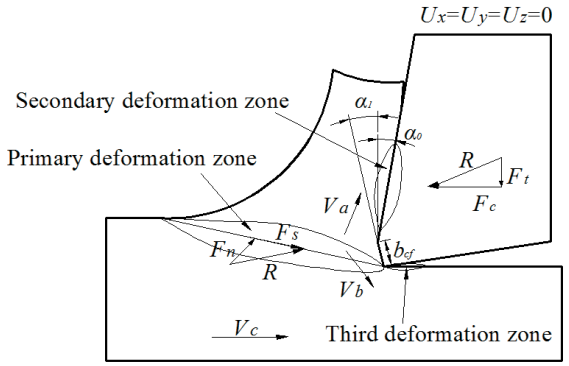

Fig. 5. *Schematic view of metal cutting process with double chamfered tool*

In the actual metal turning process, cutting width is much larger than the back engagement of the cutting edge, so the chip deformation, which is perpendicular to the cross-section of tool edge, is approximately same along the tool edge direction, which is called the plane strain state. Therefore, the metal cutting process can be regarded as a two-dimensional orthogonal cutting model when simulating the cutting process by using the FEM.

In this paper, basic geometry and boundary conditions of the numerical model are shown in Fig. 4, and a plain strain condition is assumed. The tool is fixed and cutting speed is applied to the workpiece to obtain the velocity field of the workpiece material, the rake angle is 10°, and the clearance angle is 7°. Material properties for the workpiece and tool are presented in Table 1.

Table 1. *Material properties for the workpiece and tool*

Material properties	Workpiece	Tool
Material	P20	Carbide tool
Young's modulus [GPa]	210	530
Poisson's ratio	0.3	0.3
Conductivity [W m^{-1} °C^{-1}]	51.5	120
Specific heat [J kg^{-1} °C^{-1}]	470	343.3
Thermal expansion coefficient [°C^{-1}]	1.4×10^{-6}	5.2×10^{-6}

In order to correctly simulate the cutting process with different tool geometry, it is necessary to introduce a material flow stress model to describe the material behaviour. The model is obtained from **[18]**, which considers high temperature and high strain rate, usually presented with the equation below:

$$\bar{\sigma} = (A + B(\bar{\varepsilon})^n)(1 + C\ln\left(\frac{\dot{\bar{\varepsilon}}}{\dot{\bar{\varepsilon}}_0}\right))(1 - (T^*)^m), \quad (1)$$

with the T^* is defined as:

$$T^* = \frac{T - T_r}{T_m - T_r}, \quad (2)$$

where $\bar{\sigma}$ is the equivalent flow stress, $\bar{\varepsilon}$ the equivalent plastic strain, $\dot{\bar{\varepsilon}}$ the equivalent plastic strain rate, $\dot{\bar{\varepsilon}}_0$ the reference strain rate, which equals 1 s^{-1}. The material characteristics are defined by the thermal softening coefficient m, the strain hardening exponent n, and constants adopted from **[13]**, which are listed in Table 2. T_m and T_r are the material melting temperature (1480 °C) and reference ambient temperature (20 °C), respectively.

Table 2. *J-C parameters for P20*

A [MPa]	B [MPa]	C	n	m
178.5	462.4	0.0438	0.169	0.666

1.3 Frictional Model

Whether the cutting simulation results are accurate and reasonable, to a large degree depends on the foundation of the frictional model; therefore, it is vitally important to choose a reasonable friction model. The rake face is divided into two workspaces, the sticking zone and the sliding zone, which is illustrated in Fig. 6.

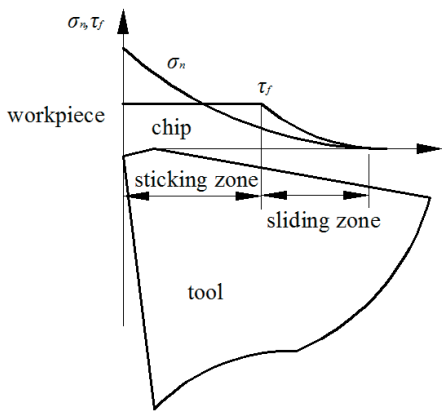

Fig. 6. *Curves representing normal and frictional stress distributions on the tool rake face*

Alvarez et al. **[19]** studied the effect of four different constitutive models and three friction

coefficients (0.4, 0.6 and 0.8) on the simulation results. They conclude that the friction factor depends on the constitutive equations and their parameters, and its election is subject to the experiment results. Thus, when considering machining simulations of P20, a moderate friction coefficient (0.4) is used in this study and friction at the tool-chip interface is controlled by a Coulomb friction model which is expressed by the following relations:

$$\tau = \mu\sigma_n, \quad \text{if} \quad \mu\sigma_n < \bar{m}\frac{\sigma_0}{\sqrt{3}}, \text{ (the sliding zone)} \quad (3a)$$

$$\tau = \bar{m}\frac{\sigma_0}{\sqrt{3}}, \text{ if } \mu\sigma_n < \bar{m}\frac{\sigma_0}{\sqrt{3}}, \text{ (the sticking zone)} \quad (3b)$$

The shear stress (τ) is either expressed by the product of Coulomb friction coefficient (μ) with normal stress (σ_n) or by a fraction ($\bar{m}$) of permissible shear stress of the workpiece material.

2 EXPERIMENTAL WORK

In this work, a disk made of P20 mould steel was turned in orthogonal mode on a CNC turning centre, and the cutting force and chip thickness were measured in each case. In the first set of tests, blank carbide tools of ISO S10 class were used with sharp and different chamfer angles α_1 and lengths b_{cf}, as listed in Table 3. The primary rake angle of the tool was 10° in all cases. A chip load of 0.1 mm and a cutting speed of 480 m/min were adopted. In the second set of tests, a chamfer tool with a primary rake angle of 10° and a chamfer angle of –25° and a chamfer length of 0.1 mm were used to cut P20 disks at three different cutting speeds of 250, 600 and 1000 m/min. The uncut chip thickness in this set was 0.06 mm. The produced chip was continuous in all cases.

Table 3. *Tool edge geometry in cutting tests with carbide tools*

Case	α_0 [°]	α_1 [°]	b_{cf} [mm]
1	10	0	–
2	10	–10	0.0902
3	10	–25	0.0841
4	10	–35	0.0863

The measurements of residual stress were conducted with an X-ray diffraction technique, and the measurement conditions used in this study are listed in Table 4 [20]. The measurements of residual stress were performed by using a '$\sin\phi$' method. An electro-polishing technique was utilized to determine the residual stress beneath the machined surface, and the maximum electro-polished depth from the machined surface is over 150 μm.

Table 4. *Conditions of X-ray diffraction*

Characteristic X-ray	Cr Kα
Diffraction plane	(2 1 1)
Diffraction angle	156.08°
Tube voltage	30 kV
Tube current	10 mA
Divergent angle	1.0°
Step angle	0.5°
Fixed time	0.4 s per step
Irradiated area	10×20 mm
Stress constant	-297.23 MPa/°

3 RESULTS AND DISCUSSION

3.1 The Existence of the Dead Metal Zone

Fig. 7 shows the velocity profile of the material under the same cutting condition with different edge geometry tools by ALE. It is obvious for the sharp tool that there is nearly no metal dead zone except for a small region where the material flow slows down because of the block of the tool corner. However, for the chamfered tool, it is clear that part of the material is trapped under the chamfer corner, which presents low speed and acts as the missing tool nose. It is much clearer that the tool of the –25° chamfer angle has the largest dead zone in comparison to the other three tools because of its larger missing region, to indicate that the zone is dependent on the tool geometry. As for the blunt tool, a dead metal zone presents to a lesser extent, because the fillet of the tool allows a smoother flow of the material along the surface.

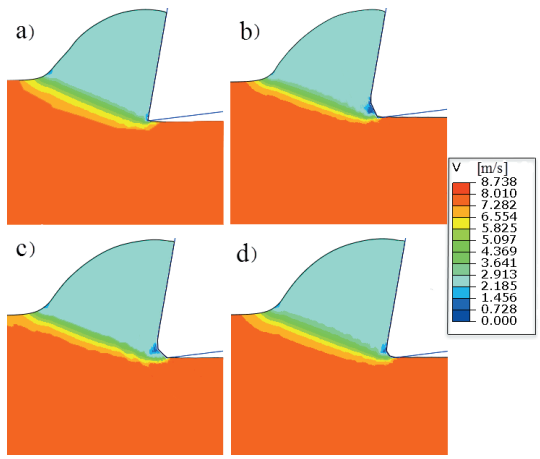

Fig. 7. *Velocity fields for; a) a sharp tool, b) 25° chamfered tool, c) double chamfered tool, and d) blunt tool*

The simulation results are compared with the simulations conducted by Movahhedy et al. [16] to discuss the position of the dead metal zone. The comparison illustrates that the rake angle affects the position of the dead zone significantly. It can be found that the positive rake angle will result in a shifting up of the dead zone, because the positive angle allows the material to follow past quickly along the rake face and the dead zone does not fill the missing region completely under the chamfer. It also can be found in these figures that the tips of the tools in these simulations have already intruded into the mesh of material at different extents because of the quality of the mesh. It can be solved by concentrating the meshes while the computational time will cost much more.

3.2 The Distributions of Effective Stress and Temperature

The properties of workpiece material at elevated temperatures and high strain rates while cutting are very different than that is not under cutting. The curves of stress-strain are predicted according to the JC model, as shown in Fig. 8, at strain rate $\dot{\varepsilon} = 5000\,\text{s}^{-1}$ and temperature $T = 800$ °C. These curves reveal many important properties of the material P20. The material has a significant property of strain hardening in that the flow stress increases as the strain increases slowly. From the left figure, the quite obvious that temperature sensitivity can be found in the material so that the flow stress decreases quickly as the temperature increases, which is called temperature softening effect. Moreover, from the right one, a distinct strain rate sensitivity of the material is shown so that the flow stress increases as the strain rate increases, which can be called the strain rate hardening effect. With the strain rate growing (from 1,000 to 10,000 s^{-1}), the increment of flow stress reduces slowly, causing the strain rate sensitivity of material to decrease, which is because the effect of temperature softening is stronger than strain rate hardening at high speed deformation when the temperature increases, decreasing the level of increment of flow stress.

Figs. 9 and 10 show the predicted distributions of effective stress and temperature with the four different tools during the metal cutting process, respectively. Although the chip is formed with different kinds of tool geometries, the distribution of the stress in the chip is almost the same. It is obvious for the shear zones in these contours that possess the highest stress values that extend from the beginning of the chip bight at the free surface to the edge of the tool or the dead metal zone. Moreover, the highest stress comes from the severe and rapid deformation in the primary zone during the cutting process. From Fig. 9, it can be seen that the distribution of the active stress along the rake face of the tool is highly concentrated in the chip in all cases, and the values are all minuscule. This is due to temperature softening effect which refers to the effective stress decreasing quickly as the temperature increases. The temperature in the friction region is extremely high (Fig. 10) due to the friction between chip and tool, which significantly affects the values of the stress (Fig. 9) in this region. Considering the effect of the temperature on tools, it can been found in Fig. 10 that the highest temperature zones are concentrated in the sliding zone and flank surface, because these two regions experienced the severest friction during cutting. Comparing the temperature distributions of these tools, a fine view can be obtained that the edges of the tools possess extremely high temperatures, suggesting that this region is the first to be worn out. Meanwhile, it can be found that several voids and non-smooth surfaces of the machined material exist in vicinity of the tool edge because of the relatively

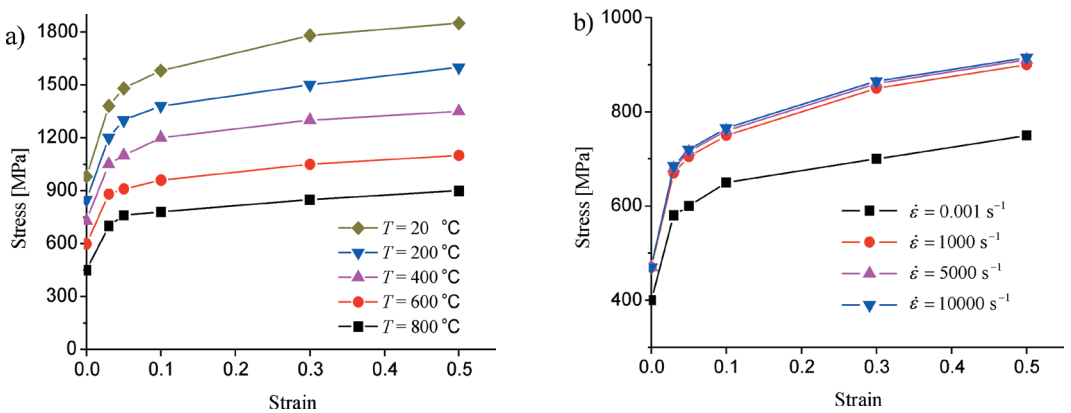

Fig. 8. *Predicting stress-strain curves of JC model; a) at strain rate* $\dot{\varepsilon} = 5000\,\text{s}^{-1}$, *and b) at temperature* $T = 800$ °C

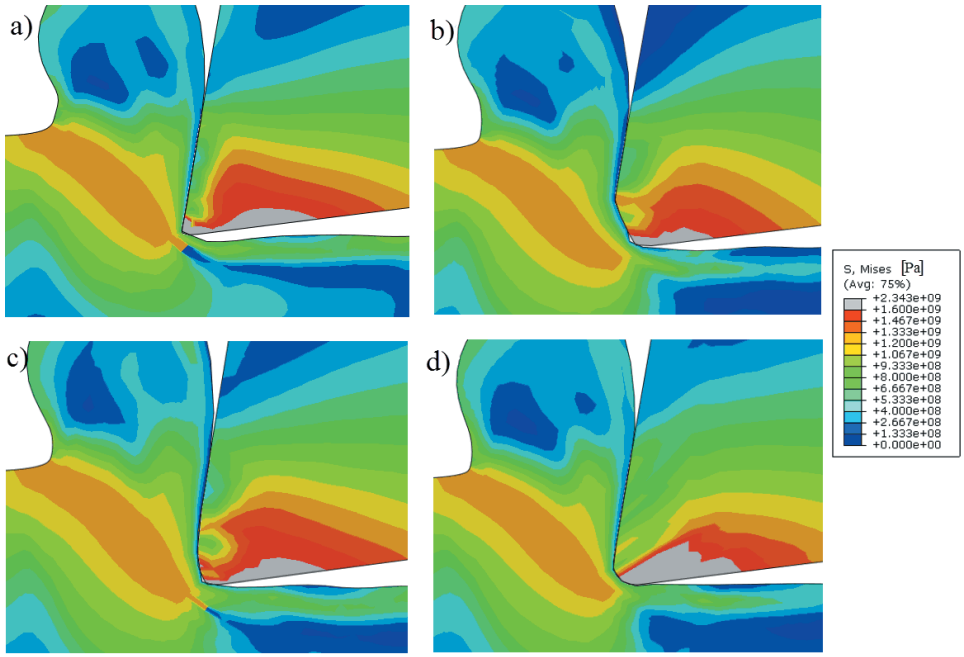

Fig. 9. *Distributions of stress for a) a sharp tool, b) a tool with 25° chamfer angle, c) a double chamfer tool, and d) a blunt tool*

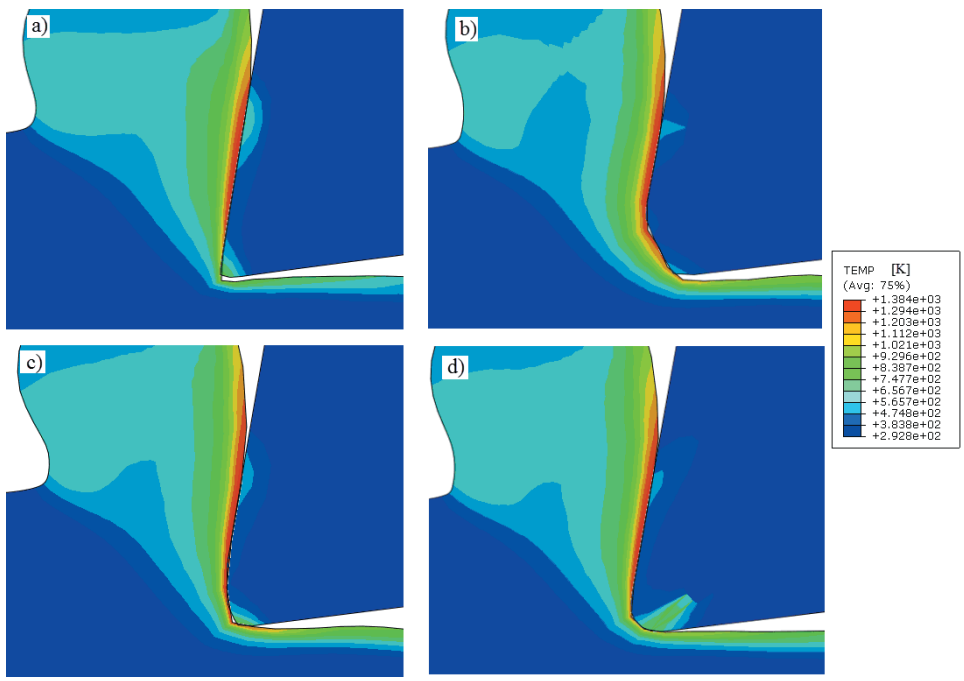

Fig. 10. *Distributions of temperature for a) a sharp tool, b) a tool with -25° chamfer angle, c) a double chamfer tool, and d) a blunt tool*

coarse finite element mesh used in these regions as well as the large deformation of workpiece material during the cutting process. Although finer meshing will result in more accurate simulation results, the computing time will increase significantly due to the re-meshing process. Moreover, after a relatively fine meshing, more grids will not work, but the time still increases. Therefore, a balance between the accurate results and the computing time should be made. In this paper, the balance is made with a relatively fine meshing, considering the computing time. The voids and non-smooth surfaces of the machined material suggest that the results obtained from these simulations will have some differences with the experimental results.

3.3 The Effect of Tool Geometries on the Distribution of Residual Stress

The modelling approach is established on the material stagnation ahead of the cutting edge and the ploughed depth, as shown in Fig. 11. Material flows toward the cutting edge and splits into upward and downward streams at the stagnation in the vicinity of the point P. As for the chamfer and double chamfer tools, the apex of the tool edge (the M of the chamfer tool and the N of the double chamfer tool) is the point P, as shown in Fig. 2. Ploughed depth t is located between the ideal material separation line BD and the actual separation line PC. This part of uncut chip thickness becomes squashed by the cutting edge and contains residual stress. Moreover, the ploughed depth t depends on cutting edge geometry and determines the distribution of residual stress. Therefore, a larger radius contributes to the shifting up of the point P, thus enlarging the ploughed depth t. The residual stresses were obtained in the circumferential direction S11 (parallel to the cutting direction) and in the radial direction S33 (parallel to the feed direction) at the

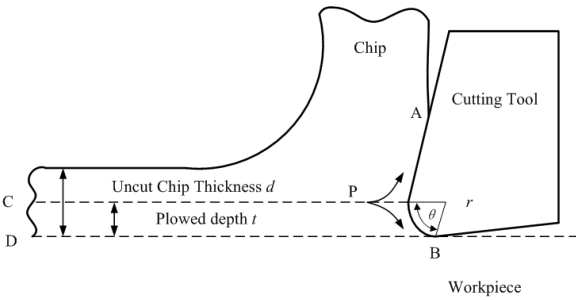

Fig. 11. *Schematic of ploughed depth and material stagnation during the cutting process*

model points, which are at distance 10 times the chip thickness behind the tool, as shown in Fig. 12. The shape of the profiles is almost same with four kinds of different tools in the circumferential (S11) and radial (S33) directions that residual stresses are tensile on the surface then rapidly shift to be compressive and finally stabilize at an approximate non-stress value. Dogra et al. [1] concluded that the effect of the chamfer is equivalent to the increasing hone radius to help increase compressive residual stress but less than

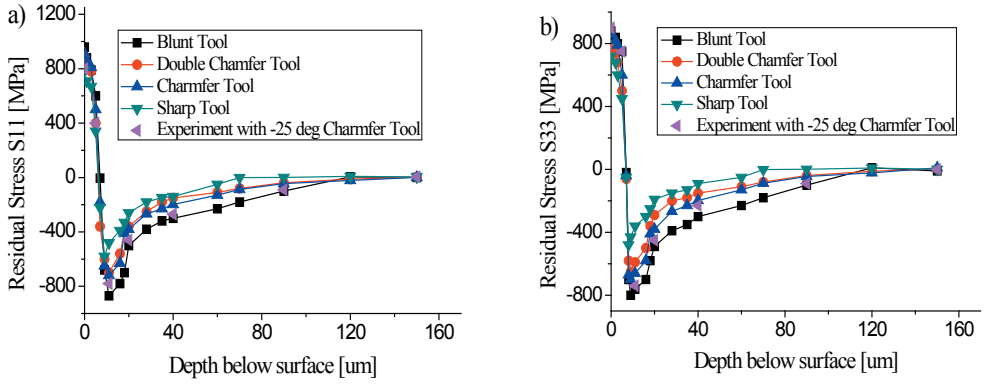

Fig. 12. *The effect of different tools on residual stresses of machined P20 in the a) circumferential (S11) and b) radial (S33) directions with V = 480 m/min and uncut chip thickness 0.1 mm and experimental result with –25 ° chamfer tool*

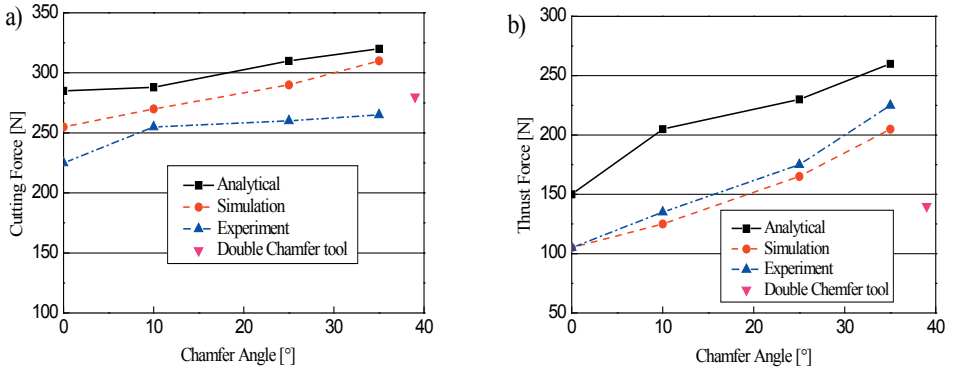

Fig. 13. *Comparison of a) cutting and b) thrust forces between analytical, experimental and simulation results of tools with different chamfer angles, and simulation results of double chamfer tool*

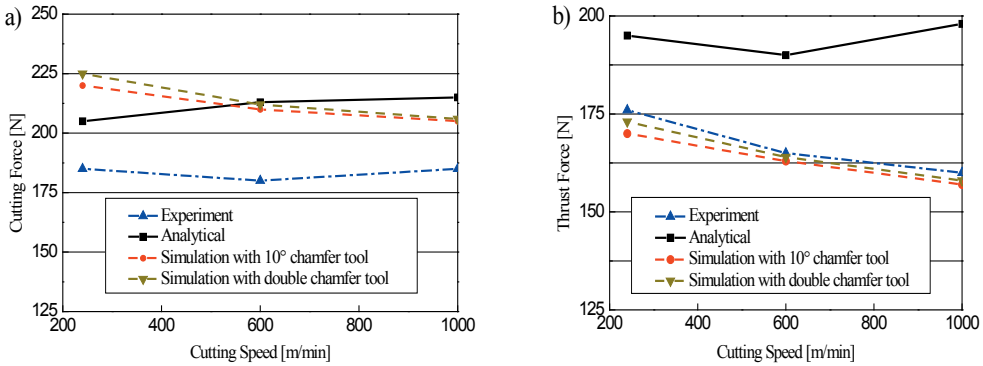

Fig. 14. *Comparison of a) cutting and b) thrust forces between analytical, experimental and simulation results of –10° chamfer tool and simulation with double chamfer tool under different cutting speeds*

that of increasing the hone radius. It can seen in Fig. 12 that the profiles of chamfer and double chamfer tool are almost same, but the peaks of them are both lower than the hone one. The peaks of the residual stresses obtained with the sharp tool are lowest among the other three tools, suggesting that the finer surface quality is acquired. Meanwhile, the experimental results from the operation with a –25° chamfer tool suggest that there is a little diference between measurment and prediction at the surface, which is partially due to the preexisting residual stresses on the actual machined surface that are neglected in the finite element model and the meshing quality in the simulations.

3.4 Effects of the Tool Geometry and Cutting Speed on Machining Forces

Fig. 13 shows the effect of different tool geometries (sharp, chamfer, double chamfer) on cutting forces and the thrust forces obtained by simulations and experiments. It can be seen that the thrust force acquired with the –35° chamfer angle is much larger than other four forces, since the presence of a chamfer angle leads to the buildup of the dead metal zone where the workpiece material will be strained to a larger extent, compared with the sharp tool. Moreover, the force created by the double chamfer tool is between that of the tools with –10° and –25° chamfer angles, because the region of the dead zone created by the double chamfer is moderate. Without considering the beginning of the cutting process when the tool has not been loaded, the cutting force gradually advances and up to a relatively large point, then fluctuates in a small area; the thrust force has the same trend but changes more rapidly. The analytical results obtained from the Ren and Altintas [21] show a great difference between the experimental and simulation results, but give a clear description of the trends of forces which is in qualitative agreement with the others. Nalbant et al. [2] concluded that it is an increment-decrement relationship between cutting speed and min cutting force. Increasing cutting speed by 66.6 % (150 to 250 m/min) and 20 % causes the main cutting force to decrease by 14.6 and 10.4 %, respectively. This trend can be also found in Fig. 14, showing that the machining forces decrease as the cutting speed increases. Moreover, the cutting speed has more significant influence on the thrust force in contrast with the cutting force. Meanwhile, the tool edge geometry has little effect on the machining force as the cutting velocity reaches a comparatively high value.

4 CONCLUSIONS

A finite element model for the simulation of chip formation with different cutting edge geometries during the cutting process has been presented. The simulation results show that the edge geometries affect the chip removal process less significantly, because the dead zones are formed under the chamfer, double chamfer and blunt edge to act as the main cutting edge of the tools, just like the sharp tool. The coupled thermal-mechanical analysis was conducted with four different tools, and some results were obtained. The behaviour and shape of the dead metal zone are studied by examining the distributions of the material velocity and the stress. The effect of tool edge geometry on the residual distribution was also studied, showing that the chamfer and double chamfer tool had the almost same function on the residual stress distribution in comparison with the hone tool and sharp tool. It is clear that the force in

the thrust direction has more dependence on the tool geometry and cutting speed, in comparison with the one in the cutting direction. The forces increase as the chamfer angle increases, and decrease as the cutting speed increases. The cutting edge geometry has little influence on the machining force when the cutting speed reaches a very high level.

Finally, the present fulfillment of the ALE method is only applied to continuous chip formation, and can not directly extend to segmented chips, which need a better crack propagation scheme. A more complex mesh motion scheme should be used to allowed for the formation of new surfaces in chips.

5 ACKNOWLEDGEMENTS

The authors would like to thank Shanghai University of Engineering Science (Project Code: 14KY0107) for providing financial support for the project, and the reviewers for their suggestions.

6 REFERENCES

[1] Dogra, M., Sharma, V.S., Dureja, J. (2011). Effect of tool geometry variation on finish turning–A Review. *Journal of Engineering Science and Technology Review*, vol. 4, no. 1, p. 1-13.

[2] Nalbant, M., Altın, A., Gökkaya, H.. (2007). The effect of cutting speed and cutting tool geometry on machinability properties of nickel-base Inconel 718 super alloys. *Materials & Design*, vol. 28, no. 4, p. 1334-1338, **DOI:10.1016/j.matdes.2005.12.008**.

[3] El-Wardany, T.I., Kishawy, H.A., Elbestawi, M. A.. (2000). Surface integrity of die material in high speed hard machining, Part 1: Micrographical analysis. *Journal of Manufacturing Science and Engineering*, vol. 122, no. 4, p. 620-631, **DOI:10.1115/1.1286367**.

[4] Shintani, K., Ueki, M., Fujimura, Y. (1989). Optimum cutting tool geometry when interrupted cutting carburized steel by CBN tool. *International Journal of Machine Tools and Manufacture*, vol. 29, no. 3, p. 415-423, **DOI:10.1016/0890-6955(89)90010-2**.

[5] Shintani, K., Ueki, M., Fujimura, Y. (1989). Optimum tool geometry of CBN tool for continuous turning of carburized steel. *International Journal of Machine Tools and Manufacture*, vol. 29, no. 3, p. 403-413, **DOI:10.1016/0890-6955(89)90009-6**.

[6] Matsumoto, Y., Hashimoto, F., Lahoti, G. (1999). Surface integrity generated by precision hard turning. *CIRP Annals - Manufacturing Technology*, vol. 48, no. 1, p. 59-62, **DOI:10.1016/S0007-8506(07)63131-X**.

[7] Kountanya, R., Al-Zkeri, I., Altan, T. (2009). Effect of tool edge geometry and cutting conditions on experimental and simulated chip morphology in orthogonal hard turning of 100Cr6 steel. *Journal of Materials Processing Technology*, vol. 209, no. 11, p. 5068-5076, **DOI:10.1016/j.jmatprotec.2009.02.011**.

[8] Shatla, M., Yen, Y.C., Altan, T. (2000). Tool-workpiece interface in orthogonal cutting-application of FEM modeling. *Transactions of the North American Manufacturing Research Institution of SME*, p. 173-178.

[9] Kim, K.W., Sins, H.-C. (1996). Development of a thermo-viscoplastic cutting model using finite element method. *International Journal of Machine Tools and Manufacture*, vol. 36, no. 3, p. 379-397, **DOI:10.1016/0890-6955(95)00054-2**.

[10] Shi, G., Deng, X., Shet, C. (2002). A finite element study of the effect of friction in orthogonal metal cutting. *Finite Elements in Analysis and Design*, vol. 38, no. 9, p. 863-883, DOI:10.1016/S0168-874X(01)00110-X.

[11] Movahhedy, M. R. (2000). *ALE Simulation of Chip Formation in Orthogonal Metal Cutting Process*, PhD thesis, University of British Columbia, Vancouver, p. 33-38.

[12] Waldorf, D.J., DeVor, R.E., Kapoor, S. G. (1999). An evaluation of ploughing models for orthogonal machining. *Journal of Manufacturing Science and Engineering*, vol. 121, no. 4, p. 550-558, DOI:10.1115/1.2833050.

[13] Al-Athel, K.S., Gadala, M.S. (2011). The use of volume of solid (VOS) approach in simulating metal cutting with chamfered and blunt tools. *International Journal of Mechanical Sciences*, vol. 53, no. 1, p. 23-30, **DOI:10.1016/j.ijmecsci.2010.10.003**.

[14] Jacobson, S., Wallén, P. (1988). A new classification system for dead zones in metal cutting. *International Journal of Machine Tools and Manufacture*, vol. 28, no. 4, p. 529-538, **DOI:10.1016/0890-6955(88)90065-X**.

[15] Liu, K., Melkote, S.N. (2007). Finite element analysis of the influence of tool edge radius on size effect in orthogonal micro-cutting process. *International Journal of Mechanical Sciences*, vol. 49, no. 5, p. 650-660, **DOI:10.1016/j.ijmecsci.2006.09.012**.

[16] Movahhedy, M.R., Altintas, Y., Gadala, M.S., (2002). Numerical analysis of metal cutting with chamfered and blunt tools. *Journal of Manufacturing Science and Engineering*, vol. 124, no. 2, p. 178-188, **DOI:10.1115/1.1445147**.

[17] Mu-oz-Sánchez, A., Canteli, J.A., Cantero, J.L., Miguélez, M.H.. (2011). Numerical analysis of the tool wear effect in the machining induced residual stresses. *Simulation Modelling Practice and Theory*, vol. 19, no. 2, p. 872-886, **DOI:10.1016/j.simpat.2010.11.011**.

[18] Johnson, G.R., Cook, W.H. (1983). *A Constitutive Model and Data for Metals Subjected to Large Strains, High Strain Rates and High Temperatures*, p. 541-547.

[19] Alvarez, R., Domingo, R., Sebastian, M.A. (2011). The formation of saw toothed chip in a titanium alloy: influence of constitutive models. *Strojniški vestnik - Journal of Mechanical Engineering*, vol. 57, no. 10, p. 739-749, **DOI:10.5545/sv-jme.2011.106**.

[20] Liu, M., Takagi, J.-i., Tsukuda, A. (2004). Effect of tool nose radius and tool wear on residual stress distribution in hard turning of bearing steel. *Journal of Materials Processing Technology*, vol. 150, no. 3, p. 234-241, **DOI:10.1016/j.jmatprotec.2004.02.038**.

[21] Ren, H., Altintas, Y., (2000). Mechanics of machining with chamfered tools. Journal of Manufacturing Science & Engineering, vol. 122, no. 4, p. 650, **DOI:10.1115/1.1286368**.

Strojniški vestnik - Journal of Mechanical Engineering 61(2015)3, 167-175
DOI:10.5545/sv-jme.2014.2294
Original Scientific Paper
Received for review: 2014-11-11
Received revised form: 2015-01-16
Accepted for publication: 2015-01-29

Deterministic Mathematical Modelling of Platform Performance Degradation in Cyclic Operation Regimes

Nenad Kapor[1] – Momcilo Milinovic[1]– Olivera Jeremic[1] – Dalibor Petrovic[2]
[1]University of Belgrade, Faculty of Mechanical Engineering, Serbia
[2]University of Defense, Military Academy, Serbia

This paper considers the modelling of extreme-capability working platforms that are operated in periodic cycles, each cycle having a predefined number of operations that affect the working surfaces. A novel hypothesis is introduced about the platform-degrading effects that cause an equivalent decrease in the successful operations after repeated cycles. Deterministic modelling, based on the basic equations of Lanchester and Dinner, is generalized here to include coupling between parameters. The newly developed mathematical model of performance degradation is in good agreement with both experimental measurements and numerical simulations. It is assumed that the new variables and their correlations link the Gaussian distribution and the observed performances of the testing platforms. Relative probability dispersions of affected surfaces are derived, as a new indirect referencing figure of merit, to describe simulations and compare them to experimental test data. The model proves a hypothesis that the degrading effects are a function of the platform capacity, frequency of operations and the number of available cycles. Degradation effects are taken into account through an equivalent decrease of effective operation capacities, reflected on the properties of the affected operating surfaces. The obtained estimations of degradation could be used in the planning of platform capacity as well as in the selection of real affected surfaces in various machining systems and for a wide range of different materials.
Keywords: cycles, operations, extreme machine platforms, probabilities, deterministic modelling

Highlights
- *Modelling of extreme-capability working platforms that are operated in periodic cycles.*
- *Proposed methodology for performances degradation caused by operations composed in cycles.*
- *Using Gaussian probability distribution law to predict degradation measures.*
- *Predicting the changes of probability dispersion based on modelling and experimental data.*
- *Determination of an analytical model based on a hypothesis that the degrading effects are a function of the platform capacity, frequency of operations and the number of available cycles.*

0 INTRODUCTION

Machines operating in cycles and their properties have not been studied in depth in literature and, as such, are not well described by integral mathematical models. If the effects of their operation are actions on the given working surfaces under given constraints, then the quality of the affected surfaces can be described by reliability functions. In this manner, the operating capabilities of the platform can be determined. A majority of the published papers use a standard approach to the measured performances that depend on the machine's designed purposes. Such processes are described in **[1]** to **[3]** for the abrasive flow machines (AFM) with which material is hardened by randomly treating the working surface with abrasive particles with polymeric fillers, and dispersed within the flow media. The authors of **[1]** classified the work piece parameters into three groups based, among others, on the number of cycles (operations) and the machining time. Some of these parameters were determined experimentally in **[2]**, in which the authors recognized that the parameters denoted as the creeping time and the cycles frequency have impact on the quality of the machining process. In **[3]**, the authors experimentally prove that the aforementioned parameters influence the process. Common for all three papers is that they do not include hidden random effects caused by particles affecting the surfaces in cyclic operations, although such effects significantly influence the quality of the surface treatment. In all three papers, there is no mathematical modelling of the process.

Another similar type of machine with cyclic operation affecting working surfaces is described in **[4]** as shot-peening (SP) platforms. They bombard a surface with spherical beads to increase the material fatigue strength. The physical modelling of the influence of the bead shapes on the performance of the surface hardening process is presented in **[5]**. Random surface effects due to bombing cycles are a result of the quality of the machine's performance. However, the connection between the effects and the particular operations is missing in **[5]**. Paper **[6]** utilizes a risk function to consider the example of solar rays hitting a surface as a random process. In fact, the determination of the risk function dumping requires much more precise estimations of the distribution if probabilities

*Corr. Author's Address: University of Belgrade, Faculty of Mechanical Engineering, Kraljice Marije 16, 11000 Belgrade, Serbia, mmilinovic@mas.bg.ac.rs

of the effect occurrence on the attacked surface. However, this paper lacks a mathematical model of random disturbances of these probabilities. Common for the description of the processes in both AFM and SP machines, as well as the processes described in [6], is that they lack the deterministic or probabilistic mathematical modelling of cycles and their parameters on the efficiency of the final process.

Mechanical engineering of extreme machines in defence technologies have particular operations grouped in the cycle regimes. These operations affect the working surfaces or areas, with constrained machine capacities with regard to operation numbers. The modelling of efficiencies in such cases is usually done using the deterministic differential theories of operational research. This approach is based on the so-called Lanchester and/or Dinner equations of particular probabilities and their distribution laws, as presented in detail in [7], as well as in [8]. Their equations use variable attrition rates as the frequencies in operations probabilities, similar to [9], in which surface point effects are taken with variable probabilities. The modelling of cycles' efficiencies in these references is performed with coupled equations, in which two subjects simultaneously affect each other. Their actions are interdependent but different; their efficiencies also evolve differently over time. This approach is not entirely useful to define a stand-alone efficiency estimation for a single subject.

A mathematical model of the equipment with constrained capacities that generates identical repeated operations in a given order is presented in [10] for air platform equipment. The main contribution of this paper is the treatment of the action on the working surfaces as a random process, but the probability distribution laws on the affected surfaces are missing. The two-dimensional Gaussian distribution laws, used for welding processes, as referred in [11], could be useful in the estimation of random processes on surfaces.

According to the state-of-the-art analysis as presented in the cited papers, there is no comprehensive mathematical model, proven by experimental data, that would be capable of explaining relations between the machine's cyclic performances, its capacities and the quality of randomly affected surfaces, as well as the designed processing time. This is because the papers do not consider two repeating processes simultaneously acting on a single object (one as working and the second as redundant or parasitic), which together change the quality of the expected performances.

The objective of this paper was to develop a general joint mathematical model that includes all pertinent factor that influence the final efficiency of processing, thus enabling the simulation and evaluation of these parallel processes.

Based on the specific requirements for sequential processing of the surfaces, a mathematical model is developed using a deterministic approach treating the surface processes as random variables.

The objective was to test the efficiency of cyclic operations affecting the working surfaces, essentially by considering differences caused by the capacities and operation rates of the processing machine. This was shown using the experimental data on operation platforms with extreme performances.

The novelty of the approach presented in this manuscript is the redesign of coupled deterministic equations done in a new manner. In the literature above, these equations are employed to describe the mutual effects of objects as a function of the elapsed process time. This approach in the literature makes the time functions dependent on the performances of two objects. In our approach, one object executes two operations in parallel, one of them comprising the working process itself, and the other, parasitic, occurring as self-degradation dependent on the first one. Both happen on the same object, i.e. the operation platform performing the same action. The new approach composes deterministic equations to describe this and to measure changes in the platform efficiency. With our approach, the quality of the working process is the convolution of both kinds of operations in one cycle, as well as their frequencies. The number of cycles influences the random arguments and reflects the probabilities of working surface coverage that follow the two-dimensional Gaussian distribution laws. This was taken as the measure of the changes in quality due to self-degradation.

1 EXPLANATION OF THE GENERAL MODEL

The model offers the possibility of evaluating the degradation of the platform performance, with regards to the equipment and devices contained within the platform. The quality of the affected surface is regarded as the dimension of probability dispersion. This dimension appears during the execution as the consequence of cycle duration and the operations frequency, as well as of the capacities of the platform. The approach presented in [12], which developed operations frequency coupled with execution probabilities as the combined attrition parameter, was used in developing our general model. Changes

of probability dispersions of random values on the affected surface appear in the form of the Gaussian distribution law. The degradation of the platform properties through the operation cycles is represented by changes in the Gaussian distribution. This is valid under the assumption that one particular Gaussian distribution function is valid for each cycle in the working regime.

In our approach, this function is distributed in successive cycles in the form of extended probability dispersions of both random arguments in the two surface directions. Consequently, the changing of efficiencies over time is measured by the resulting effects on the new randomly affected surfaces. The decrease in the efficiency with each new cycle in reflected in the new less-affected surfaces. This also results in the degradation of the working platforms' capabilities caused by less effective particular operations in the cycles. The cause of this degradation could be a consequence of rapid high-energy operations realized in short-time sequences (high mechanical power values) in successive, orderly repeated cycles, similar to those described in paper [13]. However, according to that paper, the affected points on the surfaces do not obey any probabilistic law, and thus there is no error distribution as a modelling parameter. In our research, we use the changes of the probability dispersion (PD) after each cycle, due to all the errors in the cycle, as a measure of the platform efficiency. These changes are caused by the generator of the cycles and by its self-degradation, and are reflected in the decreased number of declared operations. This makes the designed operational capacities of the platforms less effective with the number of cycles.

In order to estimate the degraded platform performances by means of time-based simulation, new relative parameters have been accepted in the modelling.

The deterministic modelling of the estimations of the so-called vulnerability performances is presented in [14] and [15]. The performances considered there are similar to our degrading platforms' performances. The models presented in [16], called Pexpot, Levpot and Dynpot, were also developed as vulnerability considerations based on the attrition rate function and thus indirectly describe the kind of expected degradation capabilities. An essential difference of our model is that the degradation of the system appears as a direct consequence of self-degradation caused by the effects of the repeated cycles. The designed frequencies and functional probabilities, contained in each operation, are reflected in the full platform capacity on the affected surfaces. This effect makes the proposed model more useful in planning the redesigning of platform capacities for required affected surfaces.

2 MATHEMATICAL MODELS

In the presented model, the platform has the capacity of M_{p_0} particular operations oriented toward the working surface. These operations occur in dynamic regimes with successive frequencies λ and a probability of surface action of approximately $p = 0.997$. This is provided using the maximum technical dimensions of the surface, which correspond to the 64 $PD_{av}2$. The width and depth of the surface used eight of the same average probability dispersions PDav, in both surface directions. Average probability dispersions PD_{av} are taken as an equal of the expected Gaussian distribution of two-dimensional random arguments. The probability variations are represented as functions of the cycle number and of the full capacity of operations. The designed properties of these processes are consequently the function of probability changes. The adopted hypothesis is that the degradation of the platform performances is an imaginary effect, able to be explained by the values of the effective and ineffective numbers of operations. This ensures a possibility of considering the ineffective number to be a value increasing with the number of cycles during the exploitation time. In that sense, the increasing number of ineffective operations corresponds to the increase of cycle probabilities dispersions.

Operative consumption is realized in cycles with the same sequential probabilities of operations, p, as in [10]. In that case, the frequency of executions of real operations, as the real rate of operation, is:

$$\frac{dM_p}{dt} = -\lambda p = -\alpha_p. \tag{1}$$

This determines the remaining number of operations as the $M_p = M_p(t)$ in each moment of time t in the cycle duration interval.

It is expected that the probability would not have a fixed value but would vary over exploitation time. The changes of probability function p could mean random changeable performances that disturb the rate of real operations on the working surfaces. The changes in probabilities affect the rate of real operations $\dot{M}_p$ in Eq. (1). This is not really possible because the frequency of operation executions is a designed property of the platform hardware. The present hypothesis has only an imaginary effect.

The acceptable solution could be to recalculate the influence of the number of ineffective operations on the new probable dispersion PD reflected in a new Gaussian distribution but for the unchanged execution operations probabilities. The consequence is that the model has to consider the extended working surfaces, with new dimensions 64 PD² engaged in operations after each cycle.

The platform degradation, as an imaginary effect, is a process in the real cycle time and is simultaneously parasitic in real operations. A new value of the modified equivalent number of operations $m_p(t)$ is diminished by this imaginary effect. This is generated as a current and recalculated capability of working platform. The new value is lower than the real number of the remaining operations $M_p(t)$. At the very beginning, it is equal to the real available capacity $m_{p_0} = M_{p_0}$.

The reason is underpinned by the fact that the model of self-degradation is viewed as a new, fictive rate of equivalent non-effective operations changes $\dot{m}_p$, which is not equal to the rate of real operation $\dot{M}_p$. This orients the mathematical model to consider the share of degraded value on each of the real operations and, by that effect, redesign the remaining number of operations available on the platform. Such a transformation implies that the degrading rate of $\dot{m}_p$ and the real rate $\dot{M}_p$ during each cycle are proportional to the remaining equivalent dimensionless number of operations $1/m_p$. The correction coefficient is the portion of one operation within the actual remaining equivalent number m_p.

Based on the previous concept, the differential equation for the degradation rates, Eq. (1), becomes:

$$\frac{dm_p}{dt} = -\alpha_p \frac{1}{m_p}. \tag{2}$$

Since the model of equivalent numbers is a function of time and the current equivalent number m_p, as the instantaneous remaining capacity, the platform performances are degraded continually with each cycle. This always means a new valid number of operations with regard to the remaining capacity. It is inappropriate to use the approach as constant and fixed for any platform capacity since it is dependent on the available number of operations. The relative degradation of the platform capacity is taken as more acceptable in modelling with the functional ratio $\mu_p(t) = m_p(t) / m_{p_0}$ where $\mu_p(t=0) = 1$, as the *current relative capacity degradation* of the platform. The general differential equation (Eq. (2)) of new functional μ_p, by methodology given in [7], is:

$$\frac{d\mu_p}{dt} = -\alpha_p \frac{1}{\mu_p M_{p_0}^2}. \tag{3}$$

If the platform, under the same conditions, executes repeating working cycles n times, in equal time intervals for each cycle of Δt, and the rate of operations in the cycle is the same, then using Eq. (3), any of i cycles (where $i = 1, 2, ..., n$) is used at the beginning of a new, redesigned equivalent number of operations from the previous cycle. The *current relative degrading* in cycle is defined as a new differential equation:

$$\frac{d\mu_{p_i}}{dt} = -\alpha_p \frac{1}{\mu_{p_i} m_{p_{(i-1)}}^2}, \quad i = 1, 2, 3. \tag{4}$$

The solution of Eq. (4) is:

$$\mu_{p_i}(t) = \sqrt{1 - \frac{2\alpha_p}{m_{p_{(i-1)}}^2} t}. \tag{5}$$

The function of the *current relative capacity degradation* of the platform full capacity after (i–1), and during the i^{th} cycle at an instant $(i-1)\Delta t < t < i\Delta t$, similarly to **[10]**, is:

$$\mu_p(t) = \mu_{p_i}(t) \prod_{j=1}^{i-1} \mu_{p_{(j)}}, \tag{6}$$

with the condition $\prod_{j=1}^{i-1} \mu_{p_{(j)}}$ for the $i = 1$. The estimation of the *relative efficiency of the current process* is the function of the affected and the initial working surface. This functional is determined for the unaffected, remaining surface at each cycle and the final working surface from the previous cycle, taken as initial in the current one. It is given in the form:

$$\mu_{p_i}(t) = 1 - \frac{S_i(t)}{S_{(i-1)}^c}, \tag{7}$$

The differential equation of the *relative efficiency of the current process,* as the remained relative surface within operation cycle considered as the degraded ones, according to a similar differential equation in **[7]** and **[10]**, is:

$$\frac{d\mu_{c_i}}{dt} = -U_i \mu_{p_i} \mu_{c_i}, \quad 0 < t < \Delta t. \tag{8}$$

If the platform operates in cycles without degradation effect, its $\mu_{p_i} = 1$, the functional μ_{p_i}

does not affect Eq. (8) and the coupling of Eqs. (4) and (8) is lost. Consequently, the *relative efficiency of the current process*, denoted by $\mu^*_{c_i}$, during the un-degrading surface processing in the cycles is described by:

$$\frac{d\mu^*_{c_i}}{dt} = -U_i \mu^*_{c_i}. \tag{9}$$

In both Eqs. (8) and (9), the operation number in one cycle is the *designed capability,* and could be variable. This depends on the designed cartridge capacity used for continual operations in the short impulse regimes. The well-balanced example between the number of operations and the covered affected surface in one cycle is the referent platform given in [10]. It uses cartridges of maximum $N_p(\Delta t)=8$, and its cycle expires in 4.4 seconds. The accepted functional *designed capability* of the platform, redesigned for the considered example, is:

$$U_i = \lambda p \frac{1.82\sigma}{S_o}. \tag{10}$$

Appropriate values need to be calculated for each platform cartridge with their declared performances regarding the expected affected surface. The solution of Eq. (8) is:

$$\mu_{c_i}(t) = \mu_{c_i}(0) e^{\frac{U_i m^2_{p(i-1)}}{3\alpha_p}\left(\mu^3_{p_i}-1\right)}, \tag{11}$$

while for the ideal, un-degraded effect, from Eq (9), it takes the form:

$$\mu^*_{c_i}(t) = \mu^*_{c_i}(0) e^{-U_i t}. \tag{12}$$

The next appropriate assumptions for the initial conditions are used:

- Model A with initial conditions for the *relative efficiency of the current process* at the very beginning $\mu_{c_i}(0) = 1 - \frac{S_i(0)}{S^c_{(i-1)}} = 1.$
- Model B with variable *relative efficiency of the current process* at the very beginning $\mu_{c_i}(t=0) = \mu_{c_i(i-1)} < 1$ taken in the next cycle from the end of the previous one. In both cases, the designed cycle capability of the platform $U_{i\max} = \lambda p \frac{1.82\sigma}{S_o} = const$ and is constant in all cycles as a declared value.

The cumulative relative efficiency of all finished processes is:

$$\mu_c = \prod_{i=1}^{n} \mu_{c_{(i)}}. \tag{13}$$

For the experimental verification of the correlation between the platform capacities and the affected surfaces for the degraded as well as for the un-degraded (available) number of operations, new expressions were required. If all available cycles on the platform are expired, the full affected surface S_p and the working surface S_0 can be correlated. The correlation could be expressed via a relation analogous to Eq. (7), using degradation effects on the surface given by *cumulative relative efficiency of all finished processes* in Eq. (13). This yields the relation

$$S_0 = \frac{S_p}{1-\mu_c}. \tag{14}$$

The same logic, analogous to Eq. (14), could be used for the non-degraded working surface S^*_0 and the affected surface S^*_p equations. They also have to be related to the *cumulative relative efficiency of all finished processes* without degradation of μ^*_c, which is a product similar to Eq. (13), with $\mu^*_{c(i)}$ determined from Eq. (12), in the same form as Eq. (14). For the ideal designed number of operations, as well as for the degraded number, the particular affected surfaces are equal ($S^*_p = S_p$). This is because no operation in the cycle is missed but is only exposed somewhere on the larger area. The working surfaces S_0 and S^*_0 could be determined as the squares of the appropriate Gaussian linear values of average probability dispersion PD_{av} for both cases. Since the degraded and the non-degraded *cumulative relative efficiency of all finished processes* are the functionally correlated to the surfaces given by Eq. (14), the dispersion values also satisfy these correlations in both cases.

Since the surfaces are taken as $8PD_{av} \times 8PD_{av}$, using basic Eq. (14) and their analogues, the ratio of PD* in un-degraded and PD of degraded cases is expressed by:

$$\frac{PD^*}{PD} = \sqrt{\frac{1-\mu_c}{1-\mu^*_c}}. \tag{15}$$

This new approach provides the method for a comparison of degraded and un-degraded surfaces of accepted dimensions, or for treating expected degrading by constraining the allowable ratio.

3 SIMULATION DATA AND RESULTS

Simulation tests are realized using MATLAB software package and compared with experimental research. The basic assumptions in the simulations were:

- Platform capacities and cycles performances presented in Table 1 are used for simulation testing, as well as in experimental modelling. These data are used in the platform degradation modelling;
- Numerical test is provided for the 8, 16, 24, 32, and 40 operation capacity of the platform. As it was accepted in the mathematical model, one cycle had 8 operations and expired in a nominal time of 4.4 seconds.

Fig. 1 represents the simulation results of the *current relative degradation* of successive ordering operations in the sequential cycles. The degraded values are positive and decreasing, bounded with value 1 from the upper side. The simulation shows that at the end of each cycle, the *current relative degradation* final value is decreasing, regardless of the number of operations remaining constant.

The consequence of the model is that platform capability degrades more rapidly in each subsequent cycle, regardless of the same number of operations. It is the consequence of the decreasing number of equivalent operations after each real execution rate. The rapidest decrease of the *current relative capacity degrading* has been observed for the platform with 8 designed operations within one cycle.

Lower degradation occurs on platforms that have 16, 24, 32 and 40 operations as the full capacity.

Platforms with higher initial capacities, e.g. the number of operations, have smaller gradients and lower degradation at the end of the cycle.

Fig. 2 represents the equivalent number of degraded operations starting with a different real number of platform capacities. It is visible that the gradient disperses with time. This process shows the minimum gradient for the platforms tested with 40 or more real operations compared to platforms with fewer capacities used in the simulation model.

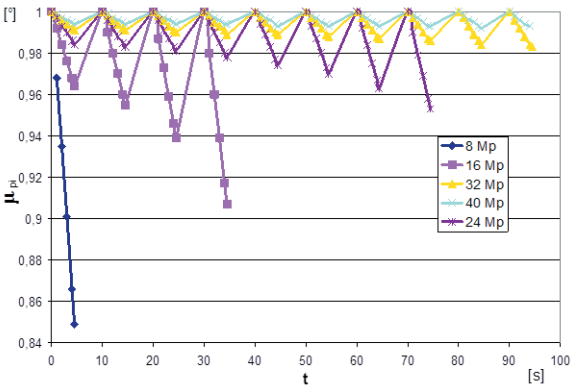

Fig. 1. *Functions of current relative degradation of successive ordering operations in the sequential cycles*

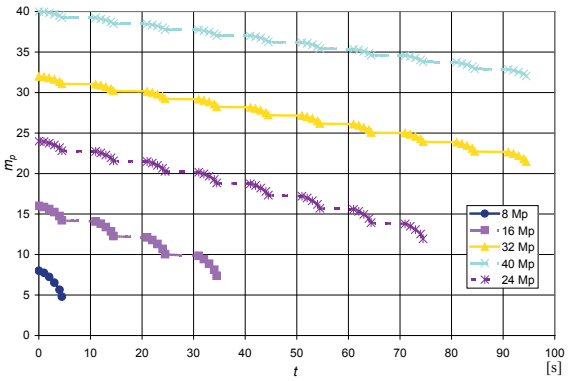

Fig. 2. *Real initial and degraded equivalent number of operations on the platforms with different operation capacities*

Fig. 3 explains the model of *cumulative relative efficiency of all finished processes*. As it shown in Figs. 3a and b, the unaffected surface decreases with the increasing number of operations. This decrease is more or less similar to the experimental results of surface roughness decrease, presented experimentally in [1]. This paper has shown similar surface effects as our model.

Table 1. *Simulated platforms performances*

Capacity variant	Number of operations in one tool set	The number of tool-sets	Available number of platforms operations	Rate of operation λ [1/s]	Working surface [m²]	Effective tool radii Rc [m]	Elementary surface efficiency σ [m²]	Number of designed affected operations in one cycle
1	4	2	8	1.8	1.7	0.126	0.05	8
2	4	4	16	1.8	1.7	0.126	0.05	8
3	4	6	24	1.8	1.7	0.126	0.05	8
4	4	8	32	1.8	1.7	0.126	0.05	8
5	5	8	40	1.8	1.7	0.126	0.05	8

Paper [1] also reported significant changes in the first 20 operations (so-called cycles in [1] and [2]) and the gradual reaching of a saturated level. The result shown in Fig. 1 also shows the saturation performance of relative degrading, but with at least 40 operations. It could be seen that those values are of the same order of magnitude.

Experiments in [1], developed for surface roughness, have shown that the roughness decreased slightly after 50 operating cycles. Comparative considerations about similarities of surfaces affecting processes, shown in Fig. 3, regardless of whether they have been tested on the different machines with different purposes, showed the same sort of behaviour.

Two models of surfaces with different initial conditions marked as a) and b) shown in Fig. 3 are tested in simulation. The first tested case, for the both models, is degraded platform performance and the

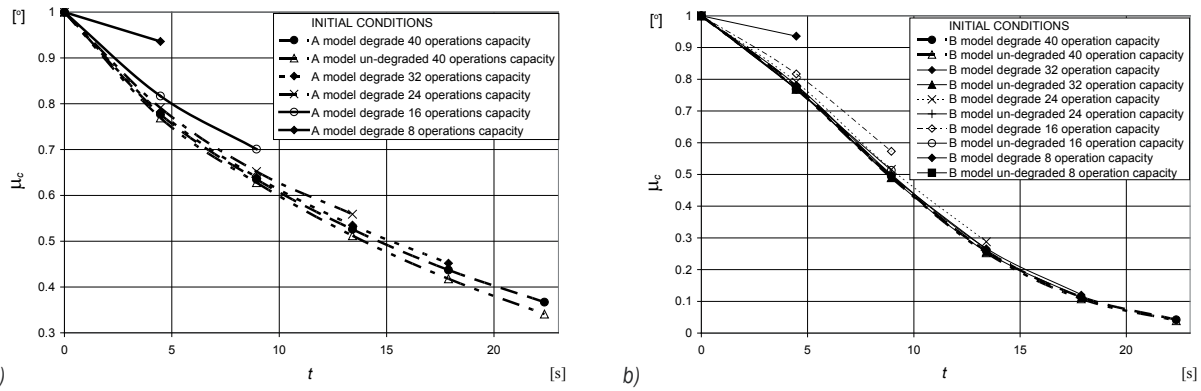

Fig. 3. *Current relative efficiency of affected surface with variable operation designed capacities and number of cycles; a) model A, and b) model B*

Table 2a. *Experimental data for the probability dispersions*

Cycle No	Model B: Experimental test of PD_{av} data [m]	Model B: Dispersion error [%]	Model A: Experimental of PD_{av} data [m]	Model A: Dispersion error [%]
1	7.5	36	5.0	32
2	5.0	10	5.0	32
3	5.0	10	9.0	22
4	5.0	10	9.0	22
5	5.0	10	9.0	22
6	5.5	0	7.5	1
PD_{av}	5.5	12.67	7.4	21.8

Table 2b. *Simulation of the probability dispersions*

Total cycles time t [s]	Degraded μ_c [°]	Non-degraded μ_c^* [°]	$1-\mu_c$ [°]	$1-\mu_c^*$ [°]	PD_{av}^* / PD_{av}	% of surface extension	Operation capacity
$\mu_c \neq 1$				Model B			
4.47	0.936	0.769	0.064	0.231	0.526361	47.36	8
8.94	0.468141	0.394497	0.531859	0.605503	0.937217	8.675	16
13.41	0.117549	0.100695936	0.882451	0.899304	0.990586	2.84	24
17.88	0.012616	0.010803896	0.987384	0.989196	0.999084	1.217	32
22.35	0.000476	0.000401542	0.999524	0.999598	0.999963	0.608	40
$\mu_c = 1$				Model A			
4.47	0.936	0.769	0.064	0.231	0.526361	47.36	8
8.94	0.572717	0.482932	0.427283	0.517068	0.909042	10.67	16
13.41	0.288294	0.247261184	0.711706	0.752739	0.972362	4.36	24
17.88	0.120871	0.103355175	0.879129	0.896645	0.990184	2.4	32
22.35	0.041622	0.035244115	0.958378	0.964756	0.996689	1.556	40

second one is the non-degraded performance. Both curves of the cases, for both models, are shown in Figs. 3a and b. The platforms with lower operation capacities, 8 and 16, in simulations have greater differences for degraded and un-degraded tests for Model A. This is also valid in Model B. At higher operation capacities, 24, 32 and 40 have diminishing differences except in Model B where their differences disappear more rapidly than in Model A. The curves from Fig. 3 present the *relative efficiency of the current process*, with regard to cycle time as a continuously varying value.

Differences between the relative values of affected surfaces in the degraded and un-degraded cases have been recalculated on their new extended working surface dimensions and transformed into their probability dispersions ratios. The average probability dispersion, PD_{av}, as the measure of degraded surface is shown in experimental and simulation test data in Tables 2a and b from Eq. (15) for the platforms with different capacities and cycle numbers composed in the tool sets (Table 1). Repeated experimental tests have been realized in cycles with 8 operations in 6 realized experiments shown in Table 2a. It is obvious that both experimental models, A and B, show strong degradation of the initial probability dispersions. The decrease is slowed down by the increasing number of operations in the new cycles. Saturation is achieved after 24 operations for Model A and after 16 operations for Model B.

It is obvious that Model B, where the *relative efficiency of the current process* at the very beginning of cycles is taken from the previous cycle, has a smaller saturation decrease of PD_{av} in both experimental and simulation cases.

In Table 2b, the dispersion in Model B is saturated after 24 operations from 47 to 2.84% and further approaches 1%. In both models, after at least 40 operations, (in experiments after 48), the probability dispersion PD stopped decreasing and diminished.

The percentage of the errors measured by the surface extension over PD, for the model in simulations and in experiments, is about 4% for Model B and about 29% for Model A.

This is because the decreased unaffected surface from the previous cycle in Model B is repeatedly taken as an initial surface for each next cycle. Consequently, errors increase as the cumulative values from the previous cycles. Taking into account the unsteady-state random processes on the designed platforms, predictions of efficiency made by this indirect modelling are of sufficiently quality.

4 CONCLUSIONS

In the present state of the art, in the field of surface-affecting machines, there is no unified model theory that connects the variable machine performances with effects on the affected surface determined in continuous working process. Operational research modelling offers some models of interaction of two interdependent objects. In our model, one object, a surface affecting machine as a platform operating in cycles, is self-degrading due to the effects of sequentially repeated cycles. In our hypothesis, it was assumed that the rate of degradation is variable and proportional to the rate of real operations divided by the actual remaining capacity. This novel approach is proved indirectly for the effects occurring on the working surface. These effects are measured by determining the statistical variations of the surface parameters.

The relevance of this model is that the real effects by the cyclic operations and also by the planned operation capacities could be predicted for the required surface effects. The model is also able to predict the extreme machine performances based on the expected quality for the surface treatment.

The presented simulation results are consistent with the experimental data and coincide with the research cited.

Further research in this area could involve an extension of the experimental data base in order to improve the simulation model according to the type of special extreme machines and their affected surfaces.

The model can be readily applied to additional processes and effects. This could be done by exponential redesign of the basic correlations between the rates of operations and the rates of degradations, or by including variable frequencies and probabilities.

5 ACKNOWLEDGMENTS

This paper is a part of the research within the Project III 47029 for MNES-RS in 2014-2015.

6 NOMENCLATURE

$M_p(t)$	current number of operations,
m_p(t)	current number of degraded operations,
$\dot{M}_p$	operation consumptions rate,
$\dot{m}_p$	rate the fictive changes of non-effective operations(rate of equivalent operations),
M_{p_0}	capacity of particular operations,

m_{p_0} initial degraded number of operations,
$m_{p(i-1)}$ initial degraded number from the previous cycle,
N number of cyclic operations,
$m_{p_i}(t)$ current number of operations during degradation,
S_0^* remaining non-degraded surface,
S_p affected surface
$S_{(i-1)}$ remaining non-degraded surface after the $(i-1)^{th}$ cycle,
$S_i(t)$ current non-degraded surface,
Δt cycle period,
PD^* probability dispersion of un-degraded, operations on the platform,
PD probability dispersion of working surface in degraded platforms operations,
U_i designed capability of the platform,
$\alpha_p = \lambda_p$ attrition rate of operations (consumption rate of operation numbers),
p probability of each operation,
$\mu_{p_i}(t)$ current relative degradation in the i^{th} cycle
$\mu_{c_i}(t)$ relative efficiency of the current process,
$\lambda = -N_p(\Delta t)/t$ operation frequency for a given cycle,
$N_p(t)$ number of operations per cycle,
σ elementary efficiency on the surface,
$\mu_p(t)$ current relative capacity degradation,
$\mu_{c_i}^*$ relative efficiency of the current process without degradation,
$\mu_{c_i(i\text{-}1)}$ relative efficiency of the current process, after $i-1$ cycles with degradation effect,
μ_c cumulative relative efficiency of all finished processes.

7 REFERENCES

[1] Gov, K., Eyercioglu, O., Cakir V.M. (2013). Hardness effects on abrasive flow machining. *Strojniški vestnik - Journal of Mechanical Engineering*, vol. 59, no. 10, p. 626-631, **DOI:10.5545/sv-jme.2013.1129**.

[2] Kar, K.K., Ravikumar, N.L., Tailor, P.B., Ramkumar, J., Sathiyamoorthy, D. (2009). Performance evaluation and rheological characterization of newly developed butyl rubber based media for abrasive flow machining process. *Journal of materials Processing Technology*, vol. 209, no. 4, p. 2212-2221, **DOI:10.1016/j.jmatprotec.2008.05.012**.

[3] Rhoades, L. (1991). Abrasive flow machining: a case study. *Journal of Materials Processing Technology*, vol. 28, no. 1-2, p. 107-116, **DOI:10.1016/0924-0136(91)90210-6**.

[4] Zupanc, U., Grum, J. (2011). Surface integrity of shot peened aluminium alloy 7075-T651. *Strojniški vestnik – Journal of Mechanical Engineering*, vol. 57, no. 5, p. 379-384, **DOI:10.5545/sv-jme.2010.142**.

[5] Fang, L., Zhao, J., Li, B., Sun, K. (2009). Movement patterns of ellipsoidal particle in abrasive flow machining. *Journal of Materials Processing Technology*, vol. 209, no. 20, p. 6048-6056, **DOI:10.1016/j.jmatprotec.2009.08.013**.

[6] Lugarić, L., Majdandžić, Lj., Škrlec, D. (2010). Countrywide positioning of domestic solar water heating systems using risk analysis and geographical information system. *Strojniški vesnik – Journal of Mechanical Engineering*, vol. 56, no. 1, p. 3-17.

[7] Przemieniecki, J.S. (2000). *Mathematical Methods in Defense Analyses, 3rd edition.* American Institute of Aeronautics and Astronautics, Redstone.

[8] Maybee, J.S. (1985). The theory of combined-arms lanchester-type models of warfare, *Naval Research Logistic Quarterly*, vol. 32, no. 2, p. 225-237, **DOI:10.1002/nav.3800320204**.

[9] Anderson, L.B. (1993). A heterogeneous shoot-look-shoot attrition process. *Simulation and Gaming*, vol. 24, no. 3, p. 277-293, **DOI:10.1177/1046878193243001**.

[10] Petrovic, D., Milinovic, M., Jeremic, O., Kovac, M., Kapor, N. (2014). Air force support operations and comparative performances. *Symposium of Operational Research*, p. 16-19. (in Serbian)

[11] Ghosh, A., Barman, N., Chattopadhyay, H., Hloch, S. (2013). A study of thermal behaviour during submerged arc welding. *Strojniški vestnik – Journal of Mechanical Engineering*, vol. 59, no. 5, p. 333-338, **DOI:10.5545/sv-jme.2012.775**.

[12] Scales, J.R. (1995). A modified lanchester linear process calibrated to historical data. *Warfare Modelling, 3rd edition*, Military Operations Research Society, Alexandria, p. 345-356.

[13] Milinovic, M., Jeremic, O., Kovac, M., Petrovic, D. (2014). Discrete deterministic modelling of autonomous missiles salvos. *Defence Science Journal*, vol. 64, no. 5, p. 471-476, **DOI:10.14429/dsj.64.5791**.

[14] Zipfel, P.H. (1995). *Modelling and Simulation of Aerospace Vehicle Dynamics*. American Institute of Aeronautics and Astronautics, Reston.

[15] Ball, R.E. (1985). *The Fundamentals of Aircraft Combat Survivability: Analyses and Design*. American Institute of Aeronautics and Astronautics, Redstone.

[16] Anderson, L.B., Miercort, F.A. (1995). On weapons scores and force strengths. *Warfare Modelling, 3rd edition*, Military Operations Research Society, Alexandria.

[17] Law, A.M., Kelton, W.D. (1982). *Simulation Modelling and Analysis*. McGraw-Hill, New York.

Strojniški vestnik - Journal of Mechanical Engineering 61(2015)3, 176-186

DOI:10.5545/sv-jme.2014.1914 Original Scientific Paper
Received for review: 2014-04-22
Received revised form: 2014-07-25
Accepted for publication: 2014-10-22

Selection of Optimum Process Parameters in High Speed CNC End-Milling of Composite Materials Using Meta Heuristic Techniques – a Comparative Study

Vikas Pare – Geeta Agnihotri – Chimata Krishna*
Maulana Azad National Institute of Technology, Bhopal, India

The machining of aluminium metal matrix composites in CNC high speed conditions is significant because such composites have diverse applications in the aeronautics industry. Because that industry requires high quality outcomes, the prediction of surface roughness, which depends on input process parameters, assumes significance in the maintaining quality of products. Even though many researchers have worked in the area of conventional machining, very few of them have explored optimization techniques, such as teaching-learning-based optimization (TLBO) and gravitational search algorithms (GSA) in high speed environments. In this research, an attempt is made to determine the optimum machining conditions for the end-milling of composite materials using GSA. Input process parameters, such as cutting speed, feed, the depth of cut and the step-over ratio are taken as independent variables, and surface roughness is taken as dependent variable. Experiments were conducted on Al_2O_3 + SiC metal matrix composite by considering selected variations in the input process parameters. Surface roughness is measured in each of cases, and the required data is obtained for further analysis. An empirical relationship is established between dependent and independent variables in the form of linear and non-linear regression equations, and the results are analysed. The results showed that GSA gives better results for surface roughness when compared to the genetic algorithm, simulated annealing and TLBO methods. An additional set of experiments was conducted to validate the results obtained.

Keywords: high-speed machining, metal matrix composite, surface roughness, gravitational search algorithms, teaching-learning-based optimization

Highlights
- *Preparation of composite material of best mechanical properties.*
- *Microstructure analysis to study the machinability of composite material.*
- *Modelling of input parameters with surface roughness for high speed CNC machining of composite material.*
- *Optimization of surface roughness using gravitational search algorithm.*
- *Validation of results by conducting additional set of experiments.*

0 INTRODUCTION

High speed milling (HSM) has assumed importance in recent years due to increased demand for quality, productivity and cost reduction in manufacturing [1]. HSM can be used mostly for relatively softer materials and the production of components in mass scale. The machining of the aluminium metal matrix composite is a significant high-speed milling application. This technology has wide application in the aeronautics or aerospace sectors, and the moulds and die industry [2] and [3].

A metal matrix composite is made by combining at least two constituent parts, one of which must be a metal. Normally, other constituents may be different materials, such as ceramics or organic compounds. In this paper, silicon carbide is used as second constituent, as it reduces the cost of resultant composites. In order to obtain the required properties in the matrix alloy, the reinforcement material, the volume of the reinforcement, location and the shape of the reinforcement and fabrication method can all be varied [4]. The objective involved designing a metal matrix composite material mainly by adding the desirable attributes of metals and ceramics. The steps involved with castings of metal matrix composite are as follows:

- Melting the aluminium metal with 5, 10, 15 and 20 % on a mass fraction basis;
- Pouring it into an already prepared mould or cavity, which has the shape of the desired component;
- Cooling and solidifying the molten metal in the mould; and
- Removing the solidified component from the mould and cleaning it properly.

The machinability of aluminium composites is considerably high in comparison to other materials. Whether the material is stable after a high-speed milling operation is performed on it needs to be studied; i.e. the structure of material needs to be checked after machining. Surface roughness is a measure of the technological quality of a product and has influence on manufacturing cost and the quality of the product. Therefore, industries always choose to maintain the good quality of the machined

*Corr. Author's Address: Mechanical Engineering Department: MANIT, Bhopal, India,462051, cmk_manit@rediffmail.com

surface. The surface roughness and material removal rate considerably change with the variation of cutting process parameters; thus, the appropriate selection of process parameters has significant role in the prediction of the surface finish and material removal rate in the high-speed end-milling process. Therefore, it needs to be studied in the context of the machining of aluminium composites as well in high-speed machining conditions.

Theoretical models have been proposed for the selection of process parameters by earlier researchers [5] to [7]. However, they do not yield good results under all the conditions of experimentation. As a result, machine operators generally use trial-and-error approaches to set up milling machine cutting conditions in order to achieve the required surface roughness. These methods are not productive and are extremely time consuming. Therefore, establishing empirical relations between output parameters, such as surface roughness and input process parameters, and then optimizing the output parameters will result in reasonably accurate results in HSM. However, there are many problems associated with the optimization of large-scale problems, such as multimodality, dimensionality and differentiability. Conventional approaches, e.g. linear and dynamic programming, etc., are not efficient in solving non-linear objective functions. Therefore, to develop efficient and effective optimization techniques is a matter of great urgency. Research is being conducted in this field and nature-inspired meta-heuristics optimization approaches are considered better than the traditional techniques, and thus are prominently used.

One of the most efficient and effective optimization techniques reported is the gravitational search algorithm (GSA), which was developed by Rashedi et al. [8] and is based upon the gravitational and motion laws of Newton, where by every particle is considered an agent in the universe. The particles attract each other with a force that is dependent on their masses and distances. An optimization method, such as teaching-learning-based optimization (TLBO), is also used for obtaining global solutions instead of local optimal solution for continuous non-linear functions. The TLBO method works on the philosophy of teaching and learning [9]. These methods may not offer the best solutions to all types of problems. Some of them yield their best results for specific cases and thus other methods result in optimum values for other types of problems. Therefore, it is important to consider a few soft computing techniques for applications in order to know which best suits the given problem.

In this work, the structure of casting of aluminium silicon carbide is tested for uniformity of distribution, by using an electron microscope before machining. Experiments were conducted on this material using a CNC high-speed machine by varying four selected input parameters: cutting speed, feed, depth of cut and step over ratio. The structure of material is also tested, using an electron microscope after machining.

The surface roughness is measured using Taylor Hobson surface roughness tester (Surtronic 3+) for each of the forty selected combinations of input parameters. The surface roughness tester has a traverse speed of 1 mm/s; the measurement unit is mm present by the dual in-line package (DIP) switch, deselected via the menu; its cut-off values are 0.25, 0.8, and 2.5 mm; its traverse length ¼ Lambda $+n$ Lambda ($n = 1, 3, 5, 10$ or $25.4 + 0.2$ mm at 0.8 mm cut-off); its parameters are R_a, R_q, R_z (DIN), R_y and S_m; its calculation time is less than reversible time or 2 s, which ever is longer. An empirical relationship between surface roughness and the input parameters is established using the MINITAB software package. The empirical equations thus obtained are optimized using GSM, TLBO, simulated annealing (SA) and genetic algorithm (GA) methods, and the results are compared.

This paper is organized as follows: in addition to the introduction in this section, a brief review of literature is given in Section 1. Experimental set up and conduction of experiments is explained in Section 2, and the results obtained and analysis are explained in Section 3. The conclusions drawn are given in Section 4.

1 LITERATURE REVIEW

The results of some of the researchers who worked on conventional machines and high-speed CNC machines by varying selected input parameters are presented in the following section. The literature includes only soft computing applications and meta-heuristic methods in the analysis of machining parameters for composite materials.

1.1 Composite Material

Pathak et al. [4] presented the preparation of an aluminium silicon carbide composite. They have also given a detailed discussion about the microstructure and its different mechanical properties. Neelima Devi et al. [10] studied the characterization of an aluminium silicon carbide composite. In their paper, tensile strength experiments were conducted by varying mass

fraction of SiC (5, 10, 15, and 20 %) with aluminium. Palanikumar and Karthikeyan [3] investigated the factors influencing the surface roughness on the machining of Al/SiC particulate composites, using tungsten carbide tool inserts (K10). Dabade et al. [11] studied the surface integrity as a function of process parameters and tool geometry by analysing cutting forces, surface finish, and microstructures of the machined surfaces on Al/SiC/10p and Al/SiC/30p composites using cubic boron nitride (CBN) inserts. Basheer et al. [12] presented a model to predict the surface roughness in precise machining of metal matrix composites, using PCD tools with respect to the size and volume of reinforcement, tool nose radius, feed rate, and the depth of cut. Very few of them worked with composites in HSM conditions and checked the stability of composite by testing the microstructure after machining.

1.2 Conventional Machining

Some researchers used statistical methods for analysing the relationships between surface roughness and selected input parameters. Aluminium metal matrix composite was used by Seeman et al. [13] whereas LM25 Al/SiC_p composite was used by Arokiadass et al. [2]. Both used surface roughness and tool wear as output variables in their studies. They used RSM for establishing the relationship between input and output variables and conducted statistical analysis. Seeman et al. used machining time (t), estimated flank wear ($V_B$max) and surface roughness (R_a) in addition to the three parameters used by most of the researchers.

Other researchers used soft computing techniques for analysis. The application of the GA method is the most common method found in the literature. Bhushan et al. [14] studied the 7075 Al alloy SiC composites and applied the GA technique to optimize the machining parameter in turning operations. Rai et al. [15] studied the multi-tool milling and estimated the machining time by applying GA techniques, taking axial depth of cut, radial immersion, feed rate and spindle speed as input parameters. Del Prete et al. [16] studied the flat end-milling process with feed, depth of cut, radial engage and speed as input parameters. Xu et al. [17] estimated various output parameters, such as cutting force, tool life and machined surface roughness by taking feed rate, depth of cut and cutting width as input parameters. Saffar and Razfar [18] estimated cutting force in the end-milling process by taking speed, feed rate and radial rake angle as input parameters. Alam et al. [19] predicted the surface roughness by considering speed, feed rate, and depth of cut as input parameters. They applied both the GA and quadratic prediction models to optimize the machining process parameters for the minimum surface roughness.

Rao et al. [9] proposed TLBO for the optimization of mechanical design problems. In their paper, he compared this technique with other techniques and proved TLBO to be best. Rao et al. [5] also used TLBO techniques for non-linear large scale problems and compared the results with those obtained by other techniques such as GA, particle swarm optimization (PSO) and artificial bee colony (ABC) techniques, and obtained the best results.

There is no specific heuristic algorithm suitable for all types of problems. The methods used may result in better solutions under specific conditions. Li et al. [20] developed models to estimate the cutting force, tool life and surface roughness. They applied PSO to improve the result. Pare et al. [21] used speed, feed, the depth of cut and the step-over ratio as input variables and optimized surface roughness using PSO. Unlike PSO, in which the two best positions decide the direction of search, GSA uses the weight of all agents for finding new search directions. Zubaidi et al. [22] applied the GSA for the optimization of cutting conditions for end-milling Ti6A14V alloy and obtained results that were proved to be better in comparison to GA and PSO techniques.

In addition to the above application of heuristic search-based algorithms, some researchers combined selected algorithms (hybrid) and made attempts to apply them in different contexts. Farahnakian et al. [23] studied end-milling with PSO combined with a neural network (NN) algorithm to predict surface roughness and cutting forces. Cus and Zuperl [1] compared the PSO, GA and SA techniques to estimate the cutting force, the best results were obtained with PSO. Huang et al. [24] studied end-milling process and deployed PSO to minimize tool wear. They took speed, feed rate and width and observed that the memetic PSO (MPSO) algorithm has better performance than back-propagation NN, conventional wavelet neural networks (WNN) and GA-based WNN.

Other works in this area include Zain et al. [25], who studied three parameters of end-milling for minimizing surface roughness. Based on the experimental data, it was concluded that process parameters should be set at the highest cutting speed and the rake angle with the lowest feed in order to obtain the minimum surface roughness. In the area of the face-milling operation, Back et al. [26] studied the effects of the insert run-out errors and the variation of the feed rate on the surface roughness. Thambu et al.

[27] observed the machining of die cast Al alloy-SiC composites. Machining studies were conducted on the AlSiC composite work pieces with high-speed steel (HSS) end-mill tools in a milling machine at different speeds and feeds. Dweiri et al. [28] studied the down-milling machining process of Alumic-79 with an adaptive neuro fuzzy inference system to estimate the effect of machining variables, i.e. spindle speed, feed rate, depth of cut and number of flutes on the surface finish. Fuht and Wu [29] analysed the effect produced by the tool geometries and cutting conditions on the machined surface quality and developed a model predicting the surface quality for aluminium.

1.3 High Speed Machining

Most of the researchers used statistical analysis methods in the area of high speed machining. They considered different sets of input parameters, output parameters and tried various analysis techniques based on statistics, including structured equation modelling (SEM) analysis, robust design, and Taguchi design approaches. Kauppinen [30] observed the results of several projects on high-speed milling for testing the suitability of high-speed milling for different kinds of materials. The materials machined were steels, aluminium alloys, graphites and polymer matrix composites. It is observed that most of the materials can be machined by high-speed milling.

Pare et al. [31] conducted experiments varying the speed from 2500 to 7500 rpm on composites. They developed predictive models for surface roughness and used GSA for optimization. In order to determine whether there is uniform variation of surface roughness over speed variation, the range of 5000 to 7500 rpm was taken into consideration. TLBO [32] was used, and the results were studied.

Koshy et al. [33] studied high-speed end-milling of hardened AISI D2 tool steel (58HRC) and estimated surface roughness and tool wear. Ozcelik and Bayramoglu [6] considered the step-over ratio in addition to the three cutting variables and developed a surface roughness prediction model for wet machining conditions. De Souza Jr. et al. [34] examined two face-milling cutter systems in the high-speed cutting of grey cast iron under a determined cutting condition. El-Wahab and Kishawy [35] deployed mathematical models to enhance the surface quality during CNC machining. Axinte and Dewes [36] observed the experimental results and related empirical models for work piece surface integrity (SI) during high-speed machining.

Ghani et al. [37] implemented Taguchi optimization methodology to optimize cutting parameters, e.g. speed, feed and depth of cut, in end-milling during the machining of hardened steel with a TiN-coated carbide insert tool considering semi-finishing and finishing conditions of high-speed milling. The milling parameters used are cutting speed, feed rate and depth of cut. From the analysis of the result, the optimal combination of process parameters for the resultant low cutting force and good surface finish was determined. Arokiadass et al. [2] studied the machining properties of LM25 Al/SiCp composite in high-speed end-milling. They deployed the RSM and prepared a mathematical model to estimate the high-speed end-milling process parameter.

Some researchers used either soft computing techniques or meta-heuristic techniques for the development of relationships among selected output and input variables. Yong et al. [38] studied high-speed milling processes with the axial depth of cut, radial depth of cut and helical angle as input parameters. They applied GA to estimate cutting force and MRR and achieved very good results. Öktem et al. [7] developed a methodology in order to determine the optimum cutting conditions leading to minimum surface roughness in the milling of mould surfaces, by coupling RSM with a developed GA. RSM was utilized to create an efficient analytical model for surface roughness in terms of cutting parameters: feed, cutting speed, axial depth of cut, radial depth of cut and machining tolerance.

Therefore, there is a need to study in detail how surface roughness varies in wider speed ranges in the case of HSM. There is scope for computing the best machining conditions under high-speed machining for composite materials and applying new heuristic techniques, such as TLBO and GSM, in the area in order to obtain better results. The experimental procedure and results and analysis are explained in subsequent sections.

2 EXPERIMENTAL PROCEDURE

The experimental procedure involves four stages: (i) the selection of proper combination of composite material, necessary cutting tools, and required equipment, (ii) data collection by conducting experiments as per the defined plan, (iii) the establishment of a surface roughness prediction model, and (iv) optimization of the predictive model for better results. Each of the stages is explained in the following sub-sections.

2.1 Selection of Proper Combination of Composite Material, Cutting Tools and Equipment

The experimental study was carried out in dry cutting conditions on a high-speed CNC vertical milling machine (Model-Agni-BMV-45-T-20-Year 2008). Others features are a maximum spindle speed of 10,000 rpm, clamping area of 450×900 mm², feed rate of 1 to 1000 µm/rev, 15-kW drive motor with a table size of 800×500×550 mm³. The work piece material used was aluminium silicon carbide composite in the form of a 55×55×22 mm³ block. The gravity die-casting method was used for the preparation of Al-SiC material. The hardness of the composite material increased with the increase in the percentage of SiC in the composite. The percentage of constituents is selected based on experimentation with various combinations of Al and SiC and testing the mechanical properties of component. Trial machining is done and the microstructure is also tested before and after trail machining. The material properties of aluminium silicon carbide material are shown in Tables 1 and 2. A flat end mill (25 mm diameter, 45 *1* helix angle, 4-flutes) produced by Addison was used for machining.

Table 1. *Chemical composition of (wt %) Al SiC*

Al	SIC	Fe	Co
84.5	15.45	0.03	0.02

Table 2. *Mechanical properties of aluminium silicon carbide composite*

Work material	Tensile strength	Elongation	Density	Hardness
Al SiC composite	145.32 N/mm²	5.5 %	2779 kg/m³	63.8 BHN

2.1.1 Microstructure Analysis

Testing of properties of Al-SiC before machining and micro-structure analysis is one of the methods to study the properties of composites material. A scanning electron microscope is used to observe the microstructure of composite material; after this analysis, various materials used in the composite can easily be observed. To perform the micro-structure analysis, a sample has been cut as per the requirement. Different degrees of fine papers were used to rub the sample starts with 600, 800, 1000, 1200 and 1500 degrees. Later, it was again rubbed, using a velvet cloth on polishing machine to finally check the microstructure. Etching solution (a mixture of 10 g NaOH, 5 g of K4 (Fe (CN)6) and 100 ml distilled water) was used to observe the microstructure of composite.

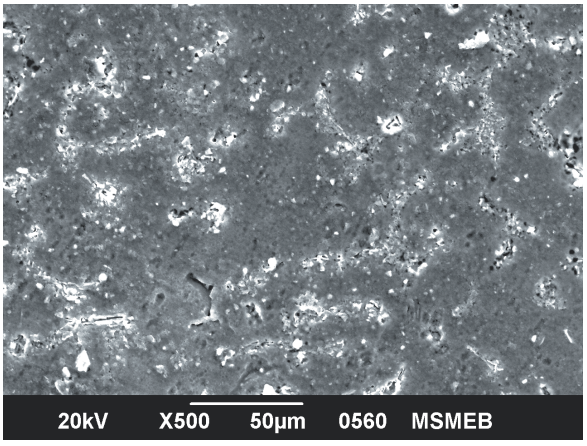

Fig. 1. *Micro structure of aluminium silicon carbide composite*

This microstructure showed mixing of aluminium and silicon carbide particles in uniform way as shown in Fig. 1. In the microstructure, if particles are segregated near grain boundaries it ideally means that the composite has high hardness; if it is away from grain boundaries, it means it has less hardness. In this case, many particles are going away from grain a boundary, which means that it is highly machinable and very useful for industrial purposes, especially in the aerospace and satellite industries.

2.1.2 Surface Roughness Measurement

A portable Surtronic 3+ was used to measure the surface roughness (shown in Fig. 2). Four readings have been taken in the traverse direction. In case there is a large deviation, extreme values are discarded and additional readings have been taken so that the total number of readings is four.

Fig. 2. *Surface roughness measurement using Surtronic 3+*

The average value of surface roughness is calculated and recorded. In this study, R_a values

were obtained in the range of 1.25 to 3.50 mm. This variation is significant for aluminium composites in HSM for applications in the aerospace industry. The repeatability of the measurements was found to be in the range of 2 to 5 %, which was considered satisfactory for generating empirical models using the variables spindle speed, feed rate, depth of cut and step-over ratio.

2.2 Collection of Data by Conducting Experiments as per the Plan

In this study, experimental work was conducted with aluminium silicon carbide composite material on a high-speed CNC milling machine. Five different values of cutting speeds (2000, 3000, 4000, 5000 and 6000 rpm) two values for the feed ranging from 100 and 200 μm/rev, two values of depth of cut (0.2 and 0.4 mm), and two values of the step-over ratio (50 and 60 %), have been taken to conduct the experiments. In this way (5×2×2×2), a total of 40 experiments were designed and conducted in this study and the data is tabulated in Table 5. Five different values are taken for cutting speed, as the range of speed in CNC HSM is very wide. The experiments conducted beyond the 6000 rpm speed range are not presented in this paper, as the variation in surface roughness obtained is marginal.

2.3 Establishment of Predicted Model for the Selected Output Measure

A prediction model for surface roughness is established by taking surface roughness as a dependent variable and input variables (cutting speed, depth of cut, feed and step-over ratio) as independent variables. A regression relationship is established between them, and the statistical tests (*F*-test and *t*-tests) are carried out to test the significance levels. Both linear regression and non-linear regression are attempted.

In linear regression analysis, the general form of equation is:

$$R_a = a_1x_1 + a_2x_2 + a_3x_3 + a_4x_4 + K\,. \tag{1}$$

Similarly, general form of non-linear equation is:

$$R_a = K \times x_1^{a_1} \times x_2^{a_2} \times x_3^{a_3} \times x_4^{a_4}, \tag{2}$$

By taking logarithms on both sides:

$$log_{10}(R_a) = a_1 \times log_{10}(x_1) + a_2 \times log_{10}(x_2) + \\ + a_3 \times log_{10}(x_3) + a_4 \times log_{10}(x_4) + log_{10}(K)\,. \tag{3}$$

In both the above cases, a_1, a_2, a_3, and a_4 are parameters and x_1, x_2, x_3, and x_4 representthe selected input variables of cutting speed, feed, the depth of cut, and the step-over ratio, respectively. K denotes a constant.

2.4 Optimization of Predictive Model

The ultimate objective of the optimization process for any problem is to assign values to a set of variables that will result in the best performance of a system. These setting variables can be calculated through deterministic or non-deterministic methods. In the deterministic method, a bottleneck is a local minima and in this regard artificial intelligence optimizing techniques are a better option.

The predictive model obtained in the above sub-section is optimized by using four meta-heuristic algorithms (GSA, TLBO, SA and GA) and is explained in the following sub-section as other algorithms are available in the literature. The program code for GSA is developed using MATLAB 2012.

2.4.1 Gravitational Search Algorithm

The concept of algorithm is as follows: the performance of the agents that are considered as the objects is calculated by their masses. As in space, all these objects are attracted to each other because of gravitational force, and a shifting of smaller masses towards heavier masses takes place. The heavier masses, due to weight, change their positions more slowly in comparison to lighter ones. There can be four classifications for the masses: active, passive, inertial mass and position. A correlation can be established as the position of the masses, and the solution of the problem is similar. A fitness function is applied to determine its gravitational and inertial masses.

The GSA is governed by two laws: (i) the law of gravity, and (ii) the law of motion. According to law of gravity, every point mass in the universe attracts every other point mass with a force that is directly proportional to the product of their masses and inversely proportional to the square of the distance between them [8]. The law of motion states that the current velocity of any mass will be equal to the sum of the fraction of its previous velocity and the variation within the velocity. Variation in the velocity of any mass is equal to the force acted on the system divided by mass of inertia. The different steps of the GSA are as follows:

- The first population is initialized to start.

- The fitness of each agent is evaluated and values are recorded.
- G is updated and the best and worst fitness rates in the population for $i = 1, 2, ..., N$ are selected.
- M (weighting in range [0, 1]) is updated. Then update K_{best} and calculate F. Then update a.
- The velocity and the position are updated: All positions should be in a feasible range.
- Repeat steps 2 to 5 until the stop criteria.
- End.

The following parameters must be set in GSA:

- Population size, N: the number of agents.
- Dimension, D: The control variables number.
- Maximum iteration, T: number of iterations to stop the optimization process if there is no convergence.
- Initial gravity, G_0: initial value of gravity, G.

GSA is a memory-less algorithm and very effective in most types of optimization problems.

3 RESULTS AND DISCUSSIONS

The microstructure of the composite material of the selected combination showed no significant difference before and after machining, thus indicating the material is stable over the selected range of speed variation. The microstructure after machining is shown in Fig. 3. In this paper, linear and non-linear relationships were established between input and output parameters to predict surface roughness. Four heuristic methods (GA, SA, TLBO and GSA) are used for optimization.

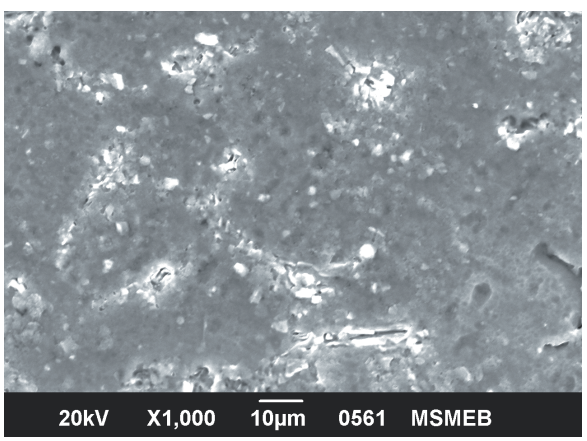

Fig. 3 *Micro-structure of aluminium silicon carbide composite*

All these four techniques are fundamentally different from each other: GA is based upon the survival of fittest, SA is based upon annealing, TLBO is inspired by the teaching-learning method and GSA is inspired by natural phenomenon of gravitational law. It is important to compare the result of these techniques so as to select the best technique for this case.

Table 3. Selected input parameter

Parameter	Smallest value	Largest value
Speed (x_1) [m/min]	2000	6000
Feed (x_2) [μm/rev]	100	200
Depth of cut (x_3) [mm]	0.2	0.4
Step-over ratio (x_4)	0.5	0.6

MATLAB 2012 was used for preparation of codes. The ranges taken for conducting experiments with the selected input variables are given in Table 3. The smallest value is taken as 2000 rpm for the cutting speed, as the lower speed values are covered in the case of conventional machines by earlier researchers for this case. Based on the selected range, experiments were conducted on a high-speed CNC machine, and data was collected by varying the cutting speed, feed, and depth of cut and step-over ratio while machining the Al-SiC composite material. In this experiment, coolant was not used and other indirect factors (machine vibration, machine tolerance, and operator performance) are assumed to be insignificant. The combinations of input variables and the measured output variable are given in Table 4.

Table 4. *Experimental data*

S. no	x_1	x_2	x_3	x_4	R_a	S. no	x_1	x_2	x_3	x_4	R_a
1	2000	100	0.2	0.5	2.30	21	4000	200	0.2	0.5	2.10
2	2000	100	0.2	0.6	3.03	22	4000	200	0.2	0.6	2.46
3	2000	100	0.4	0.5	2.62	23	4000	200	0.4	0.5	2.34
4	2000	100	0.4	0.6	3.13	24	4000	200	0.4	0.6	2.65
5	2000	200	0.2	0.5	2.65	25	5000	100	0.2	0.5	1.45
6	2000	200	0.2	0.6	3.18	26	5000	100	0.2	0.6	1.63
7	2000	200	0.4	0.5	2.95	27	5000	100	0.4	0.5	1.51
8	2000	200	0.4	0.6	3.25	28	5000	100	0.4	0.6	1.79
9	3000	100	0.2	0.5	2.15	29	5000	200	0.2	0.5	1.48
10	3000	100	0.2	0.6	2.51	30	5000	200	0.2	0.6	1.60
11	3000	100	0.4	0.5	2.45	31	5000	200	0.4	0.5	1.88
12	3000	100	0.4	0.6	2.90	32	5000	200	0.4	0.6	1.99
13	3000	200	0.2	0.5	2.26	33	6000	100	0.2	0.5	1.62
14	3000	200	0.2	0.6	2.63	34	6000	100	0.2	0.6	1.69
15	3000	200	0.4	0.5	2.54	35	6000	100	0.4	0.5	1.74
16	3000	200	0.4	0.6	3.02	36	6000	100	0.4	0.6	2.10
17	4000	100	0.2	0.5	1.98	37	6000	200	0.2	0.5	1.91
18	4000	100	0.2	0.6	2.24	38	6000	200	0.2	0.6	2.19
19	4000	100	0.4	0.5	2.20	39	6000	200	0.4	0.5	1.93
20	4000	100	0.4	0.6	2.54	40	6000	200	0.4	0.6	2.30

The regression equation, which relates the dependent variable, surface roughness and independent variables as given in Table 1, is given in Eq. (4).

$$R_a = 0.893 - 0.00028x_1 + 0.00186x_2 + \\ +1.19x_3 + 3.39x_4 . \quad (4)$$

In this analysis, p values are close to zero and the F value is 43.77 which are considered a good fit between the dependent and independent variables. Similarly, with the help of MINITAB software based on the same 40 experimental data points, a non-linear regression equation was developed, given in Eq. (5).

3.1 Linear Regression Analysis

For linear regression analysis and an associated statistical test to calculate a p value, for the coefficients associated with each independent variable, the MINITAB software package is used.

$$log_{10}(R_a) = 1.99 - 0.454\,log_{10}(x_1) + 0.124\,log_{10}(x_2) + \\ + 0.157\,log_{10}(x_3) + 0.794\,log_{10}(x_4). \quad (5)$$

Table 5a. *Results of test of significance of independent variables – linear regression*

Predictor	Coef	SE Coef	t	P
Constant	0.8925	0.4195	2.13	0.041
v	–.0002799	0.0000244	–11.48	0.00
f	.0018650	0.0006897	2.70	.011
d	1.1925	0.3449	3.46	.001
sr	3.3850	0.6897	4.91	0.00
S = 0.218111 R – Sq = 83.3 % R – Sq(adj) = 81.4 %				

Table 5b. *Results of analysis of variance*

Source	DF	SS	MSE	F value	P value
Regression	4	8.3289	2.0822	43.77	0.00
Residual error	35	1.6650	0.0476		
Total	39	9.9939			

In Table 5a, the associated variable is an effective and efficient predictor. The R^2 value in statics also is key parameter because it indicates model performance. In this case, the R^2 value is 81.4 % and this model explains 81.4 % of the variation in the dependent variable. In Table 5b, residual errors are the unexplained portion of the dependent variable; a large residual error means model is unfit but in this case residual error is not too much so this model is fit for prediction. The results suggest that all the four input parameters have significant effects on surface roughness.

3.2 Non-Linear Regression Analysis

In this study, non-linear regression analysis is performed with experimental data. In Table 6, the test of significance and variance**,** p value is 0.01, so it is statistically significant at a 99 % confidence level, and the associated variable is an effective and efficient predictor. Standard error estimates are very low for all four parameters, which indicates that this model is fit for prediction of surface roughness. The coefficients of non-linear regression equation clearly indicate that the effect of all the process parameters is significant on the surface roughness.

Table 6a. *Results of test of significance –non-linear regression*

Predictor	Coef	SE Coef	t	P
Constant	1.9944	0.1876	10.63	0.000
v	-0.4542	0.04174	-10.88	0.000
f	0.1242	0.04673	2.66	0.012
d	0.1569	0.04673	3.36	0.002
sr	0.7940	0.1776	4.47	0.000
S = 0.0444809 R – Sq = 81.7 % R – Sq(adj) = 79.7 %				

Table 6b. *Results of analysis of variance – linear regression*

Source	DF	SS	MSE	F value	P value
Regre-ssion	4	0.310046	0.0775	39.18	0.00
Residual error	35	0.069249	0.00198		
Total	39	0.379295			

3.3 Optimization Using Selected Heuristic Methods

After developing the relationships between dependent and independent variables using linear and non-linear regression methods, four optimization techniques were used, as explained earlier, and the results are given in Tables 7 and 8 for linear and non-linear relations, respectively.

The results obtained using the four selected techniques reveal that higher speed is desirable in order to obtain a minimum surface roughness value. In the case of feed rate, the values varied from 101.56 to 192.3 μm/rev; only one value was close to 200 and other three values were close to 100 μm/rev, indicating that the low value of feed is desirable for minimum surface roughness. In the case of depth of cut, three values are close to 0.2 mm, indicating that a low value of depth of cut is desirable for minimum surface roughness. The step-over ratio varies from 0.5 to 0.6, three values are close to 0.5, and one value is close to 0.6. As the number of iterations is greater in

the case of SA and GSA, it may be concluded that a step-over ratio of 0.5 is desirable for further work.

Table 7. *Comparison of four selected optimization methods – linear regression (LR)*

Parameter	GA	SA	TLBO	GSA
x_1	5702.37	2238.07	5950.2	5739.88
x_2	147.026	101.564	192.3	105.357
x_3	0.24049	0.2	0.3	0.237
x_4	0.5067	0.6	0.5	0.5224
R_a [μm]	1.57	2.389	1.63	1.53
Iteration	51	6307	5	1000

Table 8. *Comparison of four selected optimization methods – non-linear regression (NLR)*

Parameter	GA	SA	TLBO	GSA
x_1	5127.23	2846.235	4677.3	5984.9
x_2	102.467	102.434	161.2	124.71
x_3	0.2	0.2	0.3	0.216
x_4	0.519	.5	0.5	0.5074
R_a [μm]	1.66	2.09	1.88	1.571
Iteration	59	5953	5	1000

From the analysis for non-linear relationship, it was observed from the Table 8 that cutting speed varies from 2846.24 to 5984.9 rpm, indicating that higher speed is desirable for minimum surface roughness. Similarly, a lower value of feed, a lower value of depth of cut and a 50 % step-over ratio is required for minimum surface roughness. From Tables 7 and 8, GSA gives the minimum value of surface roughness as compared to other selected techniques. Therefore, it may be concluded that GSA is very effective in comparison to other techniques.

3.4 Validation of Results

For validation purposes, four separate experiments were conducted, and the data were recorded. The value of surface roughness is computed using Eqs. (4) and (5). The results are presented in Tables 9 and 10. It is observed that the maximum percentage of error was –12.0 % and thus the results are validated. From results, it is clear that the non-linear regression equation better describes the data, as the range of percentage error is 10.1 as compared to range of percentage error of 16.01 % in the case of linear regression relation. Therefore, Eq. (5) fits the data better as far as validation results and best fit tests are concerned.

Table 9. *Validation of results for LR*

x_1	x_2	x_3	x_4	R_a (actual) R_{aa}	R_a (predicted) R_{ap}	Difference $(R_{ap} - R_{aa})$	Error ×100 [%]
3000	150	0.4	0.6	2.82	2.842	0.022	0.7
4000	150	0.4	0.5	2.14	2.223	0.0.083	3.73
6000	150	0.2	0.6	1.60	1.425	–0.175	–12.28
6000	150	0.4	0.5	1.75	1.663	–0.090155	–5.2

Table 10. *Validation of results for NLR*

x_1	x_2	x_3	x_4	R_a (actual) R_{aa}	R_a (predicted) R_{ap}	Difference $(R_{ap} - R_{aa})$	Error ×100 [%]
3000	150	0.4	0.6	2.82	2.77	–0.05	–1.8
4000	150	0.4	0.5	2.14	2.10	-0.04	–1.9
6000	150	0.2	0.6	1.60	1.814	+0.214	11.7
6000	150	0.4	0.5	1.75	1.75	0.00	0

4 CONCLUSIONS

In this research, the microstructure of Al SiC composite is found to be stable after testing it before and after machining in HSM. The surface roughness models after optimization using four meta-heuristic techniques reveal that GSA proved to be the best among the four techniques in terms of optimum value of surface roughness and that TLBO gave better result in terms of number of iterations. The non-linear regression equation better explains the relationship between surface roughness and input parameters. This study can be a basis for future researchers as more input parameters need to be taken into consideration in order to predict the surface roughness at much higher speeds, i.e. of 6000 rpm onwards. The interaction effects, if any, can also be studied by future researchers. There is a scope to consider more such composite materials with various combinations of constituent materials under high-speed cutting conditions in order to compute the optimum values of input machining conditions for better design of manufacturing processes.

5 REFERENCES

[1] Cus, F., Zuperl. (2007). Particle swarm intelligence based optimization of high speed end milling. *Journal of Achievements in Materials and Manufacturing Engineering*, vol. 22, no. 2, p. 75-78.

[2] Arokiadass, R., Palaniradja, K., Alagumoorthi, N. (2012). Prediction and optimization of end milling process parameters

of cast aluminium based MMC. *Transactions of Nonferrous Metals Society of China*, vol. 22, no. 7, p. 1568-1574, **DOI:10.1016/S1003-6326(11)61357-5**.

[3] Palanikumar, K., Karthikeyan, R. (2007). Assessment of factors influencing surface roughness on the machining of Al/SiC particulate composites. *Materials and Design*, vol. 28, no. 5, p. 1584-1591, **DOI:10.1016/j.matdes.2006.02.010**.

[4] Pathak, J.P., Singh, J.K., Mohan, S. (2006). Sythensis and characterization of aluminium silicon carbide composite. *Indian Journal of Engineering & Material Science*, vol. 13, no. 3, p. 238-246.

[5] Rao, R.V., Savsani, V.J., Vakharia, D.P. (2012). Teaching–learning based optimization: an optimization method for continuous non-linear large scale problems. *Information Science*, vol. 183, no. 1, p. 1-15, **DOI:10.1016/j.ins.2011.08.006**.

[6] Ozcelik, B., Bayramoglu, M. (2006). The statistical modeling of surface roughness in high-speed flat end milling. *International Journal of Machine Tools & Manufacturing*, vol. 46, no. 12-13, p. 1395-1402, **DOI:10.1016/j.ijmachtools.2005.10.005**.

[7] Öktem, H., Erzurumlu, T., Kurtaran, H. (2005). Application of response surface methodology in the optimization of cutting conditions for surface roughness. *Journal of Material Processing Technology*, vol. 170, no. 1-2, p. 11-16, **DOI:10.1016/j.jmatprotec.2005.04.096**.

[8] Rashedi, E., Nezamabadi-pour, H., Saryazdi, S. (2009). GSA: A gravitational search algorithm. *Information Sciences*, vol. 179, no.13, p. 2232-2248, **DOI:10.1016/j.ins.2009.03.004**.

[9] Rao, R.V., Savsani V.J., Vakharia, D.P. (2011). Teaching-learning-based optimization: A novel method for constrained mechanical design optimization problems. *Computer Aided Design*, vol. 43, no. 3, p. 303-315, **DOI:10.1016/j.cad.2010.12.015**.

[10] Neelima Devi, C., Mahesh, V., Selvaraj, N. (2011). Mechanical characterization of aluminium silicon carbide composite. *International Journal of Applied Engineering Research*, vol. 1, no. 4, p. 793-799.

[11] Dabade, U.V., Joshi, S.S., Balasubramaniam, R., Bhanuprasad, V.V. (2007). Surface finish and integrity of machined surfaces on Al/SiCp composites. *Journal of Materials Processing Technology*, vol. 192-193, p. 166-174, **DOI:10.1016/j.jmatprotec.2007.04.044**.

[12] Basheer, A.C., Dabade, U.V., Joshi, S.S. (2008). Modeling of surface roughness in precision machining of metal matrix composites using ANN. *Journal of Materials Processing Technology*, vol. 197, no. 1-3, p. 439-444, **DOI:10.1016/j.jmatprotec.2007.04.121**.

[13] Seeman, M., Ganesan, G., Karthikeyan, R., Velayudham, A. (2010). Study on tool wear and surface roughness in machining of particulate aluminium metal matrix composite-response surface methodology approach. The International Journal of Advanced Manufacturing Technology, vol. 48, no. 5-8, p. 613-624, **DOI:10.1007/s00170-009-2297-z**.

[14] Bhushan, R.K., Kumar, S., Das, S. (2012). GA approach for optimization of surface roughness parameters in machining of Al alloy SiC particle composite. *Journal of Materials Engineering and Performance*, vol. 21, no. 8, p. 1676-1686, **DOI:10.1007/s1665-011-0066-2**.

[15] Rai, J.K., Brand, D., Slama, M., Xirouchakis, P. (2011). Optimal selection of cutting parameters in multi-tool milling operations using a genetic algorithm. *International Journal of Production Research*, vol. 49, no. 10, p. 3045-3068, **DOI:10.1080/00207540903382873**.

[16] Del Prete, A., De Vitis, A.A., Anglani, A. (2010). Roughness improvement in machining operations through coupled meta model and genetic algorithms technique. *International Journal of Material Forming*, vol. 3, no. 1, p. 467-470, **DOI:10.1007/s12289-010-0808-y**.

[17] Xu, F., Zhu, J.J., Wu, X., Zang, X.J., Zuo, D. W. (2010). Parameter optimization of milling Ti6Al4V using GA approach. *Key Engineering Materials*, vol. 426-427, p. 1-4, **DOI:10.4028/www.scientific.net/KEM.426-427.1**.

[18] Saffar, R.J., Razfar, M.R. (2010). Simulation of end milling operation for predicting cutting forces to minimize tool deflection by genetic algorithm. *Machining Science and Technology*, vol. 14, no. 1, p. 81-101, **DOI:10.1080/10910340903586483**.

[19] Alam, S., Nurul Amin, A.K.M., Patwari, A. U., Konneh, M. (2010). Prediction and investigation of surface response in high speed end milling of Ti-6Al-4V and optimization by genetic algorithm. *Advanced Materials Research*, vol. 83-86, p. 1009-1015, **DOI:10.4028/www.scientific.net/AMR.83-86.1009**.

[20] Li, J.G., Yao, Y.X., Gao, D., Liu, C.Q., Yuan, Z.J. (2008). Cutting parameters optimization by using particle swarm optimization (PSO). *Applied Mechanics and Materials*, vol. 10-12, p. 879-883.

[21] Pare, V., Agnihotri, G., Krishna, C.M. (2011). Optimization of cutting condition in end milling process with the approach of particle swarm optimization. *International Journal of Mechanical and Industrial Engineering*, vol. 1, no. 2, p. 2231-6477.

[22] Zubaidi, S.A., Ghani, J.A., Haron, C.H.C. (2013). Optimization of cutting conditions for end milling of Ti6Al4V alloy by using a gravitational search algorithm (GSA). *Meccanica*, vol. 48, no. 7, p. 1701-1715, **DOI:10.1007/s11012-013-9702-2**.

[23] Farahnakian, M., Razfar, M.R., Moghri, M., Asadnia, M. (2011). The selection of milling parameters by the PSO-based neural network modeling method. *The International Journal of Advanced Manufacturing Technology*, vol. 57, no. 1-4, p. 49-60, **DOI:10.1007/s00170-011-3262-1**.

[24] Huang, H., Li, A., Lin, X. (2007).Application of PSO-based wavelet neural network in tool wear monitoring. *Proceedings of the IEEE International Conference on Automation and Logistics*, p. 2813-2817, **DOI:10.1109/ICAL.2007.4339060**.

[25] Zain, A.M., Haron, H., Sharif, S. (2011). Integration of simulated annealing and genetic algorithm to estimate optimal solutions for minimizing surface roughness in end milling Ti–6AL–4V. *International Journal of Computer Integrated Manufacturing*, vol. 24, no. 6, p. 574-592, **DOI:10.1080/0951192X.2011.566629**.

[26] Baek, D.K., Ko, T.J., Kim, H.S. (2001). Optimization of feed rate in a face milling operation using a surface roughness model. *International Journal of Machine Tools & Manufacturing*, vol. 41, no. 3, p. 451-462, **DOI:10.1016/S0890-6955(00)00039-0**.

[27] Thambu, S., Marimuthu, K. (2010). Machining studies of die cast aluminium alloy-silicon carbide composites. *International*

Journal of Minerals, Metallurgy and Materials, vol. 17, no. 5, p. 648-653, **DOI:10.1007/s12613-010-0369-6**.

[28] Dweiri, F., Al-Jarrah, M., Al Wedyan, H. (2003). Fuzzy surface roughness modeling of CNC down milling of Alumin-79. *Journal of Materials Processing Technology*, vol. 133, no. 3, p. 266-275, **DOI:10.1016/S0924-0136(02)00847-6**.

[29] Fuht, K.H., Wu, C.F. (1995). A proposed statistical model for surface quality prediction in end-milling of Al alloy. *International Journal of Machine Tools and Manufacturing*, vol. 35, no. 8, p. 1187-1200, DOI:10.1016/0890-6955(95)90408-E.

[30] Kauppinen, V. (2004). High speed milling – a new manufacturing technology. *4th International DAAAM Conference on Industrial Engineering Innovation as Competitive Edge for SME*, p. 131-134.

[31] Pare, V., Agnihotri, G., Krishna, C.M. (2013). Optimization of machining parameters in high speed end milling of Al-SiC using gravitational search algorithm. *International Journal of Recent Advances in Mechanical Engineering*, vol. 2, no. 4, p. 45-51.

[32] Pare, V., Agnihotri, G., Krishna, C.M. (2013). Optimization of machining parameters in high speed end milling of Al-SiC composites using teaching learning based optimization. *Proceedings of the 2nd International Conference on Intelligent Robotics, Automation and Manufacturing*, p. 522-528.

[33] Koshy, P., Dewes, R.C., Aspinwall, D.K. (2002). High speed end milling of hardened AISI D2 tool steel (58 HRC). *Journal of Materials Processing Technology*, vol. 127, no. 2, p. 266-273, **DOI:10.1016/S0924-0136(02)00155-3**.

[34] De Souza Jr., A.M., Sales, W.F., Santos, S.C., Machado, A.R. (2005). Performance of single Si3N4 and mixed Si3N4CPCBN wiper cutting tools applied to high speed face milling of cast iron. *International Journal of Machine Tools & Manufacture*, vol. 45, no. 3, p. 335-344, **DOI:10.1016/j.ijmachtools.2004.08.006**.

[35] El-Wahab, A.I., Kishawy, H.A. (2000). A new method to improve the surface quality during CNC machining. *International Journal of Production Research*, vol. 38, no. 16, p. 3711-3723, **DOI:10.1080/00207540050175969**.

[36] Axinte, D.A., Dewes, R.C. (2002). Surface integrity of hot work tool steel after high speed milling-experimental data and empirical models. *Journal of Materials Processing Technology*, vol. 127, no. 3, p. 325-335, **DOI:10.1016/S0924-0136(02)00282-0**.

[37] Ghani, J.A., Choudhury, I.A. Hassan, H.H., (2004). Application of Taguchi method in the optimization of milling of Al alloy. Journal of Materials Processing Technology, vol. 145, no. 1, p. 84-92, **DOI:10.1016/S0924-0136(03)00865-3**.

[38] Yong, Z.P., Jun, Z., Xiuli, F., Xing, A. (2010). Optimization of surface roughness based on multi-linear regression model and genetic algorithm. *Advanced Materials Research*, vol. 97-101, p. 3050-3054, **DOI:10.4028/www.scientific.net/AMR.97-101.3050**.

Strojniški vestnik - Journal of Mechanical Engineering 61(2015)3, 187-195
DOI:10.5545/sv-jme.2014.2210
Original Scientific Paper
Received for review: 2014-09-30
Received revised form: 2014-12-16
Accepted for publication: 2015-01-06

Adaptive Fuzzy-PI Control for Active Front Steering System of Armoured Vehicles: Outer Loop Control Design for Firing On The Move System

Zulkiffli Abd Kadir*,[1,2] – Saiful Amri Mazlan[2] – Hairi Zamzuri[2] – Khisbullah Hudha[1] – Noor Hafizah Amer[1]

[1]National Defense University of Malaysia, Faculty of Engineering, Malaysia
[2]Technology University of Malaysia, Malaysia-Japan International Institute of Technology, Malaysia

An armoured vehicle tends to lose its dynamic mobility when firing on the move. This is due to the effect of the firing force that reacts at the centre of the weapon platform, which creates an unwanted yaw moment at the vehicle's centre of gravity. In order to enhance the mobility performance of the armoured vehicle, a control strategy, i.e. yaw rejection control, is designed and test on an armoured vehicle model. The purpose of the control strategy is to maintain the directional mobility of the armoured vehicle by providing a steering correction angle to the pitman arm steering system. The control strategy proposed in this study consists of two main structures: yaw rate feedback control using a Proportional-Integral-Derivative (PID) controller and Lateral Force Rejection Control (LFRC) using an adaptive Fuzzy-Proportional-Integral (adaptive Fuzzy-PI) controller. The simulation results in terms of yaw and lateral motions were observed, and the proposed control strategy was shown to successfully improve the directional mobility of the armoured vehicle after firing. The benefit of the proposed control strategy with adaptive fuzzy-PI control is evaluated by comparing its performance to fuzzy-PI and proportional-integral (PI) control strategies.
Keywords: armoured vehicle model, validation of armoured vehicle model, active front steering, firing on the move, adaptive fuzzy control, lateral force control

Highlights
- *The armoured vehicle model is developed.*
- *The armoured vehicle model was validated with a real armoured vehicle.*
- *Firing on the move control strategy is proposed.*
- *The control strategy consists of adaptive fuzzy control with lateral force control.*

0 INTRODUCTION

An online controller is used to provide a stable condition for engineering systems due to the external disturbances and uncertain inputs by automatically changing the controller parameters to satisfy the necessity of system performance. Previous studies confirmed the advantages of fuzzy controller, which has intelligent functions that can be used to predict responses through a learning process, perform optimization work and is capable of maintaining the system performance due to changing condition [1]. However, there are several problems commonly associated with fuzzy controllers. First, it is always designed without obtaining the optimum range of the membership function inputs, value of outputs and controller rules. Without an optimum set of parameters, the performance of the controller and its ability to achieve a specific desired output will be compromised. The second common problem is developing the fuzzy controller on a nonlinear model without identifying the actual system parameters. In this case, a fuzzy controller will produce insignificant output performances. Hence, the control strategy using the existing fuzzy membership function will not be able to produce the optimum performance during the initial analysis work in order to achieve the required performance levels.

Based on the abovementioned problems, a method to automatically adjust the fuzzy controller parameters is required to overcome the effect of external disturbances while dealing with parameter optimizations and nonlinear system models. The parameters known as the centre and spread of the membership function for both inputs and output values were adjusted and optimized automatically to improve the controller performance. Fuzzy controllers with optimization capabilities are often called as "adaptive fuzzy". Currently, there are some research works that have proposed adaptive fuzzy controllers for nonlinear vehicle systems. Most of the adaptive fuzzy controllers were developed to meet the desired system performance, such as improving vehicle handling and ride stabilities performance using active suspension [2] and [3], controlling vehicle slip using antilock braking system [4], monitoring the vehicle gap keeping [5], developing electrical system for electric vehicle [6] and [7] and yaw moment control for independent rear wheel drives [8]. The primary intention of the proposed adaptive fuzzy controllers

*Corr. Author's Address: National Defense University of Malaysia, Faculty of Engineering, Malaysia, zulkiffli@upnm.edu.my

was to solve the problem of selecting the range of controller parameters that can deliver the desired system performance.

In this study, a control strategy of yaw rejection system for armoured vehicle using active front steering (AFS) system is proposed. The proposed control strategy for yaw rejection is developed on a validated four-wheeled armoured vehicle model. It consists of two outer loop controllers for yaw rate feedback and lateral force feedback. The aim of designing the outer loop controllers is to reduce the magnitude of unwanted motion in the lateral direction by minimizing yaw and lateral motions due to firing force. The outer loop controllers for yaw rate feedback and lateral force feedback proposed in this study have been developed using proportional-integral-derivative (PID) control and fuzzy-PI control strategy, respectively. The proposed control strategy with adaptive fuzzy-proportional-integral (fuzzy-PI) control is then compared against the general fuzzy-PI control and the conventional proportional-integral (PI) control to evaluate the effectiveness of adaptive fuzzy-PI control.

This paper is structured as follows: the introduction and previous works on adaptive fuzzy control are explained in the first section. The second section focuses on the mathematical equations of the armoured vehicle model and is followed by validation model in the third section. The next section shows the development of the proposed control strategy with adaptive Fuzzy-PI control. The sixth section discusses the simulation results of the adaptive Fuzzy-PI control and is followed by the overall conclusion in the last section.

1 ARMOURED VEHICLE MODEL

The armoured vehicle considered in this study, as illustrated in Fig. 1, is based on a category of a movable weapon system with four wheels and can fire a projectile from the gun turret.

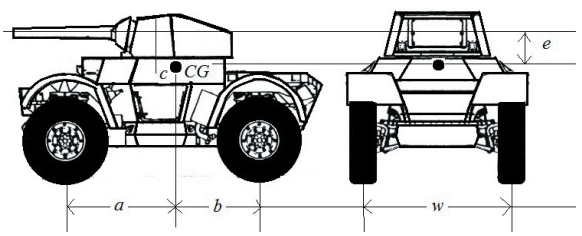

Fig. 1. *A 2D view of four wheel armoured vehicle*

The armoured vehicle covers the ride model and the handling model, which is free to pitch, roll and heave as well as allowing movements in longitudinal, lateral and yaw directions at its centre of gravity (CG).

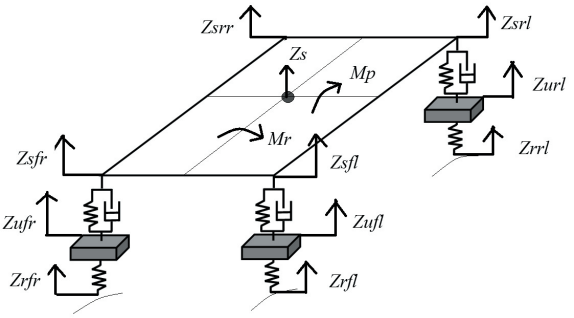

Fig. 2. *Armoured vehicle ride model*

Based on the armoured vehicle ride model shown in Fig. 2, the dynamics behaviour of the armoured vehicle in terms of pitch, roll, and heave motions are derived mathematically using equations of motions from Newton's second law as follows:

$$I_p\ddot{\theta} = (F_{srl} + F_{drl} + F_{srr} + F_{drr})b - \\ -(F_{sfl} + F_{dfl} + F_{sfr} + F_{dfr})a + m_s a_x h_{CG}, \quad (1)$$

$$I_r\ddot{\varphi} = \left(F_{sfr} + F_{srr} + F_{dfr} + F_{drr}\right)\frac{w}{2} - \\ -\left(F_{sfl} + F_{srl} + F_{dfl} + F_{drl}\right)\frac{w}{2} + m_s a_y h_{CG}, \quad (2)$$

$$m_s\ddot{Z}_s = F_{sfl} + F_{dfl} + F_{sfr} + F_{dfr} + F_{srl} + F_{drl} + F_{srr} + F_{drr}, \quad (3)$$

where $\ddot{\varphi}$ is the angular acceleration of roll at body *CG* [rad/s²], I_r is the moment inertia of roll axis [kg/m²], h_{CG} is the distance between roll axis and *CG* [m], w is the vehicle track width [m], a_y is lateral acceleration [m/s²], $\ddot{\theta}$ is the angular acceleration of pitch at body *CG* [rad/s²], I_p is the moment inertia of pitch axis [kg/m²], a is distance from the front tyre to the body *CG* [m], b is distance from the rear tyre to the body *CG* [m], a_x is longitudinal acceleration [m/s²], m_s is the armoured vehicle's mass [kg], $\ddot{Z}_s$ is the vertical acceleration of sprung mass at *CG* [m/s²], F_{sij} is suspension force [N] and F_{dij} is damper force [N].

Fig. 3 illustrates the armoured vehicle handling model. The longitudinal and lateral accelerations can be obtained by considering the forces acting on each tyre in the longitudinal direction, *x*-axis and longitudinal direction, *y*-axis as follows:

$$F_{xrr} + F_{xrl} - F_{yfr}\sin\delta + F_{xfr}\cos\delta - \\ -F_{yfl}\sin\delta + F_{xfl}\cos\delta - F_e\cos\beta = m_s a_x, \quad (4)$$

$$F_{yrr} + F_{yrl} + F_{xfr}\sin\delta + F_{yfr}\cos\delta + \\ + F_{xfl}\sin\delta + F_{yfl}\cos\delta + F_e\sin\beta = m_s a_y, \quad (5)$$

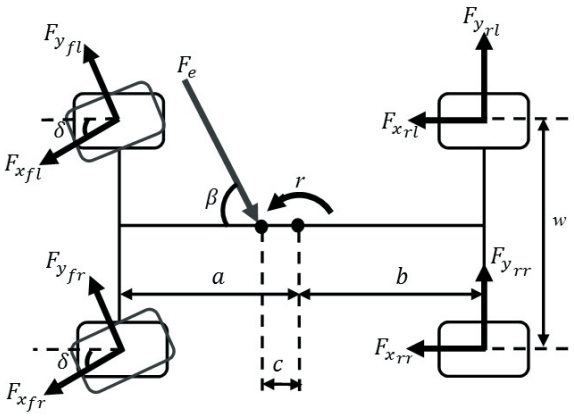

Fig. 3. *Armoured vehicle handling model with firing disturbance*

The yaw angular acceleration acting on the armoured vehicle handling model is also based on the effects of tyre forces, i.e. lateral force and longitudinal force, and it can be derived as:

$$\left(\begin{array}{l} -\frac{w}{2}F_{xfr}\cos' + \frac{w}{2}F_{xfl}\cos\delta - \frac{w}{2}F_{xrr} + \\ +\frac{w}{2}F_{xrl} + \frac{w}{2}F_{yfl}\sin' - \frac{w}{2}F_{yfr}\sin' - \\ -bF_{yrl} - bF_{yrr} + aF_{yfl}\cos' + aF_{yfr}\cos' - \\ -aF_{xfl}\sin' - aF_{xfr}\sin' + cF_e\sin\beta \end{array}\right) = I_z\ddot{r}, \quad (6)$$

where I_z is the moment of inertia around z-axis [kg/m^2], δ is the tyre steer angle [rad], $\ddot{r}$ is yaw angular acceleration [rad/s^2] and m_s is the armoured vehicle's mass [kg].

2 VALIDATION OF ARMOURED VEHICLE MODEL

In order to validate the armoured vehicle model, a handling test was conducted using a Ferret Scout Car armoured vehicle. Several transducers were installed in the armoured vehicle to observe the vehicle's behaviour such as lateral acceleration, roll angle, yaw rate and steering input from the driver, as shown in Fig. 4. Validation of the developed armoured vehicle model can be defined as an assessment and comparison of the developed model's behaviours with the actual armoured vehicle's behaviours [9]. The validation of the armoured vehicle model is done by comparing the behaviour obtained from the simulation model with the actual responses obtained from the experimental armoured vehicle using similar handling test. The experimental results were also used to optimize the parameters of the developed armoured vehicle model.

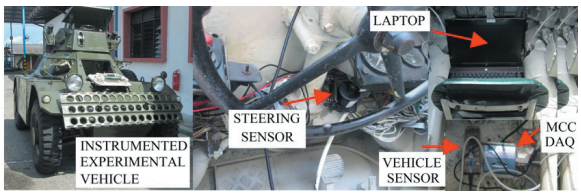

Fig. 4. *Instrumented experimental armored vehicle*

The model validation is performed for a double lane change test. However, due to several constraints, such as limitation of the experimental area and the speed of the Ferret Scout Car, the experimental work is performed with speed of 40 km/h. Fig. 5 shows the steering input delivered by the driver in double lane change test.

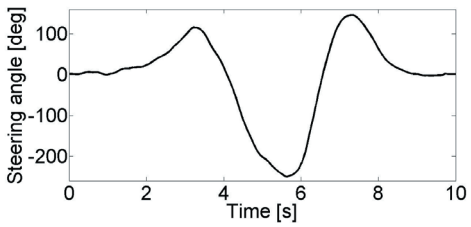

Fig. 5. *Steering wheel angle*

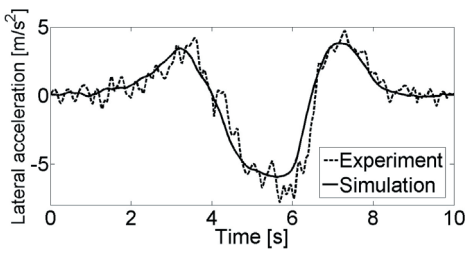

Fig. 6. *Lateral acceleration response*

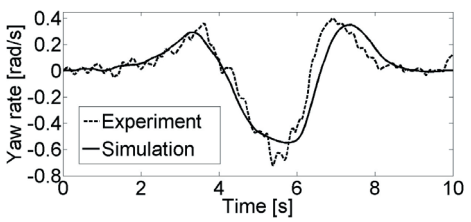

Fig. 7. *Yaw rate response*

The validation results for the double lane change test are analysed in terms of lateral acceleration, yaw rate and roll angle of the armoured vehicle. The results are shown in Fig. 6 to 8, respectively. It can be seen that simulation model has similar trends and magnitudes with the actual manoeuvring of the armoured vehicle. The small deviations in the

validation results were caused by the error from the driver in maintaining a constant speed for the actual handling test. For the overall validation results, it is clear that the behaviours obtained from the simulation work and the experimental work for the double lane change test have similar responses with acceptable rates of error. The validated armoured vehicle model is then used to develop a yaw cancellation system using active front steering in the next section.

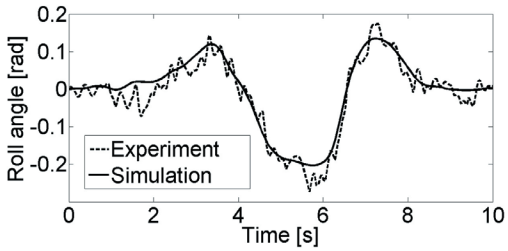

Fig. 8. *Roll angle response*

3 THE PROPOSED CONTROL STRATEGY OF AFS FOR ARMOURED VEHICLEs

The AFS for four-wheeled armoured vehicles is developed by installing an additional mechanism consisting of a direct current (DC) motor, known as an AFS actuator as well as AFS gearbox, as illustrated in Fig. 9.

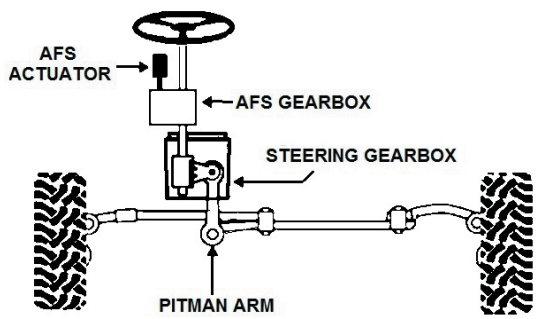

Fig. 9. *Configuration of active front steering using pitman steering*

This mechanism is installed in the conventional Pitman arm steering system by maintaining the existing parts, including the steering wheel, steering column, recirculating ball gearbox, pitman arm and steering linkage. The AFS gearbox is used to superimpose the steering wheel angle obtained from the driver and angle of steering correction from the AFS actuator. In AFS, there are two angles need to be evaluated: the steering wheel input given by the driver and the steering correction angle generated by the AFS actuator. The combination of both angles provides a correction angle to the front wheels through the Pitman arm joint.

In this study, an additional controller loop is introduced as lateral force rejection control (LFRC). The purposed of LFRC loop is used to measure the estimated lateral force (F_{ye}) in order to eliminate the unwanted lateral motion due to the firing impact. The LFRC is adopted from the principle of skyhook control usually used in suspension control, the main purpose of which is to improve the vertical behaviour of the vehicle subjected to road disturbances **[10]** and **[11]**. Using the same concept, skyhook control principle was applied in LFRC to reduce unwanted disturbances in lateral direction. The configuration of the estimated lateral force is shown in Fig. 10, which consists of an imaginary lateral damper ($C_{lateral}$) to provide virtual damping for the system and an imaginary lateral wall as the reference point.

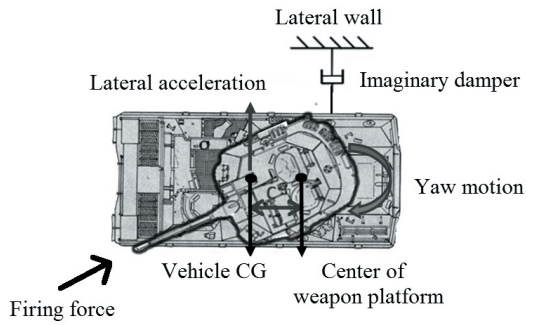

Fig. 10. *Armored vehicle with imaginary lateral wall and imaginary lateral damper*

The estimated lateral force (F_{ye}) is defined as:

$$F_{ye} = C_{lateral}\dot{y}_{GC}. \tag{7}$$

Here, $\dot{y}_{GC}$ is known as the lateral velocity of the armoured vehicle. This can be obtained by differentiating the global coordinate of lateral displacement (y_{GC}) of the armoured vehicle. The lateral displacement of y_{GC} is defined as:

$$y_{GC} = y_o + \int v_y \cos r + v_x \sin r, \tag{8}$$

where y_o is the local lateral displacement [m], r is the armoured vehicle's yaw angle [rad], v_x the armoured vehicle's longitudinal velocity [m/s], and v_y the armoured vehicle's lateral velocity [m/s].

The proposed AFS control strategy is designed using a four-wheel armoured vehicle model as shown in Fig. 11. The system is developed by assuming that the armoured vehicle travels in the longitudinal direction without any steering input from the driver.

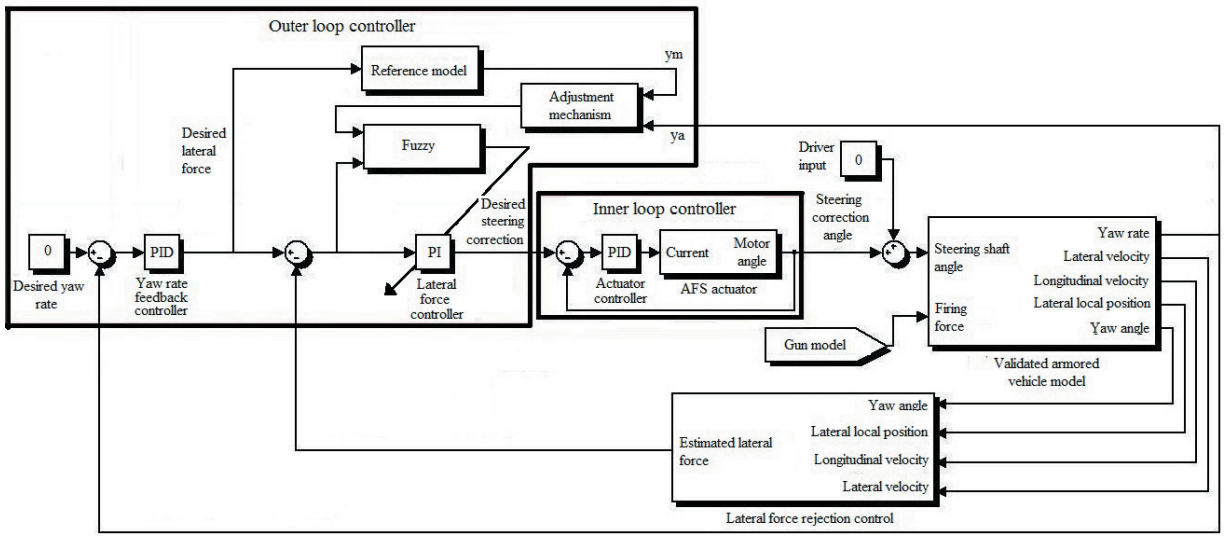

Fig. 11. *Control strategy of AFS for armored vehicle*

This control strategy consists of two feedback loop controllers, which are inner and outer loop controls. The inner loop controller is developed to control the AFS actuator while the outer loop controller is to control the overall dynamic performance of the armoured vehicle during firing. In the outer loop controller, both the yaw rate and lateral force controller feedback are used to reject the unwanted yaw motion while simultaneously minimizing the lateral movement of the armoured vehicle subjected to firing impact.

A conventional PID controller is used as the yaw rate feedback controller in order to estimate the yaw rate error of the armoured vehicle. This error is used as the reference point for the following controller loop, known as the lateral force control. This lateral force control is monitored by a self-tuning PI control adapted by a nonlinear fuzzy membership function. Henceforth, the desired lateral force (F_{yd}) is defined as:

$$F_{yd} = (K_{py} + \frac{K_{iy}}{s} + K_{dy}s)(y_d - y_a), \tag{9}$$

where y_a is actual yaw rate, y_d is desired yaw rate, while K_{py}, K_{iy}/S and $K_{dy}s$ are vehicle controllers for yaw rate response. F_{yd} is compared with the estimated lateral force (F_{ye}) in order to measure the desired angle of steering correction (δ_d). The steering correction is used to counterback the steering wheel angle due to the firing disturbance acting at the centre of weapon platform. Therefore, the δ_d is measured as below:

$$\delta_d = (K_{pl} + \frac{K_{il}}{s})(F_{yd} - F_{ye}), \tag{10}$$

where K_{pl} and K_{il}/S are proportional and integral gains for lateral force control, respectively. Initially, the gain values of proportional and integral are set to be a constant values throughout the simulation procedure. However, these constant values are not compatible once the conditions or disturbances vary with time. Hence, a self-tuning method is required in order to tune the constant values according to the disturbance or condition. The self-tuning method can be implemented for both proportional and integral gains by identifying the maximum and minimum gain values through the simulation procedure. The range of the proportional and integral gains are $K_{pl} \in [1.5, 0.1]$ and $K_{il} \in [0.08, 0.01]$. The range of each gains can be used to calibrate K'_{pl} and K'_{il} as follows:

$$K'_{pl} = \frac{K_{pl} - K_{pl\min}}{K_{pl\max} - K_{pl\min}} = \frac{K_{pl} - 0.1}{1.5 - 0.1}, \tag{11}$$

$$K'_{il} = \frac{K_{il} - K_{il\min}}{K_{il\max} - K_{il\min}} = \frac{K_{il} - 0.01}{0.08 - 0.01}, \tag{12}$$

where K'_{pl} and K'_{il} are the update values for K_{pl} and K_{il}. Both equations can be rearranged as $K_{pl}=1.4K'_{pl}+0.1$ and $K_{il}=0.07K'_{il}+0.01$. Although the self-tuning PI control is used in this control strategy, the performance of the armoured vehicle due to firing needs more improvement in term of lateral displacement and the stability of the armoured

vehicle. Hence, a nonlinear fuzzy control is merged with a self-tuning PI controller. The combination of a self-tuning Fuzzy-PI controller is used to increase the dynamic performance of the armoured vehicle during firing. The equations of the nonlinear fuzzy control are described as follows:

$$y_p = f(x\,|\,\theta) = \frac{\Sigma_{i=1}^{r} b_i \Pi_{j=1}^{n} \exp\left(-\frac{1}{2}\left(\frac{x_j - c_j^i}{\sigma_j^i} \right)^2 \right)}{\Sigma_{i=1}^{r} \Pi_{j=1}^{n} \exp\left(-\frac{1}{2}\left(\frac{x_j - c_j^i}{\sigma_j^i} \right)^2 \right)}, \quad (13)$$

where, x_j is input to the fuzzy set, $j=1,\ldots,n$ (n is number of inputs) and $i=1,\ldots,r$ (r is the number of rules). The parameter b_i is the output values of the fuzzy set, while c_j^i and σ_j^i are centre and spread of Gaussian membership function inputs, respectively. However, the parameters of the fuzzy control itself need to be configured varying with time since there are several constant parameters which are b, c and σ. Therefore, an adaption law is absorbed in the self-tuning Fuzzy-PI controller in order to enhance the performance of the AFS control strategy. The adaptation law is developed based on an adjustment mechanism to update the constant parameters of the fuzzy controller. The adjustment mechanism for the fuzzy controller is developed using first order reference model as shown in Fig. 11. The intention of the adjustment mechanism is to vary the fuzzy controller parameters, i.e. b, c and σ. The yaw rate (y_a) response is considered in designing the adjustment mechanism of the fuzzy control. It is assumed that output from fuzzy control $f(x|\theta)$ is similar with the yaw rate response, and error (e_m) for the adjustment mechanism can be written as:

$$e_m = \frac{1}{2}(y_a - y_m)^2 = \frac{1}{2}(f(x\,|\,\theta) - y_m)^2, \quad (14)$$

e_m is designed to minimize error between the reference model (y_m) and yaw rate response (y_a). By considering the number of rules (r), the parameters of input c, σ and the output parameter b can be adjusted by updating the parameter values using gradient descent method as follows:

$$b_i(k+1) = b_i(k) - \lambda_1 \frac{\partial e_m}{\partial b_i}, \quad (15)$$

$$c_i(k+1) = c_i(k) - \lambda_2 \frac{\partial e_m}{\partial c_i}, \quad (16)$$

$$\sigma_i(k+1) = \sigma_i(k) - \lambda_3 \frac{\partial e_m}{\partial \sigma_i}, \quad (17)$$

where, update parameter values λ_1, λ_2 and λ_3 need to be fine tuned. The first derivative of adjustment error (e_m) with respect to fuzzy parameters b, c and σ are written as follows:

$$b_i(k+1) = b_i(k) - \lambda_1 (f(x\,|\,\theta) - y_m)\frac{z^i}{w}, \quad (18)$$

$$c_i(k+1) = c_i(k) - \lambda_2 [f(x\,|\,\theta) - y_m][b_i(k) - f(x^m\,|\,\theta(k))]\left[\frac{x_j^m - c_j^i(k)}{(\sigma_j^i(k))^2} \right]\frac{z^i}{w}, \quad (19)$$

$$\sigma_i(k+1) = \sigma_i(k) - \lambda_3 [f(x\,|\,\theta) - y_m][b_i(k) - f(x^m\,|\,\theta(k))]\left[\frac{(x_j^m - c_j^i(k))^2}{(\sigma_j^i(k))^3} \right]\frac{z^i}{w}, \quad (20)$$

where,

$$z^i = \prod_{j=1}^{n} \exp\left(-\frac{1}{2}\left(\frac{x_j^m - c_j^i}{\sigma_j^i} \right)^2 \right), \quad (21)$$

and

$$w = \sum_{i=1}^{r} z^i. \quad (22)$$

4 PERFORMANCE ASSESSMENT OF THE ADAPTIVE FUZZY-PI CONTROL FOR ARMOURED VEHICLE USING ACTIVE FRONT STEERING

The performance of proposed control strategy is analysed for a duration of 2.5 seconds. The control parameters of PI control, parameters of the armoured vehicle model, membership functions of Fuzzy-PI, input rules of Fuzzy-PI control output rules of fuzzy-PI control and control parameters of adaptive fuzzy-PI control are presented in Tables 1 and 2, Fig. 12 and Tables 3 to 5, respectively.

Table 1. *Controller parameters for control strategy with PI control*

Yaw Rate Controller	$K_{py} = 40$	$K_{iy} = 4$	$K_{dy} = 3$
Lateral Force Controller	$K_{pl} = 1.5$	$K_{il} = 0.08$	-

The cumulative Gaussian for error and error rate membership functions are set as negative big (NB), negative small (NS), zero (ZE), positive small (PS) and positive big (PB). Meanwhile, the output values

to update the PI control are set as big (B), medium big (MB), medium (M), medium small (MS) and small (S).

Table 2. *Armoured vehicle model parameters*

Armoured vehicle mass, m_s [kg]	4000
Distance front tyre to the body CG, a [m]	1
Distance rear tyre to the body CG, b [m]	1.3
Distance from roll axis to CG, h_{CG} [m]	0.5
Moment of inertia around z-axis, I_z [kg/m²]	5000
Moment inertia of roll axis, I_r [kg/m²]	500
Damping stiffness at front left, front right, rear left, rear right, K_{sfl}, K_{sfr}, K_{srl}, K_{srr} [N/m]	10000
Damping stiffness at front left, front right, rear left, rear right, C_{sfl}, C_{sfr}, C_{srl}, C_{srr} [N/ms^{-1}]	800
Track width, w [m]	1.5

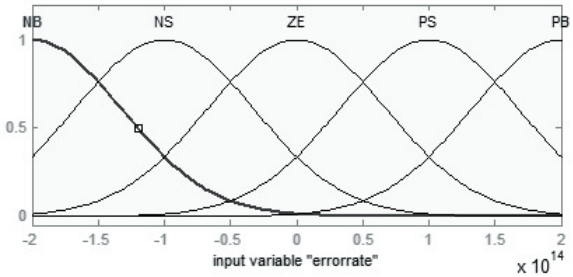

a) Error membership function

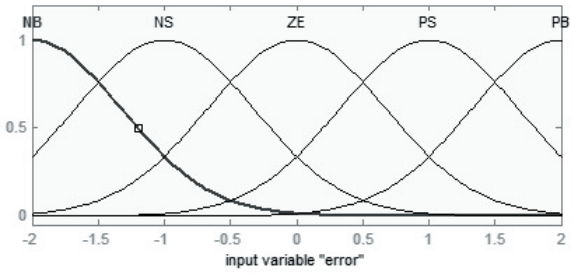

b) Error rate membership function

Fig. 12. *Membership functions of Fuzzy-PI control for error rate and error*

Table 3. *Fuzzy rules for control strategy with Fuzzy-PI control*

Error Rate/Error	NB	NS	ZE	PS	PB
NB	S	S	MS	MS	M
NS	S	MS	MS	M	MB
ZE	MS	MS	M	MB	MB
PS	MS	M	MB	MB	B
PB	M	MB	MB	B	B

Table 4. *Fuzzy output values for control strategy with Fuzzy-PI control*

Update value for PI control	S	MS	M	MB	B
K'_{pl}	0.1	0.75	1.5	2.25	3
K'_{il}	0.01	0.04	0.08	0.12	0.16

Table 5. *Controller parameters for control strategy with adaptive Fuzzy-PI control*

Update parameter	Value
λ_1	-30
λ_2	4000
λ_3	10000

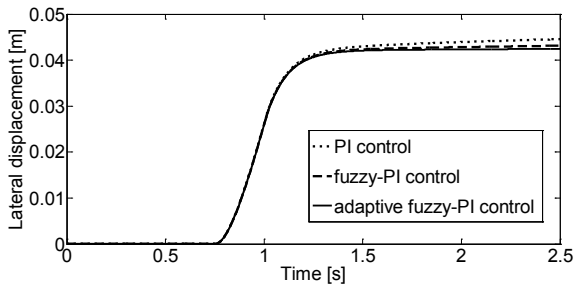

a) Firing angle of 30 degrees

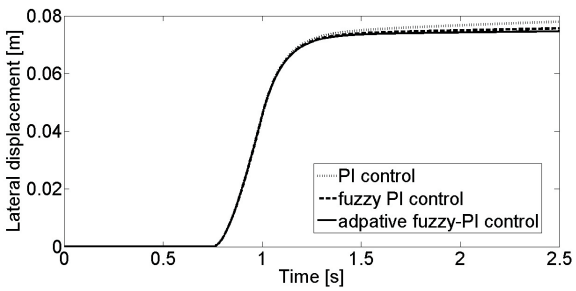

b) Firing angle of 60 degrees

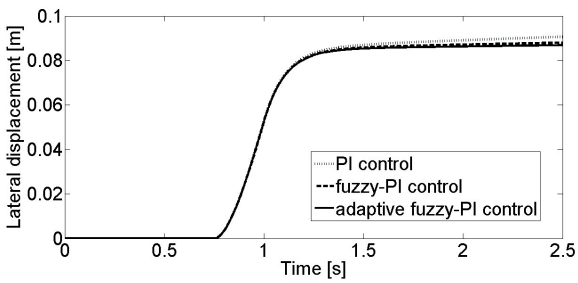

c) Firing angle of 90 degrees

Fig. 13. *Lateral displacement responses for various firing angles*

Simulation results of armoured vehicle body displacement in lateral motion are shown in Fig. 13. The firing angles of the armoured vehicle are set at 30, 60 and 90 degrees with a constant cruising speed of 40 km/h. The effectiveness of the adaptive Fuzzy-

PI control strategy can be evaluated from the lateral displacement error of the armoured vehicle after the firing condition. The control strategy with adaptive Fuzzy-PI control managed to reduce the magnitude of lateral displacement error and maintain the direction of travel after firing, in comparison to its counterparts, i.e. Fuzzy-PI and PI controls. The controller's ability to improve the dynamics performance in lateral direction will ensure better mobility for the armoured vehicle when firing on the move.

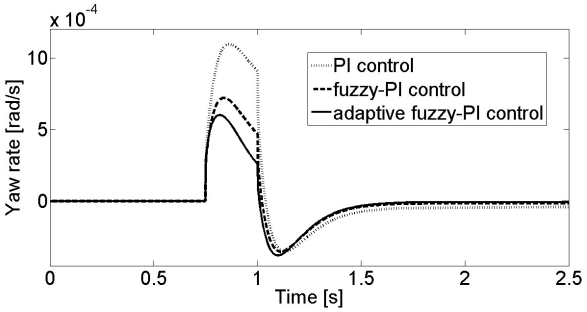

a) Firing angle of 30 degrees

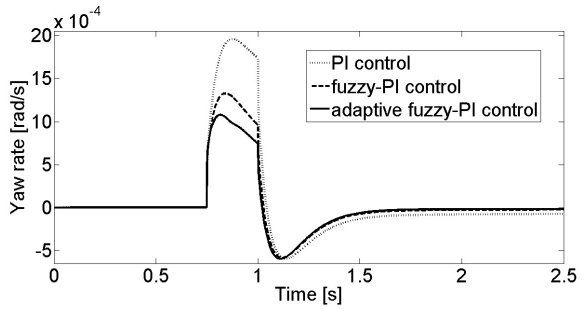

b) Firing angle of 60 degrees

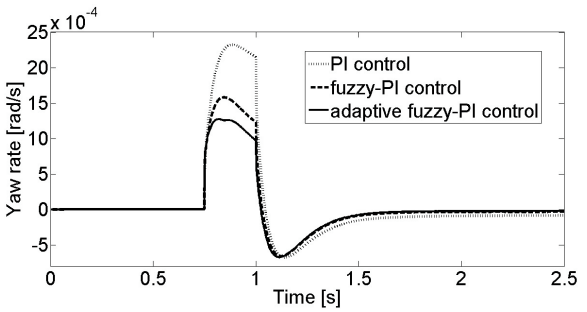

c) Firing angle of 90 degrees

Fig. 14. *Yaw rate responses for various firing angles*

Similar performance also can be observed in the yaw rate and yaw angle, as shown in Figs. 14 and 15, respectively. In both cases, the control strategy with the adaptive Fuzzy-PI control shows better performance in minimizing both the settling time and the response magnitude in comparison to the control strategy with Fuzzy-PI and PI controls. For the yaw rate response in Fig. 14, it can be observed that the control strategy with adaptive Fuzzy-PI control has been successful in minimizing the yaw rate magnitude as compared to its counterparts. The control strategy with the adaptive Fuzzy-PI control also managed to isolate armoured vehicle body from the unwanted yaw rate almost 20 % more than the Fuzzy-PI control for all firing angles. By isolating the unwanted yaw rate from the armoured vehicle body, the dynamics stability of the armoured vehicle during firing on the move can be improved. This will improve the vehicle's ability to move at the intended direction when firing. Furthermore, the probability of the armoured vehicle becoming unstable can be minimized.

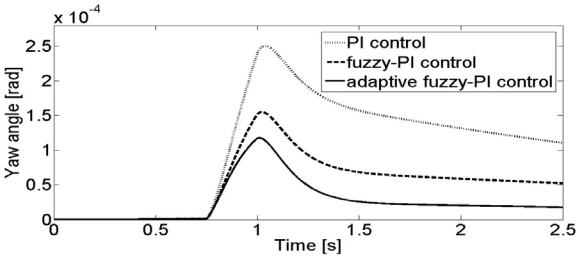

a) Firing angle of 30 degrees

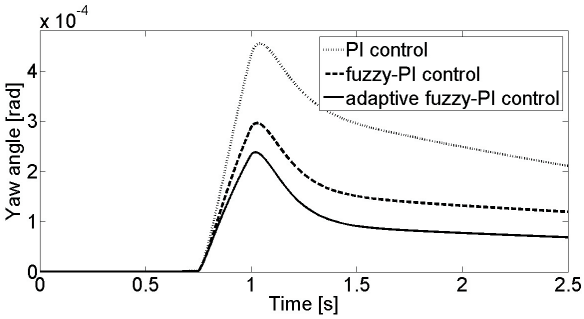

b) Firing angle of 60 degrees

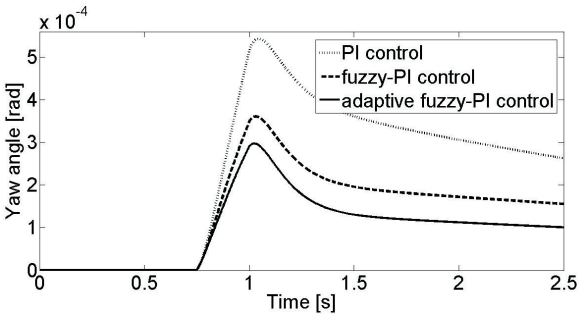

c) Firing angle of 90 degrees

Fig. 15. *Yaw angle responses for various firing angles*

Similarly, the control strategy with the adaptive Fuzzy-PI control demonstrates a significant reduction on yaw angle response at body centre of gravity on firing test with angles of 30, 60 and 90 degrees

compared to Fuzzy-PI and PI controls, as shown in Fig. 15. From the simulation results, it is evident that the adaptive Fuzzy-PI control is very effective in minimizing the yaw angle error. The yaw angle response for all firing tests is summarized in Table 6. By minimizing the yaw angle error, directional stability of armoured vehicle during firing while moving can be improved, which is the major aspect of armoured vehicle safety.

Table 6. *Yaw angle responses for firing angle of 30, 60 and 90 degrees*

Firing angle [°]	Yaw angle response		
	PI [rad]	Fuzzy-PI [rad]	Adaptive fuzzy-PI [rad]
30	2.5×10^{-4}	1.5×10^{-4}	1.1×10^{-4}
60	4.6×10^{-4}	2.9×10^{-4}	2.2×10^{-4}
90	5.4×10^{-4}	3.6×10^{-4}	2.9×10^{-4}

5 CONCLUSION

A control strategy for an armoured vehicle using AFS system has been developed on a validated model of a four-wheel armoured vehicle using MATLAB-SIMULINK. The main purpose of this proposed control strategy is to enhance the dynamic performance of the armoured vehicle, such as lateral displacement, yaw rate and yaw angle when firing on the move. There are two feedback controllers used in this study: yaw rate feedback using PID control and lateral force feedback using adaptive Fuzzy-PI control. The proposed AFS control strategy is then evaluated via simulation involving various firing angles of 30, 60 and 90 degrees. Based on the simulation results, it can be observed that the proposed AFS control strategy using the adaptive Fuzzy-PI controller performed significantly better in comparison to the Fuzzy-PI and conventional PI control strategy. This improvement of the armoured vehicle due to lateral and yaw performances can increase the stability of the armoured vehicle after the firing impact. Furthermore, the soldiers driving the armoured vehicle are able to control the vehicle even after the firing impact from the gun.

6 ACKNOWLEDGMENT

The authors would like to thank the Malaysian Ministry of Education through RAGS (RAGS/2012/UPNM/TK01/4), LRGS (LRGS/B-U/2013/UPNM/DEFENCE & SECURITY-P1), Institut Kejuruteraan Tentera Darat (IJED) and the Malaysia-Japan International Institute of Technology (MJIIT) for their financial support and the use of their research facility for this research.

7 REFERENCES

[1] Sa-ngawong, N., Ngamroo, I. (2015). Intelligent photovoltaic farms for robust frequency stabilization in multi-area interconnected power system based on PSO-based optimal Sugeno fuzzy logic control. *Renewable Energy,* vol. 74, p. 555–567, **DOI:10.1016/j.renene.2014.08.057**.

[2] Chiou J.S., Tsai, S.H., Liu, M.T. (2012). A PSO-based adaptive fuzzy PID-controllers. *Simulation Modelling Practice and Theory*, vol. 26, p. 49-59, **DOI:10.1016/j.simpat. 2012.04.001**.

[3] Mailah, M., Priyandoko, G. (2007). Simulation of a suspension system with adaptive fuzzy active force control. *International Journal of Simulation Modelling*, vol. 6, no. 1, p. 25-36, **DOI:10.2507/IJSIMM06(1)3.079**.

[4] Wang, W.Y., Li, I.H., Tsai, C.P., Su, S.F., Hsu, S.B. (2009). Dynamic Slip-Ratio Estimation and Control of Antilock Braking Systems Using an Observer-Based Direct Adaptive Fuzzy–Neural Controller. *IEEE Transactions on Industrial Electronics*, vol. 56, no. 5, p. 1746-1756, **DOI:10.1109/TIE.2008.2009439**.

[5] Naranjo, J.E., Gonzalez, C., Reviejo, J., Garcia, R., de Pedro, T. (2003). Systems adaptive fuzzy control for inter-vehicle gap keeping. *IEEE Transactions on Intelligent Transportation Systems*, vol. 4, no. 3, p. 132-142, **DOI:10.1109/TITS.2003.821294**.

[6] Shen, W.X., Chan, C.C., Lo, E.W.C., Chau, K.T. (2002). Adaptive neuro-fuzzy modeling of battery residual capacity for electric vehicles. *IEEE Transactions on Industrial Electronics*, vol. 49, no. 3, p. 677-684, **DOI:10.1109/TIE.2002.1005395**.

[7] Chau, K.T., Wu, K.C., Chan, C.C. (2004). A new battery capacity indicator for lithium-ion battery powered electric vehicles using adaptive neuro-fuzzy inference system. *Energy Conversion and Management*, vol. 45, no. 11-12, p. 1681-1692, **DOI:10.1016/j. enconman.2003.09.031**.

[8] Niasar, A.H., Moghbeli, H., Kazemi, R. (2003). Yaw moment control via emotional Adaptive Neuro-Fuzzy Controller for independent rear wheel drives of an electric vehicle. *Proceedings of 2003 IEEE Conference on Control Applications*, vol. 1, p. 380-385.

[9] Kadir, Z.A., Hudha, K., Ahmad, F., Abdullah, M.F., Norwazan, A.R., Mohd Fazli, M.Y., Khalid, A.J., Gunasilan, M. (2012). Verification of 14DOF full vehicle model based on steering wheel input. *Applied Mechanics and Materials*, vol. 165, p. 109-113, **DOI:10.4028/www.scientific.net/AMM. 165.109**.

[10] Harun, M.H., Abdullah,W., Jamaluddin, H., Rahman, R.A. Hudha, K. (2014). Hybrid skyhook-stability augmentation system for ride quality improvement of railway vehicle. *Applied Mechanics and Materials*, vol. 663, p. 141-145, **DOI:10.4028/www.scientific.net/ AMM.663.141**.

[11] Crews, J.H., Mattson, M.G., Buckner, G.D. (2011). Multi-objective control optimization for semi-active vehicle suspensions. *Journal of Sound and Vibration*, vol. 330, no. 23, p. 5502-5516, **DOI:10.1016/j.jsv.2011.05.036**.

Strojniški vestnik - Journal of Mechanical Engineering 61(2015)3, 196-206

DOI:10.5545/sv-jme.2014.2138
Original Scientific Paper
Received for review: 2014-08-24
Received revised form: 2014-10-26
Accepted for publication: 2014-11-03

Study of an Energy Regeneration System with Accumulator for Hydraulic Impulse Testing Equipment

Zaipeng Man* – Fan Ding – Chuan Ding – Shuo Liu
Zhejiang University, The State Key Lab of Fluid Power Transmission and Control, China

To guarantee the reliability and performance of hydraulic systems, it is of vital importance to do hydraulic impulse testing for hydraulic components. However, the testing time is usually so long that the energy consumption is very large. An energy regeneration system with an accumulator is proposed and used for hydraulic impulse testing equipment. Mathematical analysis and simulations show that the hydraulic impulse testing system with an accumulator can reduce energy consumption by 15% compared with that of the system without an accumulator in the cycle. Furthermore, the energy efficiency of the hydraulic impulse testing system is increased from 62.82 to 75.71% by the use of an accumulator. Both simulation results and experimental results show that the control performance of the hydraulic impulse testing equipment with an accumulator is better than that of the equipment without an accumulator, and has a faster response speed and a larger pressure rise rate.

Keywords: hydraulic impulse testing, energy regeneration, hydraulic accumulator, simulation, experiment, energy storage

Highlights

- *Proposed energy regeneration system with accumulator.*
- *Energy regeneration system used for hydraulic impulse testing.*
- *Mathematical and simulation models built for the system.*
- *Effects on energy consumption and system efficiency studied.*
- *Better control performance proved by simulation and experiment results.*

0 INTRODUCTION

Hydraulic transmission systems are widely used in construction and agricultural machinery owing to their high power density, high compactness, and flexible control [1]. However, with fuel prices increasing and an energy crisis looming, the large energy consumption of hydraulic systems is drawing more and more attention [2]. In order to improve the efficiency of hydraulic transmission systems and reduce energy consumption, many methods have been put forward. It is claimed that an energy-saving hydraulic system should be able to recover energy during deceleration or while a load is lowered [3]. Various energy-saving hydraulic systems have been studied, such as secondary control systems and constant pressure systems [4] to [6]. An energy regeneration system in hydraulic forklift trucks has been studied, concentrating on energy recovery in the main lift system with electric motor and batteries, and resulting in improved energy efficiency but shorter lifetime of components [7]. An energy recovery system with a hydraulic accumulator that could save and restore energy in a crane's hydraulic system has also been studied, and it was found that the potential energy of the crane and load can be saved in the form of hydraulic energy and reutilized [8]. A speed control system of a variable voltage variable frequency hydraulic elevator with a pressure accumulator was studied, and was shown to have higher efficiency compared with a hydraulic elevator without a pressure accumulator [9]. A new hydraulic closed-loop hydrostatic transmission energy-saving system has been proposed, and results indicate that the efficiency can be improved by using a hydraulic accumulator [3]. The energy regeneration systems for hybrid hydraulic excavators have also been studied, and it was found that an estimated 41% of the total potential energy could be regenerated at the lowering of the boom [10].

On the other hand, it is widely recognized that many hydraulic system accidents and component failures are caused by hydraulic impulse rather than overload [11]. So it is of vital importance to do hydraulic impulse testing for hydraulic components, including hydraulic hoses, fittings, assemblies, and so on. Although energy recovery applications are widely used in industry, few energy recovery systems have been developed for hydraulic impulse testing equipment. According to the relevant standards, impulse testing time may be up to 280 hours, which uses a lot of energy [12] to [15]. So it is of great importance to reduce energy consumption during impulse testing. The SAE proposed a standard for impulse machine equipment and operation, which has become the reference for most of later impulse testing equipment [16]. A new hydraulic intensifier

*Corr. Author's Address: The State Key Lab of Fluid Power Transmission and Control, Zhejiang University, Hangzhou, China. manzaipeng@126.com

has been proposed, which can be used for hydraulic impulse testing [17]. The ramp-output response of hydraulic impulse testing equipment and parameter adjustment for a standard pulse has been studied, and good performance of the system has been achieved [18]. All of these above mentioned systems can achieve the desired pressure curves. However, high energy consumption and energy waste are the main drawbacks.

As the hydraulic accumulator can store and release energy over a short period of time, it is a good choice for energy regeneration in hydraulic impulse testing equipment, since the cycle time of hydraulic impulse testing is generally very short.

In this paper, an energy regeneration system with a hydraulic accumulator is used for hydraulic impulse testing. The energy consumption and system efficiencies of the hydraulic impulse testing equipment with an accumulator are compared with those of hydraulic impulse testing equipment without an accumulator using mathematical analysis and simulations. The results show that the energy regeneration system can reduce energy consumption by 15 % and increase system efficiency from 62.82 to 75.71 %. Experiments have been carried out to study the control performance of the energy regeneration system for hydraulic impulse testing equipment with an accumulator, and the results show that a faster response speed and a larger pressure rise rate can be obtained.

1 SYSTEM DESCRIPTION

A schematic diagram of the energy regeneration system with hydraulic accumulator for hydraulic impulse testing equipment is shown in Fig. 1. It mainly consists of the pressure source, servo valve, pressure-boost cylinder, accumulator, check valve, and test components. The pressure source, including a variable displacement pump, a check valve, a relief valve, and an accumulator, is used to provide hydraulic power for the system. Since some hydraulic components need to be tested under high pressure, a pressure-boost cylinder is utilized to achieve a pressure higher than that of the pressure source. The pressure-boost cylinder is designed to work in a differential mode, under the control of the three-way servo valve. The cylinder mainly consists of four chambers, in particular, the control chamber connected to the servo valve, system-pressure-chamber connected to the pressure source, the boost chamber connected to the test components, and the accumulator chamber connected to the accumulator. The test components can be hydraulic hoses, fittings, assemblies and so on. A check valve is used to supplement hydraulic oil for the test components.

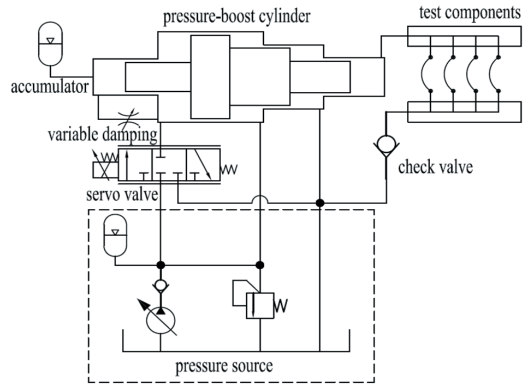

Fig. 1. *Energy regeneration system for hydraulic impulse testing equipment*

It should be noted that there are two accumulators in Fig. 1. One is connected to the accumulator chamber of the pressure-boost cylinder, the other is connected to the pump in the pressure source. Bladder accumulators are adopted due to their rapid response, long service life, and small dimensions. Both of them are helpful in reducing the energy consumption of the system. However, the accumulator connected to the pump is mainly used for absorbing pulsation of the pressure source, and is not the focus of this paper. Therefore, the accumulator referred to hereafter is the one connected to the accumulator chamber of the pressure-boost cylinder.

For simplicity of analysis, the motion of the piston of the cylinder is divided into two strokes. When a positive signal is provided for the servo valve, the piston of the hydraulic cylinder moves to the right, so the hydraulic oil in the test components is compressed and correspondingly the pressure rises, which is defined as the boost stroke. In contrast, when a negative signal is provided for the servo valve, the piston of the hydraulic cylinder moves to the left, so the hydraulic oil in the test components is released and correspondingly the pressure decreases, which is defined as the return stroke.

The key component of the energy regeneration system is the accumulator attached to the accumulator chamber of the pressure-boost cylinder. A variable damping is designed, in a mechanical structure way, between the accumulator chamber and the control chamber of the cylinder, as shown in Fig. 1. At the end stage of the boost stroke, the variable damping is so small that the accumulator may be considered as directly connected to the control chamber. Hydraulic

oil can be provided by the pressure source through the servo valve. Then in the return stroke, the variable damping becomes larger. At the end of the return stroke, the damping is so large that the accumulator may be considered as isolated from the control chamber. Correspondingly, the gas in the accumulator is compressed, and the hydraulic energy in the test components and from the pressure source is recovered by the accumulator. In the next boost stroke, the energy stored in the accumulator can be released to help push the piston.

To get better control performance of the output pressure, a feedback control method is adopted, with a pressure sensor detecting the pressure of the boost chamber of the cylinder, and a controller, which are neglected in the schematic diagram for simplicity.

2 MATHEMATICAL ANALYSIS

To analyze the advantages of the energy regeneration system with hydraulic accumulator for hydraulic impulse testing equipment, comparisons should be done between hydraulic impulse testing equipment with and without accumulator, especially the energy consumption and system efficiencies. The hydraulic impulse testing system with accumulator is shown in Fig. 1, and the system without accumulator is the same as in Fig. 1, except that the accumulator connected to the cylinder and the corresponding chamber of the cylinder are omitted. For simplicity, as defined in Section 1, the boost stroke and return stroke may be analyzed separately under some conditions.

2.1 Power of the System without Accumulator

2.1.1 Load Power

In the boost stroke, load power means the power consumption of the test components, and in the return stroke, load power means the output power of the test components. In both cases, load power of the hydraulic impulse testing system without accumulator is given as:

$$P_L = p_L q_L, \tag{1}$$

where p_L is the pressure of the test components, which can be measured with a pressure sensor, and q_L is the flow rate at the inlet of the test components, which is given as:

$$q_L = \frac{dV_L}{dt}, \tag{2}$$

where V_L is the volume of the test components, including the boost chamber of the cylinder connected together. According to the pressure formula of closed volume chambers:

$$dp_L = \frac{E \cdot dV_L}{V_L}, \tag{3}$$

where E is the equivalent bulk modulus, determined by the bulk modulus of the test components E_c and the bulk modulus of the hydraulic oil E_o, and can be given as:

$$\frac{1}{E} = \frac{1}{E_c} + \frac{1}{E_o}. \tag{4}$$

2.1.2 Power of the Pressure Source

In the boost stroke, a positive signal is input to the servo valve, and the control chamber of the cylinder is connected to the pressure source through the servo valve. It should be noticed that the system-pressure-chamber of the cylinder is always connected to the pressure source. Therefore the pressure-boost cylinder works in a differential mode, and the power of the pressure source is determined by the system pressure p_s, the difference of the input flow rate into the control chamber q_1 and the output flow rate from the system-pressure-chamber q_2. For simplicity, it is assumed that the pressure drop of the servo valve is small enough to be omitted. Therefore the power of the pressure source in the boost stroke can be given as:

$$P_{sB} = p_s \cdot (q_1 - q_2). \tag{5}$$

On the return stroke, a negative signal is input to the servo valve and the control chamber of the cylinder is connected to the tank through the servo valve. The system-pressure-chamber of the cylinder is still connected to the pressure source so the piston of the cylinder moves to the left and the power of the pressure source can be given as:

$$P_{sR} = p_s \cdot q_2. \tag{6}$$

2.2 Power of the System with Accumulator

The calculations of the load power and the pressure source power of the hydraulic impulse testing system with accumulator is the same as that of the system without accumulator, as mentioned in 2.1. The only difference is that a hydraulic accumulator and corresponding variable damping are adopted.

2.2.1 Power of the Accumulator

On the boost stroke, the power of the accumulator means the output power of the accumulator and, on the return stroke, the power of the accumulator means the power stored in the accumulator. In both cases, the power of the accumulator of the hydraulic impulse testing system is given as:

$$P_a = p_a \cdot q_a, \tag{7}$$

where p_a is pressure at the inlet of the accumulator, which can be measured by a pressure sensor, and q_a is the flow rate at the inlet of the accumulator. Since the cycle time of the hydraulic impulse testing is very short, the accumulator can be considered to be working in an adiabatic process. And according to the polytropic gas law:

$$p_a V_a^{1.4} = p_0 V_0^{1.4} = cons., \tag{8}$$

where V_a is the gas volume of the accumulator, and p_0 and V_0 are the initial pre-charge pressure and initial gas volume of the accumulator, respectively. The flow rate at the inlet of the accumulator is given as:

$$q_a = \frac{dV_a}{dt}. \tag{9}$$

2.2.2 Variable Damping

The variable damping between the accumulator chamber and the control chamber of the cylinder is designed by the mechanical clearance, which is determined by the length l of the gap seal. The flow rate through the clearance of the accumulator chamber and the control chamber of the cylinder is given as:

$$q_d = \frac{\pi d \delta^3}{12 \mu l} \cdot \Delta p \pm \frac{\pi}{2} \cdot d \delta u, \tag{10}$$

where d is the piston diameter in the accumulator chamber, which is used for the mechanical gap seal, δ, l are the clearance and length of the seal, μ is the dynamic viscosity of the hydraulic oil, and u is the velocity of the piston.

It can be concluded from formula (10) that the damping changes with the gap seal length l, which is determined by the location of the piston. When the piston moves to the right end of the cylinder, the seal length l is designed to be small enough so that hydraulic oil can be supplemented for the accumulator chamber. In contrast, when the piston moves to the left end of the cylinder, the seal length l is designed to be long enough so that the accumulator chamber is isolated from the control chamber in a short time. As a result, the gas in the accumulator can be compressed and a higher pressure can be obtained to store energy.

2.3 Energy Consumption of the System without Accumulator

2.3.1 Energy Consumption of the Load

In both the boost stroke and the return stroke, the energy consumption of the load of the hydraulic impulse testing system without accumulator is given as:

$$E_L = \int p_L \cdot q_L dt. \tag{11}$$

It should be noted that in the return stroke, Eq. (11) means stands for the energy output of the test components.

2.3.2 Energy Consumption of the Pressure Source

In the boost stroke, the energy consumption of the pressure source is given as:

$$E_{sB} = \int p_s \cdot (q_1 - q_2) dt. \tag{12}$$

In the return stroke, the energy consumption of the pressure source is given as:

$$E_{sR} = \int p_s \cdot q_2 dt. \tag{13}$$

2.4 Energy Consumption of the System with Accumulator

The calculations of the energy consumption of the load and the pressure source of the hydraulic impulse testing system with accumulator is the same as that of the system without accumulator, as mentioned in 2.3. The only difference is that a hydraulic accumulator is adopted, the energy consumption of which is given as:

$$E_a = \int p_a \cdot q_a dt. \tag{14}$$

It should be noted that in the return stroke, Eq. (14) means the energy stored in the accumulator, while in the boost stroke, Eq. (14) means the energy released by the accumulator, which works as a power source.

2.5 Energy Efficiency of the System without Accumulator

2.5.1 Boost Stroke

In the boost stroke, the pressure source is the only energy source for the load, so the energy efficiency

of the hydraulic impulse testing system without accumulator is given as:

$$\eta_{WB} = \frac{E_L}{E_{sB}}. \quad (15)$$

2.5.2 Return Stroke

In the return stroke, both the energy from the test components and from the pressure source turns into heat eventually, so the energy efficiency of the hydraulic impulse testing system without accumulator is 0.

2.6 Energy Efficiency of the System with Accumulator

2.6.1 Boost Stroke

In the boost stroke, both the pressure source and the accumulator provide energy for the test components, so the energy efficiency of the hydraulic impulse testing system with accumulator is given as:

$$\eta_{AB} = \frac{E_L}{E_a + E_{sB}}. \quad (16)$$

2.6.2 Return Stroke

In the return stroke, besides the energy from the pressure source, the high pressure energy stored in the test components is released and converted to the high pressure energy stored in the accumulator. So the energy efficiency of the hydraulic impulse testing system with accumulator is given as:

$$\eta_{AB} = \frac{E_a}{E_L + E_{sR}}. \quad (17)$$

2.6.3 Total Efficiency

Since in the return stroke, no energy is input to the load, the only useful energy into the load is the energy from the pressure source and accumulator in the boost stroke. So the total efficiency of the systems without and with accumulator is given as:

$$\eta_T = \frac{E_L}{E_{SB} + E_{sR}}, \quad (18)$$

where E_L is the load energy consumption in the boost stroke.

3 SIMULATION AND CALCULATIONS

To further compare the energy consumptions and system efficiencies of the hydraulic impulse testing systems with and without accumulator, simulation models are built in AMESim, as shown in Figs. 2 and 3. In the simulation model, the pressure-boost cylinder is built using the hydraulic component design library in the AMESim.

Table 1. *Simulation parameters*

Pressure source	system pressure [MPa]	18
	pump maximum flow rate [L/min]	9
	accumulator volume [L]	6.3
	pre-charge pressure [MPa]	10
	oil bulk modulus [MPa]	1100
Servo valve	natural frequency [Hz]	350
	maximum flow rate [L/min]	100
	corresponding pressure drop [MPa]	1
Pressure-boost cylinder	piston mass [kg]	11.7
	area of control chamber [m^2]	1.23×10^{-2}
	area of system pressure chamber [m^2]	8.65×10^{-3}
	area of booster chamber, [m^2]	2.8×10^{-3}
	maximum piston displacement [m]	0.072
	area of accumulator chamber, [m^2]	1.59×10^{-3}
Test hose	diameter [m]	0.019
	length [m]	0.96
	effective bulk modulus [MPa]	850
Accumulator	gas pre-charge pressure [MPa]	11
	volume [L]	1
Damping	orifice diameter [mm]	0.1~1.5

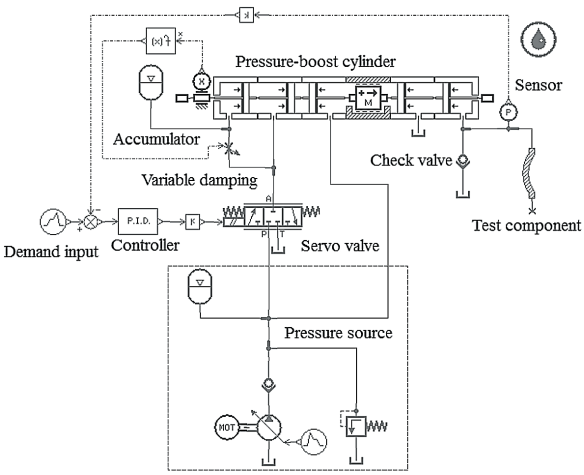

Fig. 2. *Simulation model of the system with accumulator*

Other hydraulic components such as the pressure source, check valve, pressure sensor, and accumulator are built using the standard hydraulic library. The test component is a hydraulic hose. To compare the

simulation results of the two systems, the simulation parameters are the same and are shown in Table 1. It should be noted that in Table 1, the parameters of the accumulator and variable damping is only suitable for the energy regeneration system for hydraulic impulse testing equipment with accumulator.

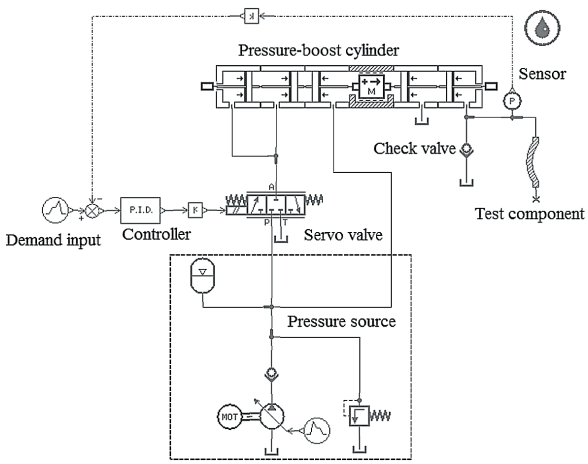

Fig. 3. *Simulation model of the system without accumulator*

In order to analyze both the boost stroke and return stroke of the systems, a square-wave demand input (or in other words, the desired output pressure), is adopted for the simulation, as shown in Fig. 4.

3.1 Comparisons of the Power of Systems with and without Accumulator

3.1.1 Load Power

Although the desired output pressures of the hydraulic impulse testing systems with and without accumulator are set to the same values, as shown in Fig. 4, there is still a minor difference in the actual output pressures of the two systems, as shown in Fig. 5. The flow rate at the inlet of the test component of the two systems is shown in Fig. 6. The positive data means that the hydraulic oil flows into the test component, while the negative data means that the hydraulic oil flows out of the test component. It is easy to see that at the initial stage of the boost stroke, the flow rate into the test component of the system with accumulator is larger than that of the system without accumulator, which is a result of the release of energy from the accumulator. Correspondingly, the output pressure of the system with accumulator rises faster than that of the system without accumulator, which can be explained by Eqs. (2) and (3).

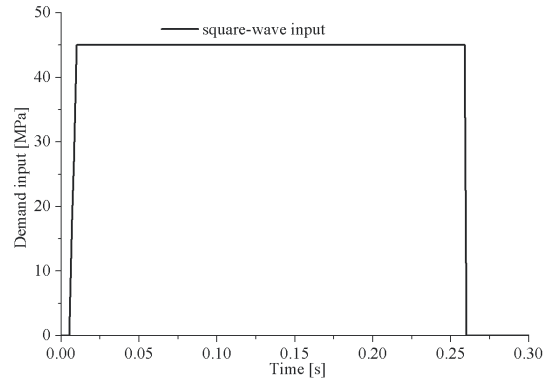

Fig. 4. *Square-wave demand input for simulation*

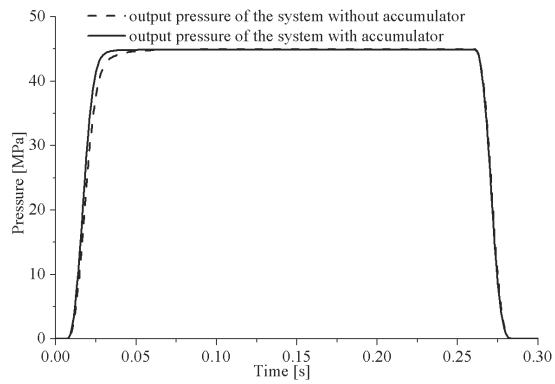

Fig. 5. *Output pressure of the system*

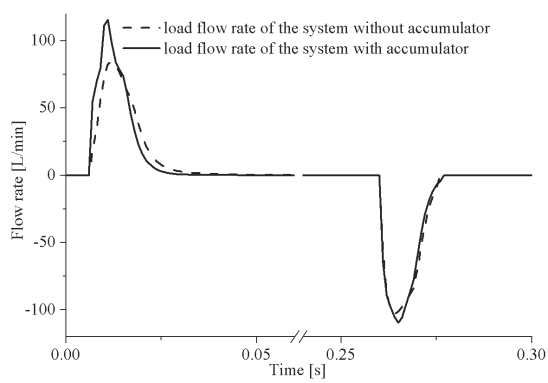

Fig. 6. *Load flow rate of the system*

According to Eq. (1), the load power of the hydraulic impulse testing systems can be calculated, as shown in Fig. 7. In the boost stroke, hydraulic oil flows into the test component, so the load consumes energy, shown as a positive result. On the other hand, in the return stroke, the test component works as an energy source to push the piston backward, and the load power is shown as a negative result. It should be noted that in the boost stroke, the maximum load power of the system with accumulator appears earlier

and larger than that of the system without accumulator because of the release of energy from the accumulator. In addition, it cannot be overlooked that in the return stroke, the load power is so large that it would be a huge waste if it were not recovered.

As can be seen from Figs. 6 and 7, in the boost stroke there is a significant difference between the load flow rate and the load power of the system with and without accumulator, while there is only a minor difference in the return stroke. The reason is that in the boost stroke, the pressure rise rate is so large that the flow rate from the pressure source is insufficient, which can be compensated by the accumulator. So, the flow rate supported by the accumulator makes a big difference. In the return stroke, energy released by the load is almost the same for the system with and without accumulator. The only difference is that for the system with accumulator some of the energy is absorbed by the accumulator, while for the system without accumulator all of the energy is wasted. However, the flow rate and power of the load are not affected.

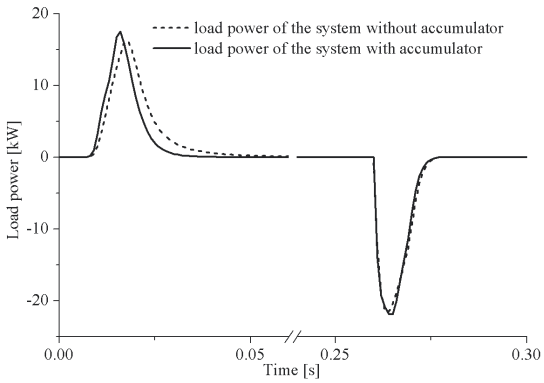

Fig. 7. *Load power of the system*

3.1.2 Power of the Pressure Source

Given that the system pressure is set at a fixed value of 18MPa, the power of the pressure source is mainly determined by the system flow rate, which is shown in Fig. 8. In the boost stroke, the pressure-boost cylinder works in a differential mode, so the system flow rate is calculated by the difference of the input flow rate into the control chamber of the cylinder and the output flow rate from the system-pressure-chamber of the cylinder. While in the return stroke, the system flow rate is just the flow rate into the system-pressure-chamber of the cylinder. For convenience of comparison, both the system flow rate in the boost stroke and the system flow rate in the return stroke are shown in the same figure. It should be noted that the instantaneous large flow rate of the system is provided by the accumulator in the pressure source rather than the pump.

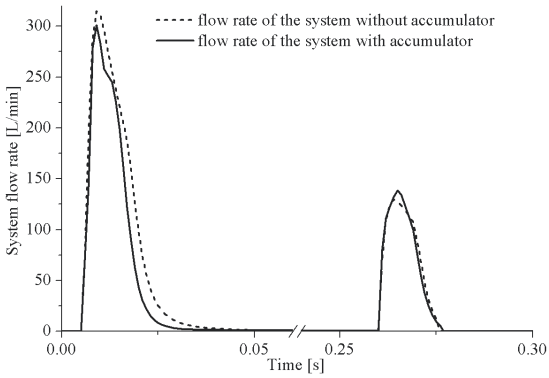

Fig. 8. *Flow rate of the system pressure source*

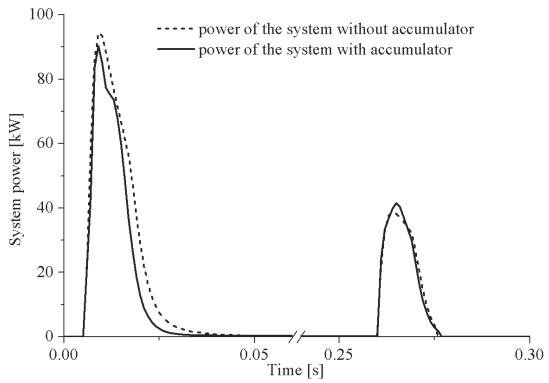

Fig. 9. *Power of the system pressure source*

According to Eqs. (5) and (6), the power of the systems can be calculated, as shown in Fig. 9. As can be seen from the figure, the maximum pressure source power of the system without accumulator is significantly greater than that of the system with accumulator.

3.1.3 Power of the Accumulator

For the hydraulic impulse testing system with accumulator, the pressure and flow rate at the inlet of the accumulator are shown in Fig. 10. For the flow rate, the positive data means that the hydraulic oil flows out of the accumulator, while the negative data means that the hydraulic oil flows into the accumulator. According to Eq. (7), the power of the accumulator of the hydraulic impulse testing system with accumulator can be calculated, as shown in Fig. 11. As with the flow rate, the positive data means that

the accumulator works as an energy source, while the negative data means that the accumulator absorbs energy.

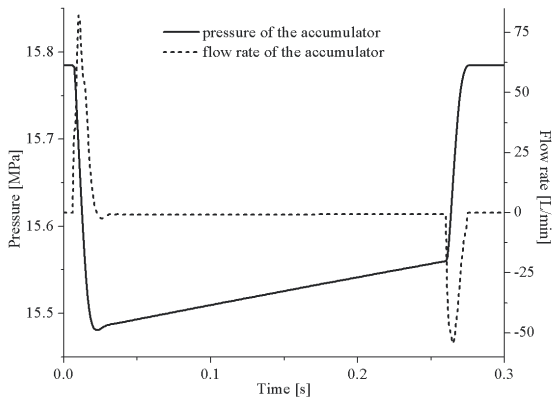

Fig. 10. *Pressure and flow rate of accumulator*

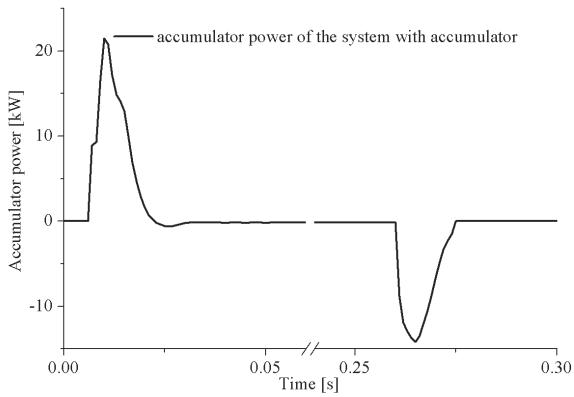

Fig. 11. *Power of the accumulator*

3.2 Comparison of Energy Consumption of Systems with and without Accumulator

For the hydraulic impulse testing system without accumulator, the energy consumption can be calculated by Eqs. (11) to (13); the calculated results are shown in Table 2. In the return stroke, the energy stored in the test component is released, so the energy consumption of the load is negative, which means that it is wasted. In both the boost stroke and the return stroke, the pressure source is constantly working, so the energy consumption remains positive.

For the hydraulic impulse testing system with accumulator, the energy consumption can be calculated by Eqs. (11) to (14); the calculated results are shown in Table 3. As in the system without accumulator, the negative energy consumption of the load in the return stroke means the energy released by the load. In addition, the negative energy released by the accumulator in the return stroke means energy stored in the accumulator.

Table 2. *Energy consumption of the system without accumulator*

Motion direction	Time [ms]	Pressure source [J]	Load [J]
Boost stroke	27	1078	877
Return stroke	15	318	–859
Total energy consumption		1396	-

Using the data in Table 3, we can determine that the energy recovery rate of the accumulator in the return stroke is (197/875)×100=22.5%, and the energy reuse rate of the accumulator in the boost stroke is (193/197)×100=98%.

By comparing the data in Table 2 and Table 3, it can be concluded that the system with accumulator can reduce energy consumption by ((1396–1186)/1396)×100=15% per cycle.

Table 3. *Energy consumption of the system with accumulator*

Motion direction	Time [ms]	Pressure source [J]	Accumulator [J]	Load [J]
Boost stroke	22	861	193	898
Return stroke	16	325	–197	–875
Total energy consumption		1186	-	-

3.3 Comparisons of Energy Efficiency of Systems with and without Accumulator

In the boost stroke, the efficiency of the hydraulic impulse testing system without accumulator can be calculated by Eq. (15) and the data in Table 2. In the return stroke, the efficiency of the hydraulic impulse testing system without accumulator is 0, as analyzed in 2.5.2.

In the boost stroke, the efficiency of the hydraulic impulse testing system with accumulator can be calculated by Eq. (16) and the data in Table 3. In the return stroke, the efficiency of the hydraulic impulse testing system with accumulator can be calculated by Eq. (17) and the data in Table 3.

Comparisons of the energy efficiency are shown in Table 4. The total efficiency of the system is calculated by the energy consumption of the load in the boost stroke divided by the total energy consumption of the pressure source. It is apparent that the efficiency of the system with accumulator is higher than that of the system without accumulator. The reason is that in the return stroke, the system with accumulator can recover energy from the load and then release the recovered energy in the next boost

stroke, while for the system without accumulator, the energy stored in the load is totally wasted in the return stroke and turns into heat.

Table 4. *Comparisons of the energy efficiency of the hydraulic impulse testing system*

Motion direction	System without accumulator [%]	System with accumulator [%]
Boost stroke	80.68	85.2
Return stroke	0	16.4
Total efficiency	62.82	75.71

4 CONTROL PERFORMANCE

To study the control performance of the energy regeneration system with accumulator for hydraulic impulse testing equipment, experiments were carried out on a prototype. The performance of the hydraulic impulse testing equipment is compared with that of the hydraulic impulse testing equipment without accumulator. To compare the experimental results with the simulation results, the parameters of the prototype are set the same with the simulation models, which are shown in Table 1.

4.1 Step-Input Response

The step-input response of the hydraulic impulse testing system with and without accumulator is studied. Both the simulations and experiments were carried out, the results of which are shown in Figs. 12 and 13. The key data of for the results is shown in Tables 5 and 6. As can be seen from the results, both systems can achieve the goal with a minor steady state error. However, the system with accumulator can achieve the goal with at a faster speed than the system without accumulator, which is the result of the energy regeneration by the accumulator.

It should be noted that there are some differences between the simulation and the experimental results. The response time lag of the experimental results is more apparent compared with the simulation results, the reason for this is that the damping forces of the seals and the piston in the simulation model are neglected and some parameters such as the bulk modulus of the hydraulic oil may be slightly different from the actual parameters. In addition, the accuracy and response speed of the components and parts of the experimental systems cannot compare with those of the simulation systems. Therefore the steady state error of the experimental results is larger than that of the simulation results. However, the shape and trend of the experimental curves, especially the influence of the accumulator, are consistent with the simulation results. Both the simulation results and the experimental results show that the system with accumulator can achieve the goal with a faster speed than the system without accumulator, while the steady state error is acceptable for the hydraulic impulse testing equipment.

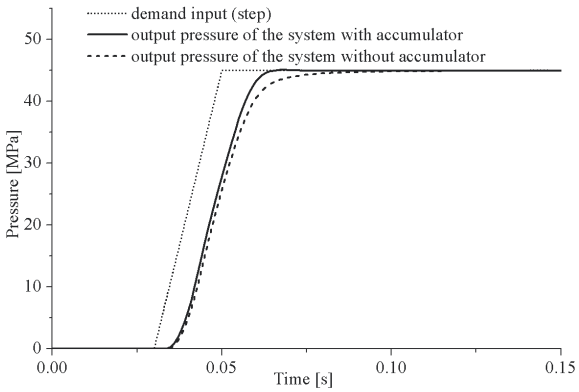

Fig. 12. *Simulation results of step-input*

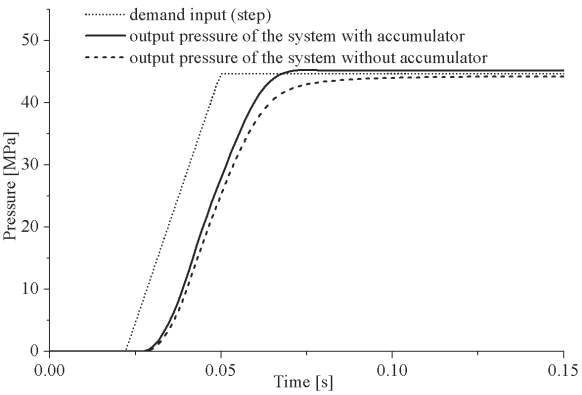

Fig. 13. *Experiment results of step-input*

Table 5. *Key data of the simulation results of step-input*

	Demand input	System without accumulator	System with accumulator
Rise time [ms]	18	51	35
Final value [MPa]	45	44.9	44.96
Steady state error [%]	-	0.2	0.09

Table 6. *Key data of the experiment results of step-input*

	Demand input	System without accumulator	System with accumulator
Rise time [ms]	24	60	42
Final value [MPa]	44.7	44.3	45.14
Steady state error [%]	-	0.9	1

4.2 Square-Wave-Input Response

For the hydraulic impulse testing equipment, the most commonly adopted pressure wave forms are the square-wave and the peak-wave. The square-wave-input response of the system with and without accumulator is studied. Both simulations and experiments were carried out and the results are shown in Figs. 14 and 15. As can be seen from the results, both systems can achieve the goal with a minor steady state error. However, the system with accumulator can achieve the goal with a faster speed than the system without accumulator.

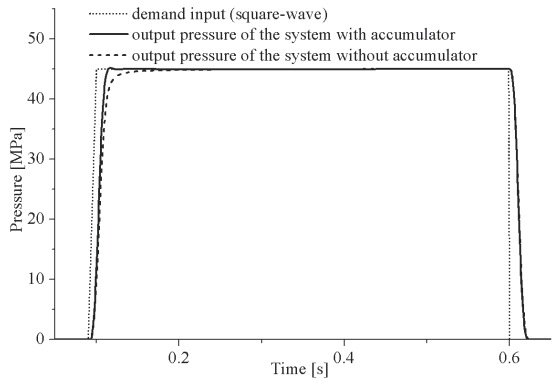

Fig. 14. *Simulation results of square-wave-input*

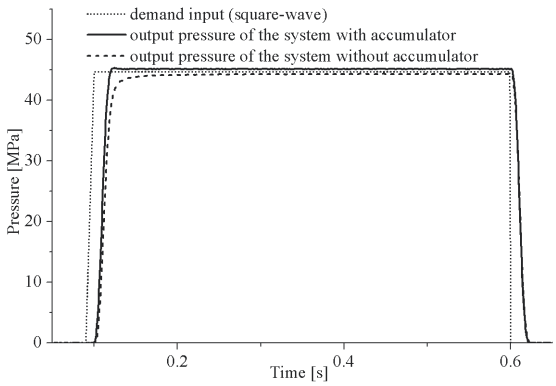

Fig. 15. *Experiment results of square-wave-input*

As with the step-input response, the response time lag and steady state error of the experimental results are larger than that of the simulation results, the reason for this is that the damping forces of the seals and the piston in the simulation model are neglected, and some parameters such as the bulk modulus of the hydraulic oil may be slightly different from the actual parameters. However, the shape and trend of the experiment curves, especially the influence of the accumulator, are consistent with the simulation results. Both the simulation results and the experiment results show that the system with accumulator can achieve the goal with a faster speed than the system without accumulator.

4.3 Peak-Wave-Input Response

The peak-wave-input response of the hydraulic impulse testing system with and without accumulator is studied. Both simulations and experiments were carried out and the results are shown in Figs. 16 and 17. It can be seen from the results that the pressure rise rate of the hydraulic impulse testing system with accumulator is larger than that of the system without accumulator. Since the pressure rise rate of the peak-wave is relatively large, the system with accumulator can achieve the goal better.

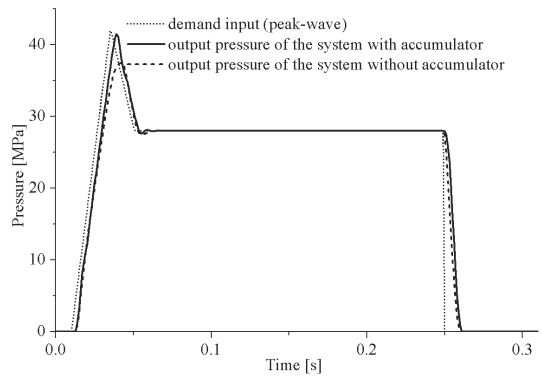

Fig. 16. *Simulation results of peak-wave-input*

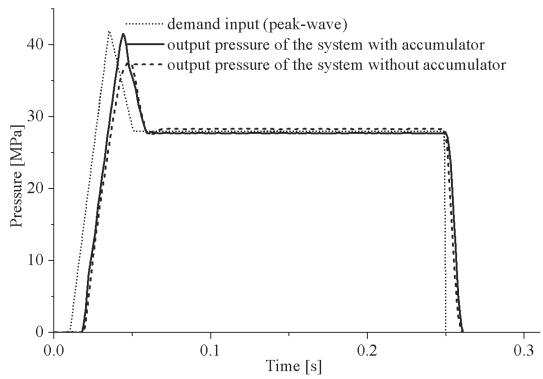

Fig. 17. *Experiment results of peak-wave-input*

As with the step-input response and square-wave-input response, the response time lag of the experimental results is larger than that of the simulation results, the reason for this is that the damping forces of the seals and the piston in the simulation model are neglected, and some parameters such as the bulk modulus of the hydraulic oil may

be slightly different from the actual parameters. However, the shape and trend of the experiment curves, especially the influence of the accumulator, are consistent with the simulation results. Both the simulation results and the experiment results show that the system with accumulator can achieve the goal better, with a larger pressure rise rate than the system without accumulator.

5 CONCLUSIONS

An energy regeneration system for hydraulic impulse testing equipment with accumulator is proposed, which serves as a form of novel energy-saving hydraulic impulse testing equipment. Mathematical analysis and simulations show that the hydraulic impulse testing system with accumulator can reduce energy consumption by 15 % over that of a system without an accumulator in the cycle, while the energy efficiency of the hydraulic impulse testing system is increased from 62.82 to 75.71 % by the adoption of an accumulator. Both simulation and experimental results show that the control performance of the hydraulic impulse testing equipment with accumulator is better than that of the equipment without accumulator: more specifically, a faster response speed and a larger pressure rise rate are achieved. In addition, the most commonly adopted pressure wave forms for hydraulic impulse testing, including square-wave and peak-wave, can be obtained by the energy regeneration system with accumulator.

6 ACKNOWLEDGEMENTS

The authors would like to thank the sponsor of the Science Fund for Creative Research Groups of the National Natural Science Foundation of China (No: 51221004).

7 REFERENCES

[1] Wang, F., Gu, L. Chen, Y. (2013). A Hydraulic Pressure-Boost System Based on High-Speed. *IEEE/ASME Transactions on Mechatronics*, vol. 18, no. 2, p. 733-743, **DOI:10.1109/TMECH.2011.2182654**.

[2] Lin, T., Wang, Q. (2012). Hydraulic accumulator-motor-generator energy regeneration system for a hybrid hydraulic excavator. *Chinese Journal of Mechanical Engineering*, vol. 25, no. 6, p. 1121-1129, **DOI:10.3901/CJME.2012.06.1121**.

[3] Ho, T.H., Ahn, K.K. (2010). Modeling and simulation of hydrostatic transmission system with energy regeneration using hydraulic accumulator. *Journal of Mechanical Science and Technology*, vol. 24, no. 5, p. 1163-1175, **DOI:10.1007/s12206-010-0313-8**.

[4] Do, H.T., Ahn, K.K. (2013). Velocity control of a secondary controlled closed-loop hydrostatic transmission system using an adaptive fuzzy sliding mode controller. *Journal of Mechanical Science and Technology*, vol. 27, no. 3, p. 875-884, **DOI:10.1007/s12206-012-1237-2**.

[5] Wang, C., Jiao, Z., Wu, S., Shang, Y. (2014). Nonlinear adaptive torque control of electro-hydraulic load system with external active motion disturbance. *Mechatronics*, vol. 24, no. 1, p.32-40, **DOI:10.1016/j.mechatronics.2013.11.005**.

[6] Minav, T., Hänninen, H., Sinkkonen, A., Laurila, L., Pyrhönen, J. (2014). Electric or hydraulic energy recovery systems in a reach truck– a comparison. *Strojniški vestnik – Journal of Mechanical Engineering*, vol. 60, no. 4, p. 232-240, **DOI:10.5545/sv-jme.2013.1581**.

[7] Andersen, T.O., Hansen, M.R., Pedersen, H.C. (2005). Regeneration of potential energy in hydraulic forklift trucks. *The 6th International Conference on Fluid Power Transmission and Control*, Hangzhou, p. 380-384.

[8] He, W., Zhang, S., Ge, S.S. (2014). Adaptive control of a flexible crane system with the boundary output constraint. *IEEE Transactions on Industrial Electronics*, vol. 61, no. 8, p. 4126-4133, **DOI:10.1109/TIE.2013.2288200**.

[9] Bing, X., Jian, Y., Yang, H.Y. (2005). Comparison of energy-saving on the speed control of the VVVF hydraulic elevator with and without the pressure accumulator. *Mechatronics*, vol. 15, no. 10, p. 1159-1174, **DOI:10.1016/j.mechatronics.2005.06.009**.

[10] Lin, T.L., Wang, Q.F., Hu, B.Z., Gong, W. (2010). Research on the energy regeneration systems for hybrid hydraulic excavators. *Automation in Construction*, vol. 19, no.8, p. 1016-1026, **DOI:10.1016/j.autcon.2010.08.002**.

[11] Evans, C.W. (1980). Testing requirements for hydraulic hose. *Polymer Testing*, vol. 1, no. 1, p. 39-49, **DOI:10.1016/0142-9418(80)90025-2**.

[12] BS EN ISO 6802:2008. *Rubber and Plastics Hoses and Hose Assemblies with Wire Reinforcements - Hydraulic Impulse Test with Flexing*. International Organization for Standardization, Geneva.

[13] ISO 1436:2009. *Rubber Hoses and Hose Assemblies - Wire-Braid-Reinforced Hydraulic Types for Oil-Based or Water-Based Fluids - Specification*. International Organization for Standardization, Geneva.

[14] ISO 6605:2002. *Hydraulic Fluid Power - Hoses and Hose Assemblies - Test Methods*. International Organization for Standardization, Geneva.

[15] ISO 6772:1988. *Aerospace - Fluid Systems - Impulse Testing of Hydraulic Hose, Tubing and Fitting Assemblies*. International Organization for Standardization, Geneva.

[16] SAE AIR1228 (2007). *Standard Impulse Machine Equipment and Operation*. Society of Automotive Engineers, Warrendale.

[17] Kim, H.E., Lee, G.C. Kim, J.H. (2010). System design and performance test of hydraulic intensifier. *Transactions of the Korean Society of Mechanical Engineers*, vol. 34, no. 7, p. 947-952, **DOI:10.3795/KSME-A.2010.34.7.947**. (in Korean)

[18] Song, K., Zhao, S., Liao, J., Dou, Y., Zhao, X. (2011). Research on key technology of hydraulic impulse testing equipment. *Journal of Aerospace Engineering*, vol. 24, no. 4, p. 409-414, **DOI:10.1061/(ASCE)AS.1943-5525.0000086**.

Strojniški vestnik - Journal of Mechanical Engineering 61(2015)3, 207-213

DOI:10.5545/sv-jme.2014.2017
Original Scientific Paper
Received for review: 2014-07-28
Received revised form: 2014-11-21
Accepted for publication: 2014-12-18

Integrated Electro-Hydraulic Machine with Self-Cooling Possibilities for Non-Road Mobile Machinery

Pavel Ponomarev[1] – Tatiana Minav[2] – Rafael Åman[3] – Lauri Luostarinen[3]

[1] Lappeenranta University of Technology, LUT Energy, Finland
[2] Aalto University, School of Engineering, Finland
[3] Lappeenranta University of Technology, LUT Mechanical Engineering, Finland

Over the past few years, due to the introduction of Tier 4 emission legislations, new developments for non-road mobile machinery (NRMM) applications to meet these stringent targets have been introduced. This paper presents a design concept for self-cooling of integrated electro-hydraulic machinery for NRMM application. The applicability of this concept is shown for an integrated electro-hydraulic energy converter (IEHEC). Two cooling schematics (passive and active) are proposed. In the passive cooling scheme the coolant flow is obtained from the case drain leakage flow of the hydraulic machine. In the active cooling scheme a boost pump can be used for providing optimal coolant flow. We show that in an NRMM environment such an IEHEC can be utilized using a passive cooling scheme.

Keywords: fluid power, energy recuperation, hybrid drivetrain, hydraulic leakage, losses, cooling, efficiency, thermal management, non-road mobile machinery

Highlights

- *Design concept for self-cooling in Non-road mobile machinery applications was introduced.*
- *Two cooling schematics are proposed for an integrated electro-hydraulic energy converter.*
- *Integrated electro-hydraulic energy converter can be utilized with a passive cooling scheme.*
- *The proposed self-cooling concept allows a decrease in the power consumption in NRMM applications.*

0 INTRODUCTION

Globally, energy efficiency is becoming an increasingly important topic in the world of non-road mobile machines (NRMM) [1] and [2]. In order to be competitive on the market, a working machine producer should have energy efficient – hybrid or fully electric – products available for customers [3] and [4]. Electrification is one of the ways of creating more energy efficient NRMM [5]. The possibilities of utilizing electrical components in NRMM have generated wide interest in this research area [6] and [7]. However, in working hydraulics the actuators are supplied by fluid power transmission and cannot be replaced by electrical analogues due to the low power density of electrical components compared with hydraulic ones [3]. On the other hand, the conventional valve controlled fluid power systems are in many cases of poor efficiency. Thus there emerges a need for hydraulic actuators that can be directly driven (or pump-controlled) via electrical machines [8] and [9]. In addition, a suitable electrical machine is required to maintain full torque at zero speed to provide the required pressure level in hydraulic actuators. Maintaining full torque at low rotational speeds sets a demand for effective cooling. In [10] an integrated electro-hydraulic energy converter (IEHEC) was introduced. Fig. 1 illustrates a cross-sectional cut of the IEHEC.

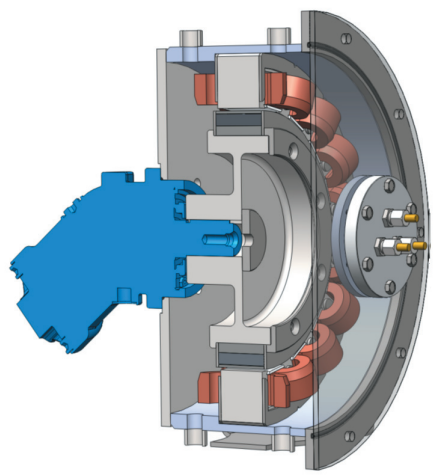

Fig. 1. *Cross-sectional cut of the IEHEC* [10]

A closed-loop fluid power circuit, which can replace traditional valve-controlled fluid power circuits in NRMM applications, consists of an IEHEC (hydraulic pump driven by an integrated electrical motor), flow compensation accessories and a hydraulic cylinder. The electrical machine is driven by a frequency converter with regenerative capabilities.

*Corr. Author's Address: Aalto University, School of Engineering, Department of Engineering Design and Production, Espoo, Finland, tatiana.minav@aalto.fi

The cooling of the integrated electrical machine is arranged by taking coolant flow from the fluid power system.

The hydraulic power can be obtained from the hydraulic machine driven by the integrated electrical machine. The electrical machine is controlled by a frequency converter connected to the main DC bus of an electrical/hybrid-electrical NRMM. Instead of a conventional directional control valve (DCV), an electrically drive pump-controlled fluid power system is applied, which offers the possibility of reducing both pipe line and throttling losses. The hydraulic machine driven by a controlled electrical machine delivers the exact amount of power required for the actuator. The amount of power is regulated electrically directly via a permanent magnet synchronous machine (PMSM) and a frequency converter. During lowering of payload in lifting applications from the initial extended position in NRMM, the control algorithm of the inverter allows the recuperation of excessive mechanical energy directly into electrical energy [3]. The released electrical energy can be stored in a battery or a super capacitor and reused later.

The efficiency of modern industrial electrical machines in the power range of 5 to 500 kW at nominal working point is typically 90 to 95 %. This means that about 5 to 10 % of the input energy is converted to heat instead of producing effective work. Fig. 2 illustrates the measured efficiency chart of the electrical machine of an IEHEC [10].

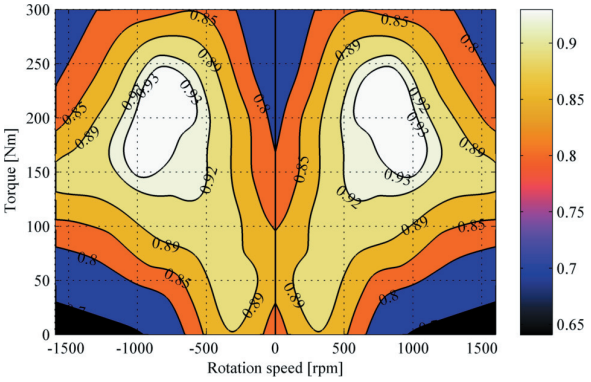

Fig. 2. *Efficiency map of electrical machine*

The high pressure level requires high torque from the electrical machine. High torque imposes high currents flowing into the machine windings. These high currents produce heat due to the Joule losses in the copper conductors. Additional heat is produced in the laminated iron stack due to the eddy-current and hysteresis losses in the iron [11]. If permanent magnets or solid conducting material are used in the machine construction, then eddy current losses are also generated in these components. This heat needs to be transferred from the electrical machine in order to limit the temperature rise and prevent possible damage to the winding insulation and permanent magnets [12]. Therefore, the cooling capability of electrical machines is an important factor in their operation. Usually, a separate cooling system is arranged for high-torque-density electrical machines, e.g. liquid cooling with a separate cooling pump or a fan system with a radiator assembly. Such a cooling system requires additional power to operate.

Many recent studies have focused on using oil as a cooling liquid [13] and [14]. Paper [15] presents comparisons of utilizing direct oil cooling approaches and conventional indirect cooling approaches for electrical motors mounted in hybrid electric vehicles or in zero emission vehicles.

In this paper two cooling approaches for electrical machines are introduced for non-road mobile machinery using the example of a direct-immersion-liquid cooled electrical machine in the IEHEC. Firstly, the approach reduces the amount of additional power required for cooling purposes by utilization of case drain leakage in the hydraulic equipment under loading conditions. Secondly, the approach utilizes a controlled boost pump for maintaining an optimal thermal regime for the machinery. Only the first approach is analyzed in detail in order to ensure that passive cooling is capable of maintaining the machinery within its thermal limits.

The remainder of this paper is organized as follows. Section 1 suggests schemes and principles for the system cooling. Section 2 describes test setup and measurements performed for the passive cooling approach in detail. Section 3 shows the formulas that are used for thermal analysis of the system. Results of the analysis are described in Sections 4. Concluding remarks are presented in Section 5.

1 COOLING METHODS CONFIGURATION

This section describes the background, proposed schemes and principles for system cooling in NRMM applications.

1.1 Leakage in Hydraulic Machines

According to [16], the measured performance characteristics of a pump-motor are often supplied by the manufacturer in graphical form and are therefore typical for that type and size of hydraulic machine. Fig. 3 shows one way of presenting the performance

characteristics of an axial piston machine acting as either a pump, or a motor. It can be seen that the optimum efficiency is located around a preferred pressure setting and speed. The optimum condition is dependent on the mechanical design and the machine size. It is important to ensure the best efficiency by selecting the correct machine size. The conditions for optimum efficiency are not the same when the machine role is reversed [16]. Efficiency charts of certain axial piston machine are presented in Fig. 3.

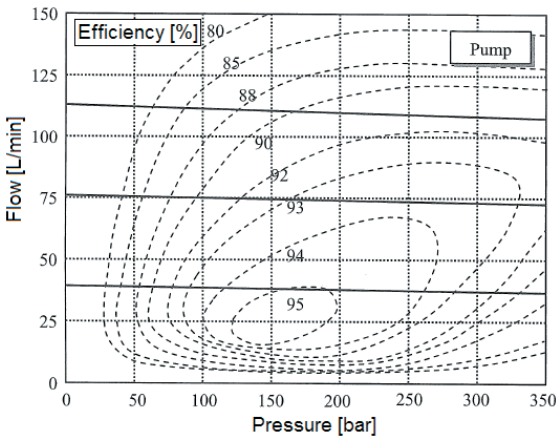

a)

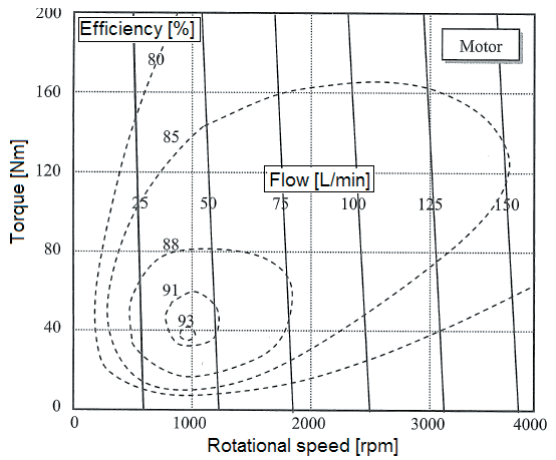

b)

Fig. 3. *Performance characteristics of an axial piston machine acting as: a) a pump and, b) a motor* [16]

In Fig. 3b torque corresponds to pressure and rotational speed to volume flow because the bent-axis piston hydraulic machine in question is of a fixed displacement type. This hydraulic machine can be operated in four quadrants.

According to [16], it is important to know that the difference between the input and the output flow rate is not the same as the case drain leakage (Fig 4). Pump internal leakage and resistance have a significant effect on the pump efficiency.

Therefore, it is difficult to predict case drain leakage at various operating points using just performance characteristics provided by the manufacturer. The exact leakage amount can be determined by extensive measurements where the number of measurement points is extremely large as case leakage depends on many variables, such as operating point (output pressure and flow rate), speed, inlet pressure, drain port pressure, temperature, and hydraulic oil properties.

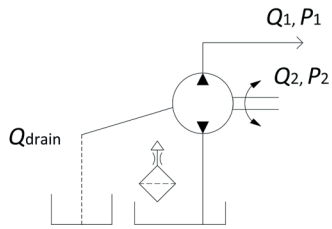

Fig. 4. *Case drain leakage*

Due to these practical difficulties, in this paper several assumptions concerning leakage flow rate are made in order to simplify analysis. According to the measurements, case drain leakage has been shown to be in the close vicinity of a certain value assumed to be constant and averaged from just a few measurement points.

1.2 Active Cooling: Boost Pump Operation

Usually, the case drain leakage flow in a closed-loop system is directed to the main hydraulic tank and is later returned to the circuit by a boosting pump. Fig. 5 illustrates a fluid power circuit with implemented active cooling.

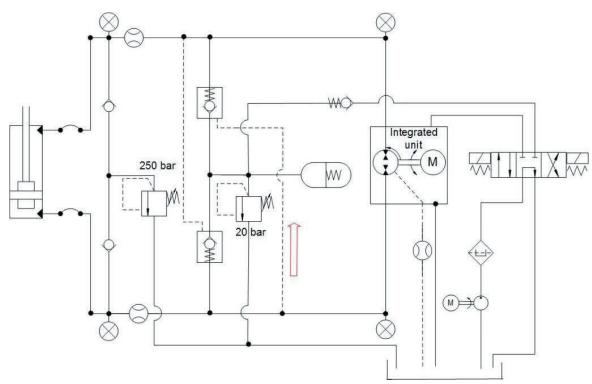

Fig. 5. *Active cooling of an electrical machine with boost pump operation*

The directional control valve is used for the prioritization of boost pump operation. The boost

pump flow is primarily directed to the pressure accumulator; otherwise the flow is directed through the electrical machine to cool down the windings, according to the measured temperature. If no boost or cooling flow is required, the boost pump flow is directed to free flow in order to consume as low a power as possible. With more advanced control the boost pump could be switched off when neither boost nor cooling flow is required.

Pressure losses in electrical machines with boost-pump cooling can be designed to be negligibly low by increasing the dimensions of the inlet and outlet lines. The dimension of the cooling lines does not influence the electro-mechanical operation of the electrical machine.

An active cooling scheme requires the following changes to the closed-loop fluid power circuit:

- directing boost pump flow (additional directional control valve),
- increased operation of the boost pump will increase energy consumption.

Therefore, an active cooling approach requires energy supply and additional components. Due to these technical limitations, passive self-cooling is suggested, as passive cooling does not require additional power for coolant circulation.

1.3 Passive Self-Cooling

Fig. 6 shows a simple closed-loop fluid power circuit with implemented passive self-cooling. Cooling flow is obtained from the case drain leakage flow of the hydraulic machine and it is then guided to integrated electrical machine. Pressure losses in the electrical machine can be seen as negligible since cooling of the stator stack does not require the housing to be filled to its top. The outgoing flow will move by gravity as long as the outlet and inlet ports are of adequate dimensions.

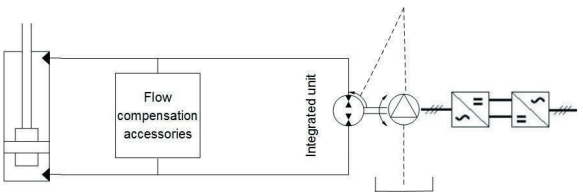

Fig. 6. *Cooling of the electrical machine obtained from the case drain leakage flow*

Due to the low flow rate of the case drain leakage it has been suggested to prefill the IEHEC and equip the drain line from the IEHEC to the tank with a throttle orifice and 2/2 directional control valve. By these means the heat produced in the windings can be effectively conducted into the IEHEC's metal body through the oil. In addition, the coolant flow rate, i.e. the case drain leakage flow, keeps bringing in the coolant oil. The directional control valve is there to prevent the IEHEC from draining to empty while standby.

The following Section 2 describes measurements of the case drain leakage flow. In these measurements the leakage flow was directed to the tank without guiding through the electrical machine.

2 MEASUREMENT OF CASE DRAIN LEAKAGE FLOW

Fig. 7 shows a photo of the case drain leakage measurement setup. The main component is the IEHEC [17]. The hydraulic machine maximum operating speed is 1500 rpm. The nominal pressure is 400 bar and the nominal flow rate is 100 l/min. An ABB ACSM1 drive was used to control the IEHEC. Fig. 5 shows the schematics of the hydraulic circuit implemented for testing case drain leakage flow.

Fig. 7. *Photo of test setup*

Fig. 8 shows the leakage flow measurement points versus the rotational speed. The measurement was carried out by driving the fluid power circuit shown in Fig. 6 through its different operating points. During operation the drain leakage flow was measured using the flow sensor KRACHT VC 0.2 [19]. The leakage flow rate varies between 0.15 to 0.24 l/min during motoring mode, and between 0.19 to 0.33 l/min in the generating mode of the electrical machine. Fig. 8 illustrates the different operational points during leakage measurements. Fluid temperature was

maintained at 40 °C. The positive speeds corresponds to the pumping mode for the hydraulic machine, and the negative rotational speeds to the motoring mode. The pressure level in bars is indicated as numbers near the measurement points. It can be seen in Fig. 8 that with increase of pressure drop (in bars) over the pump, leakage flow increased with the same rotational speed.

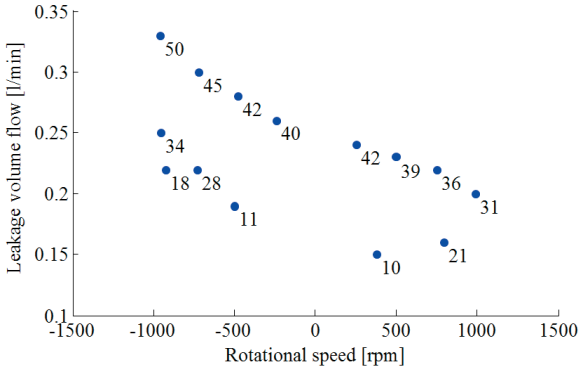

Fig. 8. *Measurement points of case drain leakage flow versus rotational speed*

The limitations of the measurement setup allowed measurements only in the low working pressure range below 50 bar. According to the measured points the case drain leakage flow in all other operating points is assumed to be 0.25 l/min.

3 THERMAL ANALYSIS

Output power P_{out} for an electrical machine at a motoring mode working point is calculated as:

$$P_{\text{out}} = \frac{w\pi T}{60}, \tag{1}$$

where w is motor speed, T is torque.

Power losses P_{loss} in an electrical machine at a motoring mode working point are calculated as follows:

$$P_{\text{loss}} = \left(\frac{1}{\eta} - 1\right) P_{\text{out}}, \tag{2}$$

where η is the electrical machine efficiency. Fig. 9 shows the power losses that are converted to heat for the electrical machine in motoring mode obtained from the efficiency map of Fig. 2 utilizing Eqs. (1) and (2). The efficiency difference in permanent magnet electrical machines with direct torque control between motoring and generating modes is negligibly small.

Taking into account that at different operating points the electrical machine has different losses, it is clear that there are two regions – one where losses are below the cooling capability (the region where an electrical machine can be safely utilized) and another region where cooling capability is insufficient to compensate for power losses with constant coolant flow.

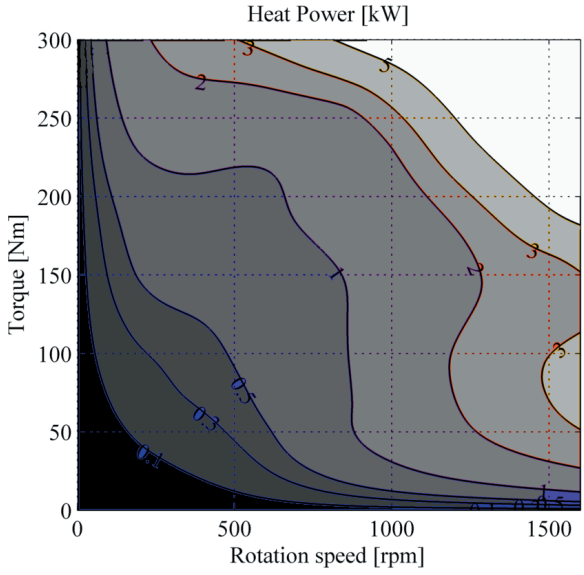

Fig. 9. *Heat power due to losses in the electrical machine during motoring mode* **[10]**

In this section the region of safe operation with self-cooling with case drain leakage flow is estimated. The following assumptions are used:

- Leakage flow is constant within the measured operating range (see Fig. 8) and is equal to 0.25 L/min.
- The whole amount of drain leakage oil participates in the heat removal. The possible flow of the coolant without capturing heat (e.g. directly from inlet to outlet without touching any hot surfaces) is neglected. Additionally, thermal resistance between the hot walls and the oil is neglected, and the thermal capacitance of the oil is also neglected by assuming ideal mixing **[14]**.
- There is no other heat removal interface, no convection cooling or no heat removal by conduction, which represents a worst-case scenario.
- There is no heat transfer between the hydraulic machine and the electrical machine.

The thermal balance equation allows for estimation of thermal rise. The allowed thermal rise is calculated from the coolant inlet temperature and maximum allowable temperature for the electrical

machine. The typical working temperature of hydraulic equipment is about 60 °C. Therefore, the base temperature for thermal analysis is set to 60 °C. The maximum allowable temperature for the electrical machine is limited by mechanical constraints, winding insulation thermal rating, and thermal rating of PMs. For the IEHEC's electrical machine the maximum temperature is set to 130 °C. Because the maximum operation temperature is higher than recommended for conventional mineral-oil-based hydraulic fluid, a fire-resistant hydraulic fluid (FRHF) should be used. According to **[18]**, FRHF can be used continuously in the temperature range up to 150 °C. Therefore, the allowable temperature rise is ΔT = 130°C – 60°C = 70 °C.

The temperature rise at every operating point under the abovementioned assumptions can be calculated as:

$$\Delta T = \frac{P_{\text{loss}}}{c_{\text{p}} Q_{\text{leak}} \rho}, \tag{3}$$

where c_{p} is the specific heat and it is 2300 J/kgK; ρ is the oil density and is equal to 880 kg/m^3; Q_{leak} is the case drain leakage oil flow rate in l/min and P_{loss} is estimated from the efficiency map as shown in Fig. 9.

Using these equations an operating region can be estimated along the whole operating range of the IEHEC, where the temperature rise under the abovementioned assumptions is acceptable.

4 RESULTS

In this study, the target was to show the feasibility of the self-cooling concept of integrated electro-hydraulic machinery for hybrid/electric NRMM applications. The feasibility depends on the assumptions. A lower temperature difference (ΔT) and a lower case drain flow rate can reduce the allowed temperature region in a significant manner. Therefore, to ensure practicality of this approach, the IEHEC's case drain leakage flow should be measured on a matrix of operating points along the whole operating range.

Fig. 10 shows the theoretical allowed region (light) for the IEHEC, where a passive self- cooling scheme is acceptable under the abovementioned assumptions.

This allowed region of operation is valid for the particular studied IEHEC. With a change in efficiency, or leakage flow, or cooling media the region could vary.

According to Fig. 10, if the intended region of operation is located in the allowed region for self-cooling, the electro-hydraulic machinery can operate safely without using additional power for cooling purposes. Short-time operation outside the allowed region can be acceptable as the cooling media has quite a high thermal capacity. Excessive heat can be accumulated for a short time within the machine components and the cooling media, assuming that the IEHEC operation point will return as fast as possible to the allowable operating region.

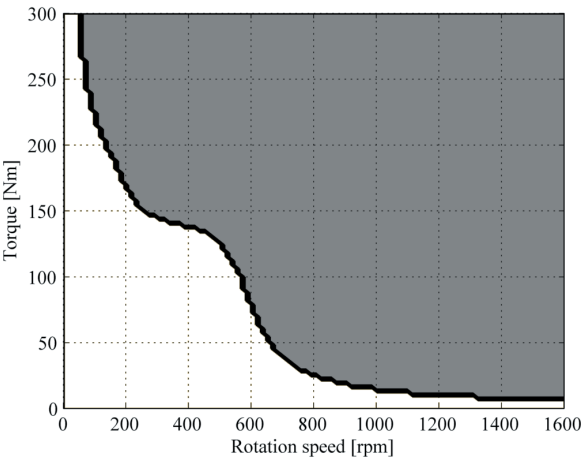

Fig. 10. *Allowed region of operation of the IEHEC*

This novel type of passive cooling would decrease the power consumption and increase the system efficiency in NRMM applications. An example of this application is a mobile crane lifting-lowering heavy payloads. In the case of active cooling, during the lifting cycle the main fluid power circuit reserves all the capacity of the boost pump and, therefore, it cannot be used in cooling. If the lifting cycle is longer it would require the addition of one more pump to cover the cooling needs. This would further increase the fuel consumption, the mass and the investment. Passive cooling is available even during a longer work cycle without additional power consumption and extra costs.

5 CONCLUSIONS

This paper introduces a new cooling method for high-torque-density electro-hydraulic machinery for NRMM applications. The self-cooling concept allows the reduction of additional components for cooling from the NRMM. The results show the allowed region for the IEHEC, where a passive self-cooling scheme is acceptable under the abovementioned assumptions. The proposed self-cooling concept allows a decrease

in the power consumption and an increase in the system efficiency in NRMM applications.

6 ACKNOWLEDGEMENTS

The research introduced in this paper has been carried out as a part of the EFFIMA (Energy and Life Cycle Cost Efficient Machines) - program of FIMECC (Finnish Metals and Engineering Competence Cluster). The research was enabled by the financial support of ECV Tubridi project (Tekes, the Finnish Funding Agency for Technology and Innovation) Laboratory of Electric Drives (LUT Energy), Laboratory of Intelligent Machines (LUT Mechanical Engineering) at Lappeenranta University of Technology and the Department of Engineering Design and Production of the School of Engineering of Aalto University.

7 REFERENCES

[1] Heybroek, K. (2008). *Saving Energy in Construction Machinery using Displacement Control Hydraulics: Concept Realization and Validation*. Licentiate thesis, Linköpings University, Linköping.

[2] Ivantysynova, M. (2008). Innovations in pump design-what are future directions. *International Symposium on Fluid Power*, Toyama, **DOI:10.5739/isfp.2008.59**.

[3] Minav, T. (2011). *Electric-Drive-Based Control and Electric Energy Regeneration in a Hydraulic System*. PhD thesis, Acta Universitatis Lappeenrantaensis 436, Lappeenranta University of Technology, Lappeenranta.

[4] Immonen, P. (2013). *Energy Efficiency of a Diesel-Electric Mobile Working Machine*. PhD. thesis, Acta Universitatis Lappeenrantaensis 518, Lappeenranta University of Technology, Lappeenranta.

[5] Lin, T., Wang, Q., Hu, B., Gong, W., (2010). Development of hybrid powered hydraulic construction machinery. *Journal Automation in Construction*, vol. 19, no. 1, p. 11-19, **DOI:10.1016/j.autcon.2009.09.005**.

[6] Ming, X., Bo, J., Guojin, C., Jing, N. (2013). Speed-control of energy regulation based variable-speed electrohydraulic drive. *Strojniški vestnik - Journal of Mechanical Engineering*, vol. 59, no. 7-8, p. 433-442, **DOI:10.5545/sv-jme.2012.911**.

[7] Minav, T., Sinkkonen, A., Hänninen, H., Laurila, L., Pyrhönen, J. (2014). Energy recovery system comparison of reach truck. *Strojniški vestnik - Journal of Mechanical Engineering*, vol. 60, no. 4, p. 232-240, **DOI:10.5545/sv-jme.2013.1581**.

[8] Andersen, T., Hansen, M., Pedersen, H. (2005). Regeneration of Potential Energy in Hydraulic Forklift Trucks. *Proceedings of the 6th International Conference on Fluid Power Transmission and Control*.

[9] Minav, T., Laurila L., Pyrhönen J., Vtorov V.,(2011). Direct pump control effects on the energy efficiency in an electro-hydraulic lifting system. *Journal International Review of Automatic Control*, vol. 4, no. 2, p. 235-242.

[10] Ponomarev, P. (2013). *Tooth-Coil Permanent Magnet Synchronous Machine Design for Special Applications*. PhD thesis, Acta Universitatis Lappeenrantaensis 531, Lappeenranta University of Technology, Lappeenranta.

[11] Yamazaki, K., Fukushima, N. (2010). Iron-loss modeling for rotating machines: comparison between Bertotti's three-term expression and 3-D eddy-current analysis. *IEEE Transactions on Magnetics*, vol. 46, no. 8, p. 3121–3124, **DOI:10.1109/TMAG.2010.2044384**.

[12] Smeets, J.P.C., Soulard, J., Lomonova, E.A., (2010). Thermal analysis of a winding turn-to-turn fault in PM synchronous machine. *XIX International Conference on Electrical Machines*, Rome, p. 1–6, **DOI:10.1109/ICELMACH.2010.5608010**.

[13] Sim, J.H. Chai, S.H., Kim, D.M., Hong, J.P. (2013). Temperature prediction of oil-cooled IPMSM for in-wheel direct-drive through lumped parameter thermal model. *International Conference on Electrical Machines and Systems*, Busan, p. 134-138, **DOI:10.1109/ICEMS.2013.6754540**.

[14] Ponomarev, P., Polikarpova, M., Pyrhonen, J. (2012). Conjugated fluid-solid heat transfer modeling of a directly-oil-cooled PMSM using CFD. *International Symposium on Power Electronics, Electrical Drives, Automation and Motion*, p. 141–145, **DOI:10.1109/SPEEDAM.2012.6264385**.

[15] Huang, Z., Nategh, S., Alakula, M., Lassila, V., Yuan, J. (2012) Direct Oil Cooling of Traction Motors in Hybrid Drives. *IEEE International Conference Electric Vehicle*, Greenville, p. 1–8, **DOI:10.1109/IEVC.2012.6183163**.

[16] Watton, J. (2009). Fundamentals of Fluid Power Control, Cambridge University Press, Cambridge, **DOI:10.1017/CBO9781139175241**.

[17] Ponomarev, P., Åman, R., Handroos, H., Immonen, P., Pyrhonen, J., Laurila, L. (2014). High power density integrated electro-hydraulic energy converter for heavy hybrid off-highway working vehicles. *IET Electrical Systems in Transportation*, vol. 4, no. 4, p. 114-121, **DOI:10.1049/iet-est.2013.0009**.

[18] Exxon Mobil Corporation (2014). Mobil Pyrotec HFD 46 Fire-Resistant Hydraulic Fluid, from: *http://www.mobil.com/USA-English/Lubes/PDS/GLXXENINDMOMobil_Pyrotec_HFD_46.aspx*, accessed on 2014-10-08.

[19] KRACHT GmbH. (2014). Gear Type Flow Meter VC, from *http://kracht.eu/uploads/tx_ttproducts/datasheet/VC_GB_01-12_01.pdf*, accessed on 2014-10-08.

Vsebina

Strojniški vestnik - Journal of Mechanical Engineering
letnik 61, (2015), številka 3
Ljubljana, marec 2015
ISSN 0039-2480

Izhaja mesečno

Razširjeni povzetki

Strojniški vestnik - Journal of Mechanical Engineering 61(2015)3, SI 31

Prejeto v recenzijo: 2014-05-26
Prejeto popravljeno: 2014-09-15
Odobreno za objavo: 2015-01-06

Vpliv debeline stene surovca na proces rotacijskega stiskanja votlih delov

Janusz Tomczak* – Tomasz Bulzak – Zbigniew Pater
Tehniška univerza v Lublinu, Fakulteta za strojništvo, Poljska

Votle dele, kot so gredi spremenljivega premera in osi, je mogoče izdelovati z različnimi postopki preoblikovanja kovin, med katerimi so najbolj priljubljeni rotacijsko kovanje, ekstrudiranje, hidroforming, potisno preoblikovanje in rotacijsko ekstrudiranje. Rotacijsko stiskanje je inovativna tehnologija preoblikovanja za izdelavo votlih kovinskih delov, ki je bila razvita na Tehniški univerzi v Lublinu.

V procesu rotacijskega stiskanja sodelujejo trije valji, ki se ne le vrtijo, temveč se tudi premikajo proti osi obdelovanca. Kot surovci pri rotacijskem stiskanju se uporabljajo kosi komercialnih cevi ali tulcev, ki se vrtijo in obenem tanjšajo pod vplivom delovne površine orodij. Premer obdelovanca se tako postopoma zmanjšuje. Rotacijsko stiskanje ima svoje mesto v industriji zaradi preproste zasnove procesa in primernosti za avtomatizacijo.

Postopek rotacijskega stiskanja za izdelavo votlih delov je nova in danes še ne dovolj preučena tehnologija preoblikovanja kovin. Zato so upravičene numerične in eksperimentalne raziskave za opredelitev razmerij med posameznimi parametri rotacijskega stiskanja in kakovostjo votlih izdelkov. V članku je predstavljen vpliv začetne debeline stene obdelovanca na rotacijsko stiskanje in kakovost izdelka. Kot surovci v numeričnih simulacijah in eksperimentalnih preizkusih so bili uporabljeni kosi cevi. Zunanji premer cevi D je bil 42,4 mm, debelina stene t_o pa 3, 5, 7, 9 in 11 mm. Numerična analiza je bila opravljena po metodi končnih elementov s programsko opremo za simulacije Simufact Forming, različica 12.0. Numerični rezultati so bili nato verificirani z laboratorijskimi preizkusi v laboratorijskih pogojih. Preizkusi so bili opravljeni na kovaškem stroju, ki je bil zasnovan in izdelan na oddelku za računalniško modeliranje in preoblikovanje kovin na Tehniški univerzi v Lublinu.

V raziskavi je bil ugotavljan vpliv začetne debeline stene obdelovanca na porazdelitev napetosti, temperatur, navor in obremenitve. Na podlagi rezultatov smo lahko opredelili vpliv začetne debeline obdelovanca na spremenljivost debeline in dolžine stene, pri čemer je zmanjšanje premera na prehodu ostalo konstantno $d = D/d = 1{,}5$ (kjer je D zunanji premer obdelovanca in d zunanji premer na prehodu). Z analizo geometrije narejenih delov je bilo mogoče ugotoviti, da zmanjšanje zunanjega premera vpliva na debelino stene obdelovanca in na dolžino. V večini primerov smo opazili povečanje debeline stene na oblikovanem prehodu, le pri obdelovancu z začetno debelino $t_o = 11$ mm se je ta parameter med rotacijskim stiskanjem zmanjšal. Poudariti pa je treba, da se relativno povečanje debeline stene na oblikovanem vratu (v primerjavi z začetno debelino) zmanjšuje s povečevanjem začetne debeline stene obdelovanca. Obraten trend je viden pri dolžini obdelovanca, kjer večja začetna debelina stene povzroči podaljšanje dela. Deli, narejeni po postopku rotacijskega stiskanja, imajo značilno neenakomerno porazdelitev napetosti: večja kot je začetna debelina stene obdelovanca, bolj neenakomerna je porazdelitev napetosti. Postopek rotacijskega stiskanja je lahko zahtevnejši pri oblikovanju delov z debelino stene pod 5 mm. Vzrok je v tem, da je material pri manjši debelini stene bolj nagnjen k hitremu ohlajevanju med procesom preoblikovanja.

Prihodnje študije rotacijskega stiskanja bi morale biti usmerjene v preučevanje pojavov, ki lahko prekinejo stabilnost procesa. Smiselne bi bile tudi raziskave za ugotavljanje povezav med tehnološkimi parametri procesa in geometrijo obdelovanca.

Ključne besede: rotacijsko stiskanje, votli deli, votle gredi, preoblikovanje kovine, metoda končnih elementov, eksperiment

*Naslov avtorja za dopisovanje: Tehniška univerza v Lublinu, Fakulteta za strojništvo, 36 Nadbystrzycka Str., 20-618 Lublin, Poljska, j.tomczak@pollub.pl

Strojniški vestnik - Journal of Mechanical Engineering 61(2015)3, SI 32

Prejeto v recenzijo: 2014-07-08
Prejeto popravljeno: 2014-11-26
Odobreno za objavo: 2014-12-10

Raziskava vpliva različnih geometrij robov orodja na obdelavo s simulacijo po metodi končnih elementov

Lei Wan – Dazhong Wang* –Yayun Gao
Kolidž za strojništvo, Tehniška univerza v Šanghaju, Kitajska

Namen raziskave je opredelitev vplivov različnih geometrij rezalnega roba orodja na proces odrezavanja, kamor spadajo npr. nabiranje materiala obdelovanca pod posnetim robom (območje mrtve kovine), porazdelitev napetosti in temperature pri štirih različnih geometrijah roba, in še posebej porazdelitev preostalih napetosti, ki lahko odraža kakovost obdelane površine. Rezultati raziskave lahko pomagajo pri iskanju pravega roba za obdelavo določenega materiala.

Najprej je predlagan nov analitični model in nato so analizirani postopki odrezavanja z različnimi geometrijami robov. V drugi fazi je bila uporabljena metoda končnih elementov za simulacijo procesa odrezavanja z različnimi geometrijami rezalnega roba pri različnih rezalnih hitrostih, rezultat pa je porazdelitev hitrosti, napetosti in temperature. Končno so bili opravljeni še eksperimenti z različnim kotom posnetja pri različnih rezalnih hitrostih za validacijo rezultatov simulacije.

Uporabljen je bil pristop z naslednjimi koraki: teoretična analiza, simulacija po metodi končnih elementov, validacija eksperimenta. Po analitičnem modelu je bil pripravljen model iz končnih elementov in uporabljen za simulacijo procesa odrezavanja. Rezultati eksperimentov so bili uporabljeni za validacijo simulacij. Tematika članka se uvršča v področje proizvodnje, preoblikovanja kovin in analize po metodi končnih elementov.

Rezultati simulacije kažejo, da ima geometrija roba manjši vpliv na proces oblikovanja odrezka, ker se pod posnetim robom, dvojnim posnetim robom in topim robom nabere material obdelovanca (mrtvo območje), ki podobno kot pri ostrem orodju deluje kot glavni rezalni rob orodja. Vedenje in oblika kovine v mrtvem območju sta preučena z vidika porazdelitve hitrosti materiala in napetosti. Vpliv geometrije na porazdelitev preostalih napetosti kaže, da imajo orodja z enojnim in dvojnim posnetjem praktično enak vpliv na porazdelitev napetosti kot pri brušenem in ostrem orodju. Jasno je, da je sila v smeri podajanja bolj odvisna od geometrije orodja in rezalne hitrosti kot sila v smeri rezanja. Sile se povečujejo s povečevanjem kota posnetja in zmanjšujejo z zmanjševanjem rezalne hitrosti. Geometrija rezalnega roba ima majhen vpliv na sile pri obdelavi, ko je rezalna hitrost zelo velika.

Prihodnje raziskave na tem področju se lahko posvetijo 3D-simulaciji procesa odrezavanja po metodi končnih elementov za jasnejšo predstavitev obrabe boka orodja ter celovito analizo obrabe orodja. Visokohitrostno odrezavanje je prikladno za analizo procesov odrezavanja z različnimi geometrijami rezalnega roba, ker se spremeni mehanizem oblikovanja odrezkov in je njegov vpliv na različne rezalne robove drugačen. Omejitve, ki so bile ugotovljene pri raziskavah, vključujejo natančnost simulacije po metodi končnih elementov in eksperimentalne napake, ki lahko privedejo do napačnih rezultatov. Simulacija namreč predstavlja idealen primer, medtem ko se v realnem procesu odrezavanja ni mogoče izogniti eksperimentalnim napakam zaradi nenadnih vibracij ipd. Zato je pomemben tudi pravilen pristop k simulaciji procesa odrezavanja, ki je ustreznejši za realen proces.

Prispevek, novosti, vrednost: Novost predstavljenega članka z ozirom na obstoječe vire s tega področja je v novem analitičnem modelu, ki upošteva štiri glavne geometrije robov orodja in je uporaben za analizo porazdelitve preostalih napetosti in oblikovanja območja mrtve kovine. Članek je lahko v pomoč in vodilo pri izbiri primerne geometrije roba orodja za odrezavanje danega materiala pri določeni rezalni hitrosti tako, da bosta porabljena energija in obraba najmanjši, kakovost obdelane površine pa najboljša.

Ključne besede: proces odrezavanja, metoda končnih elementov, nabiranje materiala pod posnetim robom, geometrija roba orodja, učinek toplotnega mehčanja, deformacijsko utrjanje, preostale napetosti

*Naslov avtorja za dopisovanje: Kolidž za strojništvo, Tehniška univerza v Šanghaju, Kitajska, wdzh168@hotmail.com

Strojniški vestnik - Journal of Mechanical Engineering 61(2015)3, SI 33

Prejeto v recenzijo: 2014-11-11
Prejeto popravljeno: 2015-01-16
Odobreno za objavo: 2015-01-29

Deterministično matematično modeliranje degradacije zmogljivosti platforme v režimih cikličnega obratovanja

Nenad Kapor[1] – Momcilo Milinovic[1]* – Olivera Jeremic[1] – Dalibor Petrovic[2]

[1]Univerza v Beogradu, Fakulteta za strojništvo, Beograd, Srbija
[2]Univerza za obrambo, Vojaška akademija, Srbija

Na področju strojev za obdelavo površin trenutno ne obstaja poenoten teoretični model za povezovanje spremenljive zmogljivosti strojev v cikličnih delovnih procesih, ki se izkazujejo v vplivu na kontinuirno obdelane površine. Modeliranje v operacijskih raziskavah ponuja določene modele medsebojnih odvisnosti med dvema matematično neodvisnima objektoma. V teh modelih pa ni obravnavan samo en objekt oz. stroj za obdelavo površin kot delovna platforma, ki delovne operacije izvaja ciklično in zaradi vpliva ponavljajočih se ciklov samodegradira. V zasnovanem modelu je bilo privzeta hipoteza, da platforma samodegradira, hitrost degradacije pa je spremenljiva in sorazmerna z realno hitrostjo izvajanja operacij, zmanjšana za tekoče število preostalih neizvedenih operacij z razpoložljivo kapaciteto. Ti vplivi se merijo z določanjem statistične variabilnosti parametrov obdelovane površine.

Glavni cilj članka je ovrednotenje samodegradacije zmogljivosti platforme zaradi vpliva ponavljajočih se ciklov. Projektirane frekvence in funkcijske verjetnosti, ki so vsebovane v vsaki delovni operaciji, se odražajo na kakovosti obdelovanih površin kot funkcija polne kapacitete razpoložljivih operacij na platformi. Predlagani model je zato uporaben pri načrtovanju in spreminjanju kapacitet platforme, kakor tudi pri zahtevah za obdelavo površine. Model, ki je predstavljen v tem članku, je podoben modelom ranljivosti bojnih platform na osnovi koeficienta izgub, ki posredno opisujejo pričakovano degradacijo delovnih zmogljivosti.

Deterministično modeliranje na podlagi osnovnih enačb Lanchestra in Dinnerja je tukaj posplošeno z vsebovano povezavo med parametri. Na novo razviti matematični model degradacije zmogljivosti se dobro ujema tako z eksperimentalnimi meritvami kot z numeričnimi simulacijami. Predpostavljeno je, da so nove spremenljivke in njihove korelacije povezane z zabeleženo zmogljivostjo preizkusnih platform z Gaussovo porazdelitvijo. Relativni raztros verjetnosti parametrov obdelane površine je prevzet kot nova veličina, ki opisuje obdelovano površino, s tem pa postane novo posredno merilo za učinkovitost platforme. Ti raztrosi verjetnosti so bili uporabljeni v novem modelu za simulacije in primerjave z eksperimentalnimi podatki. Razlike med relativnimi vrednostmi obdelovanih površin pri degradiranih in nedegradiranih platformah so bile preračunane na dimenzije novih ustreznih obdelanih površin. Srednji raztros verjetnosti PDav kot merilo degradacije površine je določen eksperimentalno in s simulacijo. Model potrjuje hipotezo, da je učinek degradacije funkcija kapacitete platforme, frekvence izvajanja operacij in števila razpoložljivih ciklov. Vpliv degradacije je v preračunu upoštevan z ekvivalentnim zmanjšanjem števila operacij s polno kapaciteto, ki se odraža na lastnostih obdelanih površin.

Predstavljeni rezultati kažejo tudi nasičenje relativne degradacije, vendar pri vsaj 40 operacijah. Te vrednosti so enakega velikostnega reda kot pri testih drugih avtorjev na podobnih strojih.

Simulacije so bile opravljene s programskim paketom MATLAB in njihovi rezultati so bili primerjani z rezultati eksperimentov. Pri simulacijah sta bili uporabljeni naslednji osnovni predpostavki:

- Predstavljene zmogljivosti platforme, kot sta kapaciteta operacij in število operacij, so bile uporabljene za eksperimentalno modeliranje. Ti podatki so bili uporabljeni pri modeliranju degradacije platforme.
- Numerični in eksperimentalni podatki so potrdili model degradacije za več platform z različnimi seti kapacitet operacij. Privzeto je bilo, da ima en cikel 8 operacij in da se izvede v nazivnem času 4,4 sekunde.

Novost predstavljenega pristopa je v uporabi prilagojenih determinističnih enačb, ki so povezane na inovativen način. Te enačbe so v literaturi uporabljene za opis medsebojnih vplivov objektov kot funkcije časa izvajanja procesa. Časovna funkcija je po pristopu v literaturi odvisna od zmogljivosti obeh objektov. V našem pristopu pa en objekt vzporedno izvaja dve operaciji: ena je sam delovni proces, druga, parazitna, pa je samodegradacija v odvisnosti od delovnega procesa. Novi pristop povezuje deterministične enačbe za opis tega pojava in merjenje sprememb učinkovitosti platforme.

Nadaljnje raziskave na tem področju se lahko usmerijo v razširitev eksperimentalnih podatkov za izpopolnitev simulacijskega modela ustrezno vrsti specialnih strojev in obdelovanim površinam.

Ključne besede: cikli, operacije, specialni stroji, verjetnost, deterministično modeliranje

*Naslov avtorja za dopisovanje: Univerza v Beogradu, Fakulteta za strojništvo, Kraljice Marije 16, 11000 Beograd, Srbija, mmilinovic@mas.bg.ac.rs

Strojniški vestnik - Journal of Mechanical Engineering 61(2015)3, SI 34

Prejeto v recenzijo: 2014-04-22
Prejeto popravljeno: 2014-07-25
Odobreno za objavo: 2014-10-22

Izbira optimalnih parametrov procesa visokohitrostnega CNC-rezkanja kompozitnih materialov z metahevrističnimi tehnikami – primerjalna študija

Vikas Pare – Geeta Agnihotri – Chimata Krishna*
Nacionalni institut za tehnologijo Maulane Azada, Bhopal, Indija

Visokohitrostna CNC-obdelava kompozitnih materialov z aluminijastim matriksom je pomembna za letalsko in vesoljsko industrijo. Letalska in vesoljska industrija zahteva visoko kakovost in napovedovanje površinske hrapavosti na podlagi vhodnih parametrov procesa je pomembno za zagotavljanje kakovosti izdelkov. Veliko raziskovalcev se ukvarja s konvencionalno obdelavo, le malo pa se jih je lotilo tehnik optimizacije na področju visokohitrostnih obdelav, kot so npr. optimizacija na osnovi poučevanja in učenja (TLBO) ter gravitacijski iskalni algoritmi (GSA). Namen tega raziskovalnega članka je modeliranje odvisnosti med površinsko hrapavostjo in izbranimi vhodnimi parametri, optimizacija površinske hrapavosti z mehkimi računskimi tehnikami kot so GSA, TLBO, SA in GA, primerjava rezultatov, kakor tudi verifikacija in validacija rezultatov iz prejšnjega koraka z izvedbo dodatnega nabora eksperimentov.

Teoretični modeli ne dajejo nujno dobrih rezultatov pri vsakih eksperimentalnih pogojih. Pristopi s poskusi in napakami, kot jih uporablja stroj, niso produktivni in porabijo tudi zelo veliko časa. Z opredelitvijo empiričnih odvisnosti med izhodnimi parametri kot je površinska hrapavost in vhodnimi procesnimi parametri, ki ji sledi optimizacija izhodnih parametrov, je mogoče dobiti razmeroma točne rezultate visokohitrostne obdelave. Razvoj učinkovitih in usmerjenih tehnik optimizacije je nujen, saj konvencionalni pristopi niso primerni za kompleksnejše modele. Mehke računske tehnike so primerne za kompleksne modele in morajo biti uporabljene v tem kontekstu.

Metodologija vključuje naslednje korake:

1. korak: izbira prave kombinacije kompozitnega materiala, rezalnih orodij in opreme,
2. korak: zbiranje podatkov z izvedbo eksperimentov po opredeljenem načrtu,
3. korak: postavitev modela za napovedovanje površinske hrapavosti in
4. korak: optimizacija prediktivnega modela za boljše rezultate.

To raziskovalno delo bo proizvajalcem pomagalo pri izbiranju primernih parametrov procesa za zmanjšanje površinske hrapavosti in povečanje kakovosti končnega izdelka.

Uporabljene so bile štiri optimizacijske tehnike za iskanje optimalne vrednosti površinske hrapavosti in podana je primerjava rezultatov. Izbor rezultatov je prikazan v Preglednici 6. Rezultati, pridobljeni s štirimi izbranimi tehnikami, razkrivajo, da je treba za boljšo površinsko hrapavost aluminijaste površine izbrati višjo hitrost. Vrednost podajanja se je spreminjala od 101,56 do 192,3 μm/obr.: le ena vrednost je bila blizu vrednosti 200 μm/obr. in ostale tri vrednosti so bile blizu 100 μm/rev. Sledi zaključek, da je za minimalno površinsko hrapavost zaželeno majhno podajanje. Kar se tiče globine reza, so bile tri vrednosti blizu 0,2 mm in iz tega sledi, da je za minimalno površinsko hrapavost zaželena majhna globina reza. Del premera rezkarja, ki sodeluje pri obdelavi, se je spreminjal od 0,5 do 0,6: tri vrednosti so blizu 0,5, četrta pa je blizu 0,6. Število iteracij je bilo večje pri algoritmih SA in GSA, zato je mogoče sklepati, da je za nadaljnje delo zaželena vrednost deleža 0,5.

Največja hitrost v tej študiji je bila 6000 obr./min, visokohitrostni CNC-stroji pa obratujejo tudi z veliko večjimi hitrostmi. Študijo bi bilo mogoče še razširiti z dodatnimi vhodnimi parametri v večjem območju vrednosti za napovedovanje površinske hrapavosti. Modeli ne upoštevajo vplivov interakcij, ki lahko postanejo predmet prihodnjih raziskav. V pogojih visokohitrostne obdelave bi bilo treba raziskati tudi več kompozitnih materialov z različnimi kombinacijami sestavnih materialov, s čimer bi omogočili izračun optimalnih pogojev obdelave za boljšo pripravo proizvodnih postopkov.

Mikrostruktura in materialne lastnosti kompozita AlSiC so dobro preučene. Ta material je bil obdelan na visokohitrostnem CNC-stroju za ugotavljanje optimalnih vrednosti vhodnih parametrov v območju vrtilnih hitrosti do 6000 obr./min. Za optimizacijo površinske hrapavosti komponent so bile uporabljene optimizacijske tehnike kot sta gravitacijski iskalni algoritem ter optimizacija na osnovi poučevanja in učenja.

Ključne besede: visokohitrostna obdelava, kompozit s kovinskim matriksom, površinska hrapavost, gravitacijski iskalni algoritmi, optimizacija na osnovi poučevanja in učenja

*Naslov avtorja za dopisovanje: Nacionalni institut za tehnologijo Maulane Azada, Bhopal, Indija, 462051, cmk_manit@rediffmail.com

Strojniški vestnik - Journal of Mechanical Engineering 61(2015)3, SI 35

Prejeto v recenzijo: 2014-09-30
Prejeto popravljeno: 2014-12-16
Odobreno za objavo: 2015-01-06

Adaptivna mehko-PI-regulacija za sistem aktivnega sprednjega krmiljenja oklepnega vozila: zasnova zunanje krmilne zanke za sistem streljanja med gibanjem

Zulkiffli Abd Kadir*,[1] – Saiful Amri Mazlan[2] – Hairi Zamzuri[2] – Khisbullah Hudha[1] – Noor Hafizah Amer[1]

[1]Tehniška fakulteta, Malezijska nacionalna univerza za obrambo, Malezija
[2]Malezijsko-japonski mednarodni inštitut za tehnologijo, Tehniška univerza v Maleziji, Maleziji

Oklepna vozila pri streljanju med gibanjem izgubijo svojo dinamično mobilnost. Vzrok za to je vpliv reakcijske sile pri streljanju v središču oborožitvene platforme, ki v težišču oklepnika povzroči nezaželen moment vrtenja okrog navpične osi. Z namenom izboljšanja mobilnih lastnosti oklepnika je bila na podlagi validiranega modela oklepnika zasnovana strategija regulacije za kompenzacijo vrtenja okrog navpične osi. Cilj te strategije regulacije je ohranitev smerne mobilnosti oklepnika s korekturo krmilnega kota, ki se uveljavi prek vzvodov krmilnega sistema koles. Predlagana strategija regulacije je sestavljena iz dveh delov: povratnozančne regulacije vrtenja okrog navpične osi s pomočjo proporcionalno-integralno-diferencialnega (PID) regulatorja in regulacije za kompenzacijo bočne sile (LFRC) s pomočjo adaptivnega mehko-proporcionalno-integralnega (adaptivnega mehko-PI) regulatorja. Predlagana je strategija regulacije sistema za kompenzacijo vrtenja okrog navpične osi za oklepnike z aktivnim sprednjim krmiljenjem (AFS). Predlagana strategija regulacije za kompenzacijo vrtenja okrog navpične osi je razvita na podlagi modela štirikolesnega oklepnika. Model štirikolesnega oklepnika je bil validiran s pomočjo eksperimentalnega modela oklepnika, ki predstavlja dejansko vedenje oklepnika. Na podlagi validiranega modela oklepnika je v študiji predlagana strategija regulacije sistema aktivnega sprednjega krmiljenja. Sestavljena je iz dveh regulatorjev zunanje zanke za hitrost vrtenja okrog navpične osi in bočno silo. Namen snovanja regulatorjev zunanjih zank je zmanjšanje velikosti nezaželenega gibanja v bočni smeri z zmanjševanjem vrtenja okrog navpične osi in bočnega gibanja zaradi streljanja. Predlagana regulatorja zunanje zanke za vrtenje okrog navpične osi in bočno silo sta bila razvita na podlagi proporcionalno-integralno-diferencialne (PID) in mehko-PI strategije regulacije. Predlagana strategija adaptivne mehko-propocionalno-integralne (mehko-PI) regulacije je nato primerjana s splošno mehko-PI regulacijo in s konvencionalno proporcionalno-integralno (PI) regulacijo za oceno učinkovitosti adaptivne mehko-PI regulacije.

Strategija regulacije za oklepnik s sistemom AFS je bila razvita na podlagi validiranega modela štirikolesnega oklepnika s pomočjo paketa MATLAB-SIMULINK. Glavni namen predlagane strategije regulacije je izboljšanje dinamičnih lastnosti oklepnika, npr. bočnega odmika, hitrosti vrtenja okrog navpične osi in kota vrtenja okrog navpične osi pri streljanju med gibanjem. V študiji sta bila uporabljena dva povratnozančna regulatorja: prvi PID za hitrost vrtenja okrog navpične osi in drugi mehko-PI za bočno silo. Predlagana strategija regulacije AFS je nato bila ovrednotena s simulacijo pri različnih kotih streljanja 30, 60 in 90 °. Rezultati simulacije kažejo, da se predlagana strategija regulacije AFS z adaptivnim mehko-PI-regulatorjem v primerjavi z mehko-PI regulatorjem in konvencionalnim PI-regulatorjem odreže bistveno bolje. V študiji je predlagana strategija regulacije, razvita na podlagi validiranega modela oklepnika, pri čemer sistem ni implementiran v realnočasovni proces. Prihodnje raziskave bi se lahko posvetile implementaciji predlagane strategije regulacije v realnočasovno simulacijo strojne opreme v zanki (HIL). Za vrednotenje učinkovitosti oklepnega vozila med streljanjem bosta razvita in preizkušena vzvodni krmilni mehanizem in izvršni člen za AFS. Predlagana strategija mehko-PI-regulacije bo uporabljena za preučitev odgovora oklepnika za kompenzacijo neželenih motenj pri streljanju.

Novost, ki je predstavljena v tem članku, je sposobnost streljanja oklepnika med gibanjem brez izgube smerne stabilnosti. V vozilu je bil implementiran sistem aktivnega krmiljenja sprednjih koles (AFS) za analizo vedenja oklepnika med streljanjem. Sistem AFS je običajno vgrajen v potniških vozilih in kompenzira zunanje motnje zaradi sile vetra. V tej študiji je bil enak koncept uporabljen pri oklepniku za kompenzacijo nezaželenega vrtenja okrog navpične osi med streljanjem, pri čemer je sila udarca večja od sile bočnega vetra. Predlagan je hibridni adaptivni mehko-PI-mehanizem regulacije za izboljšanje vedenja oklepnika med streljanjem. Predlagana strategija regulacije bistveno izboljša vedenje oklepnika v primerjavi s pasivnim oklepnikom.

Ključne besede: model oklepnika, validacija modela oklepnika, aktivno sprednje krmiljenje, streljanje med gibanjem, adaptivna mehka regulacija, regulacija bočne sile

*Naslov avtorja za dopisovanje: Tehniška fakulteta, Malezijska nacionalna univerza za obrambo, Malezija, zulkiffli@upnm.edu.my

Strojniški vestnik - Journal of Mechanical Engineering 61(2015)3, SI 36

Prejeto v recenzijo: 2014-08-24
Prejeto popravljeno: 2014-10-26
Odobreno za objavo: 2014-11-03

Raziskava uporabe sistema za regeneracijo energije z akumulatorjem v opremi za preizkušanje hidravličnih impulzov

Zaipeng Man* – Fan Ding – Chuan Ding – Shuo Liu
Državni laboratorij za fluidno tehniko, Univerza v Zhejiangu, Kitajska

Preizkušanje hidravličnih komponent s hidravličnimi impulzi je ključnega pomena za zagotavljanje zanesljivosti in zmogljivosti hidravličnih sistemov. Čeprav so aplikacije ponovnega pridobivanja energije močno razširjene v industriji, pa je med njimi le malo takih, ki bi bile razvite za opremo za preizkušanje hidravličnih impulzov. Standardi določajo, da trajajo impulzni preizkusi do 280 ur, kar pa je energijsko potratno in zmanjšanje rabe energije za impulzne preizkuse je zato zelo pomembna naloga. Hidravlični akumulator lahko hitro shrani in sprosti energijo, zato predstavlja dobro rešitev za regeneracijo energije v opremi za preizkušanje hidravličnih impulzov, kjer so cikli običajno zelo kratki. V članku je podan predlog sistema za regeneracijo energije z akumulatorjem kot del opreme za preizkušanje hidravličnih impulzov.

Za analizo prednosti sistemov za regeneracijo energije s hidravličnim akumulatorjem v opremi za preizkušanje hidravličnih impulzov je bila narejena primerjava opreme za preizkušanje hidravličnih impulzov z akumulatorjem in brez njega, še posebej z vidika rabljene energije in učinkovitosti sistema. Postavljeni so bili matematični modeli za moč sistema, rabe energije in energijsko učinkovitost. V okolju AMESim so bili ustvarjeni modeli za simulacijo sistemov z in brez akumulatorja. Pri simulaciji je bil uporabljen vhod v obliki kvadratnega vala za analizo vedenja sistema v delih cikla s povečanjem tlaka oz. z vračanjem. Primerjava moči sistema, rabe energije ter učinkovitosti sistemov z akumulatorjem in brez njega je bila narejena na podlagi simulacije in izračunov. Rezultati kažejo, da lahko sistem za preizkušanje hidravličnih impulzov z akumulatorjem rabi do 15 % manj energije na cikel kot sistem brez akumulatorja. Energijski izkoristek sistema za preizkušanje hidravličnih impulzov se z vključitvijo akumulatorja poveča iz 62,86 na 75,71 %.

Za preučitev učinkovitosti krmiljenja sistema za regeneracijo energije z akumulatorjem v opremi za preizkušanje hidravličnih impulzov so bili opravljeni eksperimenti na prototipu. Narejena je primerjava zmogljivosti opreme z akumulatorjem in opreme brez akumulatorja. Preučen je odziv sistema za preizkušanje hidravličnih impulzov z akumulatorjem in brez njega na stopnico.

Rezultati kažejo, da oba sistema dosežeta cilj z minimalno napako po ustalitvi, sistem z akumulatorjem pa ta cilj doseže hitreje kot sistem brez akumulatorja, predvsem zahvaljujoč regeneraciji energije v akumulatorju. Za primerjavo učinkovitosti krmiljenja sistemov z akumulatorjem in brez njega so bile uporabljene najpogostejše oblike tlačnih valov pri opremi za preizkušanje hidravličnih impulzov, vključno s kvadratnimi in vršnimi valovi. Rezultati simulacij in eksperimentov kažejo, da je učinkovitost krmiljenja opreme za preizkušanje hidravličnih impulzov z akumulatorjem boljša od učinkovitosti opreme brez akumulatorja, tako z ozirom na hitrost odziva kot na hitrejši porast tlaka.

Inovacija v tej raziskavi je vpeljava sistema za regeneracijo energije z akumulatorjem v opremo za preizkušanje hidravličnih impulzov, ki predstavlja nov pristop k varčevanju z energijo v tovrstnih sistemih. Matematične analize in simulacije kažejo, da lahko sistem za preizkušanje hidravličnih impulzov z akumulatorjem zmanjša rabo energije in izboljša učinkovitost sistema. Tako rezultati simulacij kot rezultati eksperimentov dokazujejo, da je učinkovitost krmiljenja opreme za preizkušanje hidravličnih impulzov z akumulatorjem boljša kot pri opremi brez akumulatorja.

Ključne besede: preizkušanje hidravličnih impulzov, regeneracija energije, hidravlični akumulator, simulacija, eksperiment, shranjevanje energije

*Naslov avtorja za dopisovanje: Državni laboratorij za fluidno tehniko, Univerza v Zhejiangu, Hangzhou, Kitajska, manzaipeng@126.com

Strojniški vestnik - Journal of Mechanical Engineering 61(2015)3, SI 37

Prejeto v recenzijo: 2014-07-28
Prejeto popravljeno: 2014-11-21
Odobreno za objavo: 2014-12-18

Integrirani elektrohidravlični stroj z možnostjo samohlajenja za necestno mobilno mehanizacijo

Pavel Ponomarev[1] – Tatiana Minav[2] – Rafael Åman[3] – Lauri Luostarinen[3]

[1] Tehniška univerza v Lappeenranti, LUT Energija, Finska
[2] Univerza Aalto, Tehniška šola, Espoo, Finska
[3] Tehniška univerza v Lappeenranti, LUT Strojništvo, Finska

V zadnjih letih so se zaradi uvedbe zakonodaje o izpustih Tier 4 pojavile novosti na področju necestne mobilne mehanizacije (NRMM), ki omogočajo doseganje teh strogih ciljev. V članku je predstavljen koncept zasnove samohlajenja integriranih elektrohidravličnih strojev za uporabo v NRMM. Uporabnost koncepta je prikazana na primeru integriranega elektrohidravličnega pretvornika energije (IEHEC). V članku sta predstavljena dva pristopa k hlajenju (pasivni in aktivni) električnih strojev za necestno mobilno mehanizacijo. Prvi pristop dodatno moč, ki je potrebna za hlajenje, zmanjšuje z uporabo lekažnega toka iz ohišja hidravlične opreme pod obremenitvijo, drugi pristop pa za vzdrževanje optimalnega toplotnega režima strojev uporablja krmiljeno ojačevalno črpalko. Prvi pristop je podrobneje analiziran za preverjanje, ali je pasivno hlajenje sposobno vzdrževanja temperaturnih omejitev stroja.

Namen te študije je prikaz primernosti koncepta samohlajenja integriranih elektrohidravličnih strojev za hibridne/električne aplikacije NRMM. Za ugotavljanje praktične uporabnosti pristopa je bil lekažni tok iz ohišja IEHEC izmerjen v vrsti delovnih točk znotraj celotnega delovnega območja. Meritve so bile opravljene s poganjanjem hidravličnega kroga v različnih delovnih točkah. Lekažni tok med delovanjem (v načinu motorja in generatorja) je bil izmerjen z merilnikom pretoka. Dvig temperature v vsaki delovni točki je bil izračunan v sklopu toplotne analize. Ob upoštevanju dejstva, da ima električni stroj v različnih delovnih točkah različne izgube, postane jasno, da obstajata dve območji: tam, kjer so izgube pod zmogljivostjo hlajenja (območje varne uporabe električnega stroja), in tam, kjer zmogljivost hlajenja ne zadošča za kompenzacijo.

Predvideno območje uporabe IEHEC je po rezultatih raziskave znotraj dovoljenega območja za samohlajenje in elektrohidravlični stroj lahko varno obratuje brez dodatne moči za hlajenje. Kratkotrajno delovanje zunaj dovoljenega območja je lahko sprejemljivo, saj ima hladilni medij veliko toplotno kapaciteto. Odvečna toplota se lahko za krajši čas zadrži v komponentah stroja in v hladilnem mediju, ob predpostavki, da se delovna točka IEHEC kar se da hitro vrne v dovoljeno delovno območje.

Uporabljena merilna oprema omogoča samo meritve v območju nizkega obratovalnega tlaka pod 50 bar. Za prihodnje raziskave bi zato bilo treba odpraviti to omejitev merilne konfiguracije in dokazati, da je pasivno hlajenje uporabno tudi pri dolgotrajnejših delovnih ciklih.

Članek predstavlja novo metodo hlajenja elektrohidravličnih strojev z visoko gostoto momenta za uporabo v NRMM. Pasivni koncept samohlajenja omogoča zmanjšanje dodatnih komponent za hlajenje v NRMM. Rezultati kažejo, da je območje pasivnega samohlajenja IEHEC ob omenjenih predpostavkah sprejemljivo. Predlagani koncept samohlajenja omogoča zmanjšanje porabe energije ter izboljšanje izkoristka sistema v aplikacijah NRMM.
Ključne besede: fluidna tehnika, rekuperacija energije, hibridni prenosnik moči, hidravlična lekaža, izgube, hlajenje, učinkovitost, toplotni nadzor, necestna mobilna mehanizacija

*Naslov avtorja za dopisovanje: Univerza Aalto, Tehniška šola, Espoo, Finska, tatiana.minav@aalto.fi

Doktorske disertacije, znanstveno magistrsko delo, diplomske naloge

DOKTORSKE DISERTACIJE

Na Fakulteti za strojništvo Univerze v Ljubljani so obranili svojo doktorsko disertacijo:

- dne *3. februarja 2015* **Rok LACKO** z naslovom: »Uporaba vodikovih tehnologij za izrabo razpršenih obnovljivih virov energije« (mentor: prof. dr. Mihael Sekavčnik);

Hibridni energetski sistem z vodikovimi tehnologijami za izrabo obnovljivih virov energije lahko alternativno omogoča samozadostno preskrbo porabnikov z energijo. Namen pričujočega dela je numerična in eksperimentalna ocena izvedljivosti povsem samostojne preskrbe gospodinjstva z električno energijo in toploto ter primerjava z referenčnim in alternativnim načinom energijske preskrbe, vključno z analizo občutljivosti, kjer obravnavamo vpliv velikosti energetskega sistema (glede na število porabnikov, ki ga tvorijo) in njegovo geografsko lokacijo. V delu primerjamo energetski sistem, ki porablja fosilne in obnovljive vire energije s sistemom, ki izkorišča izključno obnovljive vire (energijo sončnega obsevanja in energijo vetra) s podporno vključitvijo vodikovih tehnologij. Za izvedbo modeliranja in numeričnih simulacij smo izbrali referenčno gospodinjstvo, ki je locirano na slovenski Obali. Pri obravnavi smo upoštevali geografsko lokacijo in razpoložljivost virov energije, dinamiko rabe energije in tehnično-ekonomske lastnosti sestavnih delov energetskega sistema. Rezultati kažejo, da je povsem (100 %) obnovljiva preskrba referenčnega gospodinjstva tehnično izvedljiva in ima manjše obratovalne stroške (za 660 EUR letno), kot sistemi na fosilna goriva. Povezovanje porabnikov v večje skupine omogoča manj dinamično obratovanje vodikovih tehnologij, kar se kaže s 5-kratnim povečanjem obremenitvenega faktorja in 80 % manjšo specifično nazivno močjo gorivne celice sistema 80-ih porabnikov v primerjavi z enim samim. Eksperimenti, z zgolj 3 % odstopanjem od numeričnih rezultatov, potrjujejo zmožnost alternativne uporabe obstoječih industrijskih vodikovih tehnologij za izravnavo rabe in proizvodnje energije.

- dne *27. februarja 2015* **Tine CENCIČ** z naslovom: »Diagnostika kavitacije v črpalni hidroelektrarni« (mentor: izr. prof. dr. Marko Hočevar, somentor: prof. dr. Branko Širok);

Narejena je bila eksperimentalna raziskava z namenom zaznavanja kavitacije, ki pri delovanju turbine v črpalnem režimu povzroča kavitacijsko erozijo. Kavitacijo v črpalnem režimu se je merilo s senzorji vibracij, akustično emisijo ter z visokofrekvenčnim tlačnim senzorjem. Raziskava je temeljila na analizi vsebnosti visokofrekvenčnih merjenih spremenljivk. Najboljši rezultati so bili doseženi z novo sestavljeno cenilko, ki je bila določena kot produkt RMS cenilke in kvadratne vrednosti pretočnega števila. V generatorskem režimu se je s tlačnimi in vibracijskimi senzorji analiziralo vpliv kavitacijskega vrtinca. V disertaciji je bila narejena primerjava med različnimi metodami merjenja kavitacijskih poškodb in izdelan model napredovanja kavitacijske erozije. Rezultati disertacije predstavljajo doprinos k napovedi rasti kavitacijskih poškodb na črpalnih turbinah.

- dne *27. februarja 2015* **Matej MILAVEC** z naslovom: »Turbulentna disipacija energije v elementih pretočnega trakta turbinskih strojev« (mentor: prof. dr. Branko Širok, somentor: izr. prof. dr. Marko Hočevar);

Predloženo delo obravnava aeromehanične in akustične pojave v špranji med vrhom lopatice in mirujočim ohišjem aksialnega ventilatorja. Podrobno so obdelane in primerjane razmere v toku zraka v zračni špranji za dve konstrukcijsko pomembno različni obliki temena rotorskih lopatic in njihov vpliv na aerodinamske ter akustične značilnosti ventilatorja. Poleg integralnih zvočnih in aerodinamskih karakteristik so bile opravljene podrobne analize lokalno izmerjenih časovnih vrst hitrosti in tlakov, njihovih varianc, ravni zvočnega tlaka in vizualizacije toka v špranji rotorja. Ugotovljene in pojasnjene so razmere in značilnosti, ki povezujejo emisijo hrupa ventilatorja s tokovnimi pojavi v špranji rotorja ventilatorja z nastankom, obliko, velikostjo ter razporeditvijo in velikostjo tokovnih struktur. Ugotovljena in potrjena so tudi mejna področja in značilne analitske oblike upada frekvenčnega spektra ravni zvočnega tlaka, s katerimi lahko na izviren način ugotovimo naravo in obseg generiranega hrupa ventilatorja in ne nazadnje vnaprej določimo umeščenost in splošno akustično primernost zasnove novega ventilatorja. Predstavljen in uporabljen je tudi izviren način določitve atraktorjev v energijskem polju toka v špranji ventilatorja, s katerimi lahko predvidimo ali pa potrdimo lokalni razvoj posebnih tokovnih pojavov in njihov vpliv na delovanje ter izsevano zvočno moč ventilatorja.

*

ZNANSTVENO MAGISTRSKO DELO

Na Fakulteti za strojništvo Univerze v Mariboru je z uspehom zagovarjal svoje magistrsko delo:

- dne *20. februarja 2015* **Marko LESKOVŠEK** z naslovom: »Upravljanje proizvodnje v podjetju z omejitvami pri zaposlenih« (mentor: prof. dr. Borut Buchmeister).

*

DIPLOMSKE NALOGE

Na Fakulteti za strojništvo Univerze v Mariboru sta pridobila naziv magister inženir strojništva:

dne 25. februarja 2015:

Jernej HRIBERNIK z naslovom: »Optimizacija zalog v podjetju X iz avtomobilske industrije« (mentor: doc. dr. Iztok Palčič);

Aleš ŽURGA z naslovom: »Potencial uporabe stisnjenega zemeljskega plina v prometu« (mentor: prof. dr. Aleš Hribernik).

*

Na Fakulteti za strojništvo Univerze v Ljubljani so pridobili naziv diplomirani inženir strojništva:

dne 4. februarja 2015:

Andrej BERNIK z naslovom: »Celovita avtomatizacija procesa struženja in vrtanja planetne gredi« (mentor: prof. dr. Janez Kopač);

Vojislav DIMITRIJEVIĆ z naslovom: »Označevanje rezanih komponent iz elektropločevine« (mentor: izr. prof. dr. Tomaž Pepelnjak);

Jan STANIČ z naslovom: »Temperatura kot kritična kontrolna točka v procesu pridelave hrane« (mentor: izr. prof. dr. Ivan Bajsić).

*

Na Fakulteti za strojništvo Univerze v Mariboru sta pridobila naziv diplomirani inženir strojništva (UN):

dne 26. februarja 2015:

Matjaž PRIŠENK z naslovom: »Modeliranje in analiza daljnovoda« (mentor: doc. dr. Boštjan Harl, somentor: izr. prof. dr. Marko Kegl, izr. prof. dr. Jožef Predan);

*

Na Fakulteti za strojništvo Univerze v Mariboru sta pridobila naziv diplomirani inženir strojništva:

dne 26. februarja 2015:

Primož GALUN z naslovom: »Analiza sposobnosti procesa valjanja na osnovi merjenja vibracij« (mentor: prof. dr. Bojan Ačko, somentor: doc. dr. Andrej Godina);

Stojan PISLAK z naslovom: »Predstavitev in analiza preoblikovalnega postopka pri izdelavi trgalnika papirja« (mentor: doc. dr. Mirko Ficko).

*

Na Fakulteti za strojništvo Univerze v Mariboru je pridobil naziv diplomirani inženir mehatronike (UN):

dne 26. februarja 2014:

Denis VINŠEK z naslovom: »Model reševalnega robota z ozirom na težišče« (izr. prof. dr. Karl Gotlih, somentor: doc. dr. Suzana Uran).

*

Na Fakulteti za strojništvo Univerze v Mariboru so pridobili naziv diplomirani inženir strojništva (VS):

dne 26. februarja 2015:

Aleks HEDL z naslovom: »Solarni kolektor za ogrevanje sanitarne vode« (mentor: prof. dr. Aleš Hribernik, somentor: asist. dr. Gorazd Bombek);

Marko HOZJAN z naslovom: »Konstruiranje elementov vertikalne vetrne turbine« (mentor: prof. dr. Srečko Glodež);

Primož SKUTNIK z naslovom: »Zasnova svečanega priznanja Ivana Munde« (mentor: izr. prof. Vojmir Pogačar, somentor: asist. Andrej Cupar);

dne 27. februarja 2015:

Anže RIBIČ z naslovom: »Numerična analiza zmogljivosti polžastega transporterja z uporabo metode DEM« (mentor: prof. dr. Iztok Potrč, somentor: izr. prof. dr. Tone Lerher).

*

Na Fakulteti za strojništvo Univerze v Mariboru so pridobili naziv diplomirani inženir mehatronike (VS):

dne 26. februarja 2015:

Davorin FRIM z naslovom: »Posodobitev krmilja na lesnem skobeljnem stroju« (mentor: izr. prof. dr. Darko Lovrec, somentorja: asist. dr. Vito Tič, viš. pred. mag. Janez Pogorelc).

Information for Authors

All manuscripts must be in English. Pages should be numbered sequentially. The manuscript should be composed in accordance with the Article Template given above. The maximum length of contributions is 10 pages. Longer contributions will only be accepted if authors provide juastification in a cover letter. For full instructions see the Information for Authors section on the journal's website: http://en.sv-jme.eu .

SUBMISSION:

Submission to SV-JME is made with the implicit understanding that neither the manuscript nor the essence of its content has been published previously either in whole or in part and that it is not being considered for publication elsewhere. All the listed authors should have agreed on the content and the corresponding (submitting) author is responsible for having ensured that this agreement has been reached. The acceptance of an article is based entirely on its scientific merit, as judged by peer review. Scientific articles comprising simulations only will not be accepted for publication; simulations must be accompanied by experimental results carried out to confirm or deny the accuracy of the simulation. Every manuscript submitted to the SV-JME undergoes a peer-review process.

The authors are kindly invited to submit the paper through our web site: http://ojs.sv-jme.eu. The Author is able to track the submission through the editorial process - as well as participate in the copyediting and proofreading of submissions accepted for publication - by logging in, and using the username and password provided.

SUBMISSION CONTENT:

The typical submission material consists of:

- A **manuscript** (A PDF file, with title, all authors with affiliations, abstract, keywords, highlights, inserted figures and tables and references),
- Supplementary files:
  - a **manuscript** in a WORD file format
  - a **cover letter** (please see instructions for composing the cover letter)
  - a ZIP file containing **figures** in high resolution in one of the graphical formats (please see instructions for preparing the figure files)
  - possible **appendicies** (optional), cover materials, video materials, etc.

Incomplete or improperly prepared submissions will be rejected with explanatory comments provided. In this case we will kindly ask the authors to carefully read the Information for Authors and to resubmit their manuscripts taking into consideration our comments.

COVER LETTER INSTRUCTIONS:

Please add a **cover letter** stating the following information about the submitted paper:

1. Paper **title**, list of **authors** and their **affiliations**.
2. **Type of paper**: original scientific paper (1.01), review scientific paper (1.02) or short scientific paper (1.03).
3. A **declaration** that neither the manuscript nor the essence of its content has been published in whole or in part previously and that it is not being considered for publication elsewhere.
4. State the **value of the paper** or its practical, theoretical and scientific implications. What is new in the paper with respect to the state-of-the-art in the published papers? Do not repeat the content of your abstract for this purpose.
5. We kindly ask you to suggest at least two **reviewers** for your paper and give us their names, their full affiliation and contact information, and their scientific research interest. The suggested reviewers should have at least two relevant references (with an impact factor) to the scientific field concerned; they should not be from the same country as the authors and should have no close connection with the authors.

FORMAT OF THE MANUSCRIPT:

The manuscript should be composed in accordance with the Article Template. The manuscript should be written in the following format:

- A **Title** that adequately describes the content of the manuscript.
- A list of **Authors** and their **affiliations**.
- An **Abstract** that should not exceed 250 words. The Abstract should state the principal objectives and the scope of the investigation, as well as the methodology employed. It should summarize the results and state the principal conclusions.
- 4 to 6 significant **key words** should follow the abstract to aid indexing.
- 4 to 6 **highlights;** a short collection of bullet points that convey the core findings and provide readers with a quick textual overview of the article. These four to six bullet points should describe the essence of the research (e.g. results or conclusions) and highlight what is distinctive about it.
- An **Introduction** that should provide a review of recent literature and sufficient background information to allow the results of the article to be understood and evaluated.
- A **Methods** section detailing the theoretical or experimental methods used.
- An **Experimental section** that should provide details of the experimental set-up and the methods used to obtain the results.
- A **Results** section that should clearly and concisely present the data, using figures and tables where appropriate.
- A **Discussion** section that should describe the relationships and generalizations shown by the results and discuss the significance of the results, making comparisons with previously published work. (It may be appropriate to combine the Results and Discussion sections into a single section to improve clarity.)
- A **Conclusions** section that should present one or more conclusions drawn from the results and subsequent discussion and should not duplicate the Abstract.
- **Acknowledgement** (optional) of collaboration or preparation assistance may be included. Please note the source of funding for the research.
- **Nomenclature** (optional). Papers with many symbols should have a nomenclature that defines all symbols with units, inserted above the references. If one is used, it must contain all the symbols used in the manuscript and the definitions should not be repeated in the text. In all cases, identify the symbols used if they are not widely recognized in the profession. Define acronyms in the text, not in the nomenclature.
- **References** must be cited consecutively in the text using square brackets [1] and collected together in a reference list at the end of the manuscript.
- **Appendix(-icies)** if any.

SPECIAL NOTES

Units: The SI system of units for nomenclature, symbols and abbreviations should be followed closely. Symbols for physical quantities in the text should be written in italics (e.g. *v*, *T*, *n*, etc.). Symbols for units that consist of letters should be in plain text (e.g. ms^{-1}, K, min, mm, etc.). Please also see: http://physics.nist.gov/cuu/pdf/sp811.pdf .

Abbreviations should be spelt out in full on first appearance followed by the abbreviation in parentheses, e.g. variable time geometry (VTG). The meaning of symbols and units belonging to symbols should be explained in each case or cited in a **nomenclature** section at the end of the manuscript before the References.

Figures (figures, graphs, illustrations digital images, photographs) must be cited in consecutive numerical order in the text and referred to in both the text and the captions as Fig. 1, Fig. 2, etc. Figures should be prepared without borders and on white grounding and should be sent separately in their original formats. If a figure is composed of several parts, please mark each part with a), b), c), etc. and provide an explanation for each part in Figure caption. The caption should be self-explanatory. Letters and numbers should be readable (Arial or Times New Roman, min 6 pt with equal sizes and fonts in all figures). Graphics (submitted as supplementary files) may be exported in resolution good enough for printing (min. 300 dpi) in any common format, e.g. TIFF, BMP or JPG, PDF and should be named Fig1.jpg, Fig2.tif, etc. However, graphs and line drawings should be prepared as vector images, e.g. CDR, AI. Multi-curve graphs should have individual curves marked with a symbol or otherwise provide distinguishing differences using, for example, different thicknesses or dashing.

Tables should carry separate titles and must be numbered in consecutive numerical order in the text and referred to in both the text and the captions as Table 1, Table 2, etc. In addition to the physical quantities, such as *t* (in italics), the units [s] (normal text) should be added in square brackets. Tables should not duplicate data found elsewhere in the manuscript. Tables should be prepared using a table editor and not inserted as a graphic.

REFERENCES:

A reference list must be included using the following information as a guide. Only cited text references are to be included. Each reference is to be referred to in the text by a number enclosed in a square bracket (i.e. [3] or [2] to [4] for more references; do not combine more than 3 references, explain each). No reference to the author is necessary.

References must be numbered and ordered according to where they are first mentioned in the paper, not alphabetically. All references must be complete and accurate. Please add DOI code when available. Examples follow.

Journal Papers:

Surname 1, Initials, Surname 2, Initials (year). Title. Journal, volume, number, pages, DOI code.

[1] Hackenschmidt, R., Alber-Laukant, B., Rieg, F. (2010). Simulating nonlinear materials under centrifugal forces by using intelligent cross-linked simulations. *Strojniški vestnik - Journal of Mechanical Engineering,* vol. 57, no. 7-8, p. 531-538, DOI:10.5545/sv-jme.2011.013.

Journal titles should not be abbreviated. Note that journal title is set in italics.

Books:

Surname 1, Initials, Surname 2, Initials (year). Title. Publisher, place of publication.

[2] Groover, M.P. (2007). *Fundamentals of Modern Manufacturing*. John Wiley & Sons, Hoboken.

Note that the title of the book is italicized.

Chapters in Books:

Surname 1, Initials, Surname 2, Initials (year). Chapter title. Editor(s) of book, book title. Publisher, place of publication, pages.

[3] Carbone, G., Ceccarelli, M. (2005). Legged robotic systems. Kordić, V., Lazinica, A., Merdan, M. (Eds.), Cutting Edge Robotics. Pro literatur Verlag, Mammendorf, p. 553-576.

Proceedings Papers:

Surname 1, Initials, Surname 2, Initials (year). Paper title. Proceedings title, pages.

[4] Štefanić, N., Martinčević-Mikić, S., Tošanović, N. (2009). Applied lean system in process industry. *MOTSP Conference Proceedings*, p. 422-427.

Standards:

Standard-Code (year). Title. Organisation. Place.

[5] ISO/DIS 16000-6.2:2002. *Indoor Air – Part 6: Determination of Volatile Organic Compounds in Indoor and Chamber Air by Active Sampling on TENAX TA Sorbent, Thermal Desorption and Gas Chromatography using MSD/FID.* International Organization for Standardization. Geneva.

WWW pages:

Surname, Initials or Company name. Title, from http://address, date of access.

[6] Rockwell Automation. Arena, from *http://www.arenasimulation.com,* accessed on 2009-09-07.

EXTENDED ABSTRACT:

When the paper is accepted for publishing, the authors will be requested to send an **extended abstract** (approx. one A4 page or 3500 to 4000 characters). The instruction for composing the extended abstract are published on-line: http://www.sv-jme.eu/information-for-authors/ .

COPYRIGHT:

Authors submitting a manuscript do so on the understanding that the work has not been published before, is not being considered for publication elsewhere and has been read and approved by all authors. The submission of the manuscript by the authors means that the authors automatically agree to transfer copyright to SV-JME when the manuscript is accepted for publication. All accepted manuscripts must be accompanied by a Copyright Transfer Agreement, which should be sent to the editor. The work should be original work by the authors and not be published elsewhere in any language without the written consent of the publisher. The proof will be sent to the author showing the final layout of the article. Proof correction must be minimal and executed quickly. Thus it is essential that manuscripts are accurate when submitted. Authors can track the status of their accepted articles on http://en.sv-jme.eu/.

PUBLICATION FEE:

Authors will be asked to pay a publication fee for each article prior to the article appearing in the journal. However, this fee only needs to be paid after the article has been accepted for publishing. The fee is 240.00 EUR (for articles with maximum of 6 pages), 300.00 EUR (for articles with maximum of 10 pages), plus 30.00 EUR for each additional page. The additional cost for a color page is 90.00 EUR. These fees do not include tax.

Strojniški vestnik -Journal of Mechanical Engineering
Aškerčeva 6, 1000 Ljubljana, Slovenia,
e-mail: info@sv-jme.eu

9 770039 248001
ISSN 0039-2480

http://www.sv-jme.eu

Contents

Papers